Ministère de l'enseignement supérieur et de la recherche scientifique

Université Hassiba Benbouali de Chlef

Faculté de Technology

Département de Génie mécanique

THÈSE

Présentée pour l'obtention du diplôme de

DOCTORAT

Filière : Génie Mécanique

Spécialité : Mécanique Energétique

Par

BEDROUNI MOHAMMED

Thème :

Simulation numérique de l'écoulement d'un fluide compressible autour d'un système d'obstacles décalés avec la méthode LES

Soutenue le 05/01/2020, devant le jury composé de :

Mr. Mohammed Hadj MELIANI	Professeur	UHB-Chlef	Président
Mr. Madjid MERIEM-BENZIANE	Professeur	UHB-Chlef	Examinateur
Mr. AbdALLAH BENAROUS	Professeur	USD-BLIDA	Examinateur
Mr. Boualem CHETTI	MCA	UDB-Khemis Miliana	Examinateur
Mr. Amar ZERROUT	MCA	UHB-Chlef	Examinateur
Mr. Ali KHELIL	Professeur	UHB-Chlef	Encadreur

Ministry of the Higher education and Scientific Research

University Hassiba Benbouali of Chlef

Faculty of Technology

Department Of Mechanical Engineering

A DESSERTATION

Presented for obtaining the diploma of

DOCTORAT

Field: Mechanical Engineering

By

MOHAMMED BEDROUNI

Thesis Title :

Numerical Simulation of Compressible Fluid Flow Past Staggered Obstacles Using Large Eddy Simulation Method

Defended on 05/01/2021, Before a jury composed of:

Mr. Mohammed Hadj MELIANI	Professor	UHB-Chlef	President
Mr. Madjid MERIEM-BENZIANE	Professor	UHB-Chlef	Examiner
Mr. AbdALLAH BENAROUS	Professor	USD-BLIDA	Examiner
Mr. Boualem CHETTI	MCA	UDB-Khemis Miliana	Examiner
Mr. Amar ZERROUT	MCA	UHB-Chlef	Examiner
Mr. Ali KHELIL	Professor	UHB-Chlef	Supervisor

Acknowledgements

Firstly, I would like to express my deepest sense of gratitude to my supervisor, Professor ***Ali KHELIL***, for his patient guidance, encouragement, understanding and excellent advice throughout this thesis as well as providing me all facilities during my thesis. I attribute the level of my thesis to his encouragement and effort and without him this thesis would not have been completed or written.

My sincere appreciation goes to the Professor ***Hassan NAJI*** & professor ***Mohammed BRAIKIA*** for their constant supports, great advices and comments, directing and assistance during the work of this thesis, which appointed them a backbone of this work.

I am also grateful to professors of the mechanical department for their support and encouragement.

Most important thanks here go to my family who have helped me to achieve all my goals.

Finally, I would like to offer special thanks to my friends who helped me to have enjoyable and memorial stay.

Chlef, October 7, 2020

Mohammed BEDROUNI

*I dedicate my dissertation work to the spirits of my **Father** and my **Brother***

To my mother, my wife, my son, my brothers and my sister

To all my friends and family.

Contents

List of Figures

List of tables

Abstract

The thesis deals with the study of the flow past a single bluff body in the first part and an array of staggered obstacles in the second part with the use of numerical approaches.

Firstly, we have conducted a dynamic and thermal study of the flow past a single obstacle to well understand the flow mechanisms and structures. The main objective is to explore and discuss the effects of rounding the top corners of electronic components which are subjected to a cross-flow and a perpendicular impinging jet on the cooling efficiency. Simulations were performed at a Reynolds number of 3410 for the channel flow and three different impinging-to-cross-flow Reynolds number ratios ($\alpha = 0.5,\ 1\ and\ 1.5$) based on the radius of the rounded top corner, four cubic geometries were examined. The impacts of the rounded corner on coherent structures and cooling improvement is the principal aim of the study. The Shear Stress Transport (SST) K-ω model is implemented. Moreover, the assessment of this simulation is investigated by comparison with available experimental data. It should be noted that the high mesh resolution was handled where the wall-normal coordinate value is relevant for walls (herein $0.01 \le y^+ \le 0.19$ for the cube wall). Excellent agreement was obtained between the numerical results and experimental data. The coherent structures and flow features created closer to the components significantly influence the wall heat transfer. Furthermore, for $\alpha = 1\ and\ 1.5$, the cooling effectiveness can be enhanced by more than 6% and 23% respectively with rounding top corners of the cube compared to the base case.

In the second part, A large-eddy simulation (LES) study has been undertaken to investigate the turbulent dynamic structure of a fluid flow past two different staggered tube bundles. The first bundle is composed of all circular cylinders and the second is composed of circular and square cylinders. Computations have been conducted for $Re_D = 12{,}858$, which match available experiments. To select the appropriate grid, our findings were compared with available experimental data and the GCI method is used to assess the grid refinement influence on the solution. It should be stressed that the mesh density was chosen so that the wall-normal coordinate y^+ value is suitable (herein $0.14 \le y^+ \le 0.87$ for the walls cylinders). It turned out that, for the fine mesh, the results get by the considered model corroborate available experimental data and were more accurate than those of Patel obtained with the RANS-SST model. Streamlines, turbulence kinetic energy contours, instantaneous vorticity contours computed indicate that wake patterns are more chaotic in the mixed configuration exhibiting larger recirculation zones compared to the purely circular tube bundle. In addition, flow coherent eddies within both configurations are identified via the Q-criterion. Based on the obtained

findings we can conclude that, in addition to being physically sound, the adopted model is found to be suitable for simulating the turbulent flow over circular and mixed staggered tube bundles with higher resolution.

Keywords: Flow past obstacles, Heat transfer enhancement, Cooling electronic components, Large eddy simulation, Shear Stress Transport model, GCI method.

ملخص

تتناول الأطروحة دراسة التدفق الذي يمر عبر عقبة واحدة في الجزء الأول ومجموعة من العقبات المتداخلة في الجزء الثاني باستخدام طرق عددية.

أولاً ، لقد أجرينا دراسة ديناميكية وحرارية للتدفق عبر عقبة واحدة لفهم آليات وهياكل التدفق جيدًا. الهدف الرئيسي هو استكشاف ومناقشة تأثيرات تدوير الزوايا العلوية للمكونات الإلكترونية التي تخضع لتدفق القناة و تدفق الاصطدام العمودي على كفاءة التبريد. تم إجراء عمليات المحاكاة برقم رينولدز 3410 لتدفق القناة وثلاث نسب مختلفة ($\alpha = \mathrm{Re}_j / \mathrm{Re}_H = 0.5,\ 1\ and\ 1.5$). بناءً على نصف قطر الزاوية العلوية المستديرة ، تم فحص أربعة أشكال هندسية مكعبة. تعتبر تأثيرات الزاوية المستديرة على الهياكل المتماسكة وتحسين التبريد الهدف الرئيسي للدراسة. تم تطبيق النموذج K-w SST في المحاكاة. علاوة على ذلك ، تم تقييم هذه المحاكاة من خلال المقارنة مع البيانات التجريبية المتاحة. وتجدر الإشارة إلى أنه تم التعامل مع الشبكة ذات الدقة العالية بحيث تكون مناسبة للجدران ($0.01 \le y^+ \le 0.19$ لجدار المكعب). تم الحصول على توافق ممتاز بين النتائج العددية والبيانات التجريبية. تؤثر الهياكل المتماسكة وميزات التدفق التي تم إنشاؤها بالقرب من المكونات بشكل كبير على نقل حرارة المكون الإلكتروني. علاوة على ذلك ، و في حالة 1.5 و $\alpha = 1$ يمكن تحسين فعالية التبريد بأكثر من 6٪ و 23٪ على التوالي من خلال تدوير الزوايا العلوية للمكون الالكتروني.

في الجزء الثاني ، تم إجراء دراسة لاستقصاء البنية الديناميكية المضطربة لتدفق السوائل عبر نموذجين مختلفين من العوائق المتداخلة باستخدام طريقة المحاكاة واسعة النطاق (LES). تتكون الحزمة الأولى من أسطوانات دائرية فقط والثانية تتكون من أسطوانات دائرية ومربعة. تم إجراء الحسابات من اجل رقم رينولدز $Re_D = 12{,}858$ التي تتوافق مع التجارب المتاحة. لتحديد الشبكة المناسبة ، تمت مقارنة النتائج التي توصلنا إليها مع البيانات التجريبية وقمنا باستخدام الطريقة GCI لتقييم تأثير تحسين الشبكة على الحل. يجب التأكيد على أنه تم اختيار كثافة الشبكة بحيث تكون مناسبة ($0.14 \le y^+ \le 0.87$ لأسطوانات الجدران). اتضح أنه بالنسبة للشبكة الدقيقة ، فإن النتائج التي تم الحصول عليها من خلال النموذج المدروس تدعم البيانات التجريبية المتاحة وكانت أكثر دقة من تلك الخاصة بباتيل (patel) التي تم الحصول عليها باستخدام نموذج RANS- SST. تشير خطوط الانسياب ، وملامح الطاقة الحركية المضطربة ، وخطوط الدوامة اللحظية المحسوبة إلى أن أنماط التدفق أكثر فوضوية في حزمة الانابيب المختلطة التي تنتج مناطق إعادة تدوير أكبر مقارنة بحزمة الأنابيب الدائرية البحتة. بالإضافة إلى ذلك ، تم تحديد الدوامات المتماسكة للتدفق داخل كلا النموذجين عبر المعيارQ . بناءً على النتائج التي تم الحصول عليها يمكننا أن نستنتج أن النموذج المعتمد مناسب لمحاكاة التدفق المضطرب عبر حزمة الأنابيب الدائرية والمختلطة و بدقة عالية.

الكلمات المفتاحية: التدفق عبر العقبات ، تحسين نقل الحرارة ، تبريد المكونات إلكترونية ، المحاكاة واسعة النطاق (LES)، التدفق المضطرب ، الطريقة GCI.

Résumé

La thèse traite l'étude de l'écoulement d'un fluide autours d'un seul obstacle dans la première partie et un système d'obstacles décalés dans la seconde partie avec l'utilisation des approches numériques.

Dans un premier temps, nous avons mené une étude dynamique et thermique de l'écoulement de l'air froid autours d'un seul obstacle pour bien comprendre les mécanismes et les structures d'écoulement. L'objectif principal est d'explorer et de discuter l'impact de l'arrondissement des coins supérieurs des composants électroniques soumis à un écoulement transversal et à un jet d'impact perpendiculaire sur l'efficacité du refroidissement. Les simulations ont été menées à un nombre de Reynolds de 3410 pour l'écoulement du canal et trois rapports différents de nombre de Reynolds entre le jet impactant et l'écoulement du canal ($\alpha = 0.5,\ 1\ and\ 1.5$). Sur la base du rayon du coin supérieur arrondi, quatre géométries cubiques ont été examinées. L'impact du coin arrondi sur les structures cohérentes et l'amélioration du refroidissement est l'objectif principal de l'étude. Le modèle SST K-ω est implémenté. De plus, la validation de la méthodologie et les résultats de cette simulation est étudiée par comparaison avec les données expérimentales disponibles. Il convient de noter que la résolution de maillage élevée a été gérée là où la valeur de coordonnée normale du mur est pertinente pour les murs ($0.01 \le y^+ \le 0.19$ pour la paroi du cube). Un excellent accord a été obtenu entre les résultats numériques et les données expérimentales. Les structures cohérentes et la morphologie de l'écoulement créées plus près des composants influencent considérablement le transfert de chaleur de la paroi. En outre, pour $\alpha = 1\ and\ 1.5$, l'efficacité de refroidissement peut être améliorée de plus de 6% et 23% respectivement en arrondissant les coins supérieurs du cube par rapport au cas de base.

Dans la deuxième partie, une étude a été entreprise pour étudier la structure dynamique turbulente d'un écoulement de fluide au-delà de deux systèmes d'obstacles décalés différents avec la méthode de la Simulation des grandes échelles (LES). Le premier faisceau est composé uniquement de cylindres circulaires et le second est composé de cylindres circulaires et carrés. Les calculs ont été effectués pour un nombre de Reynolds $Re_D = 12{,}858$, qui correspondent aux expériences disponibles. Pour sélectionner le maillage approprié, nos résultats ont été comparés aux données expérimentales disponibles et la méthode GCI est utilisée pour évaluer l'influence du raffinement du maillage sur la solution. Il convient de souligner que la densité de maillage a été choisie de manière à ce que la valeur de y+ soit appropriée ($0.14 \le y^+ \le 0.87$ pour les parois des cylindres). Il s'est avéré que, pour le maillage fin, les résultats obtenus par le modèle considéré corroborent les données expérimentales disponibles et étaient plus précis que ceux de Patel obtenus avec le modèle RANS-SST. Les lignes

de courant, les contours d'énergie cinétique de turbulence, les contours de tourbillon instantanés calculés indiquent que les modèles de sillage sont plus chaotiques dans la configuration mixte présentant des zones de recirculation plus grandes que le faisceau de tubes purement circulaire. De plus, les structures cohérentes dans les deux configurations sont identifiées via le critère Q. Sur la base des résultats obtenus, nous pouvons conclure que, en plus d'être physiquement solide, le modèle adopté s'avère approprié pour simuler l'écoulement turbulent sur des faisceaux de tubes décalés circulaires et mixtes avec une résolution plus élevée.

Mots clés : Ecoulement autours d’obstacles, amélioration du transfert de chaleur, refroidissement des composants électroniques, modèle de transport de contrainte de cisaillement (SST), Simulation des grandes échelles (LES), méthode GCI.

Nomenclature

b	Grid spacing (m)
Cw	WALE constant (--)
D	Cylinder diameter (m)
d	Nozzle jet diameter (m)
e	relative error (--)
GCI	grid convergence index (--)
H	Channel height (m)
h	Cube height (m)
k	Turbulent kinetic energy (m^2s^{-2})
Nu	Nusselt number
p	Pressure (Pa)
P_k, P_ω	Production terms of k and ω respectively
Pr_t	Turbulent Prandtl number
q	Heat flux (W)
R	Curved edge radius (m)
Re_D	Reynolds number $\mathrm{Re}_D = uD/\nu$
Re_H	Cross flow Reynolds number based in the cube height and the inlet velocity
Re_j	Impinging jet flow Reynolds number based in the nozzle diameter and the jet velocity
S	Strain rate tensor, (s^{-1})
$\|S\|$	Norm of strain rate tensor
S^d	Traceless symmetric tensor (s^{-1})
SL	Longitudinal pitch-to-diameter ratio
ST	transverse pitch-to-diameter ratio (--)
t	Time, (s)
T	Temperature (K)
U_H	Cross flow velocity inlet, (ms^{-1})
U_J	Jet velocity inlet, (ms^{-1})
U_{in}	Incoming flow velocity (ms^{-1})
u_τ	wall friction velocity (ms^{-1})
RSM	Reynolds Stress Model
SV	Side vortex
SST	Shear stress transport
x, y, z	Cartesian coordinate system (m)
y^+	Wall units coordinate (--)

Superscripts/subscripts

i, j, k	Coordinate alternation index
t	Turbulent
w	Wall
$(.)'$	Fluctuating quantity
$\bar{(.)}$	Filtered variable
$()^+$	Dimensionless quantity

Greek letters

δ_{ij}	Kronecker tensor (--)
ε	Dissipation of turbulent kinetic energy ($m^2\ s^{-3}$)
Ω	Antisymmetric vortex tensor
ω	Turbulent dissipation rate
μ	Dynamic viscosity **(**m^2s^{-1}**)**
μ_t	Turbulent viscosity **(**m^2s^{-1}**)**
ρ	Density, ($kg\ m^{-3}$)
κ	Von Karman constant
λ	Thermal conductivity ($W\ m^{-1}\ K^{-1}$)
ν	Kinematic viscosity (m^2s^{-1})
ν_t	SGS eddy-viscosity (m^2s^{-1})
τ_{sgs}	Deviatoric SGS stress tensor (Pa)
$\alpha = \frac{\mathrm{Re}_j}{\mathrm{Re}_H}$	Impinging to cross flow Reynolds number ratio
Δ	LES filter length (m)

Abbreviations

CFD	Computational fluid dynamic
LES	Large eddy simulation
LHV	Lower horseshoe vortex
RANS	Reynolds Averaged Navier Stokes
UHV	Upper horseshoe vortex
WV	Wake vortex

GENERAL INTRODUCTION

General Introduction

The study of the fluid flow past obstacles is one of the most widely studied problems due to its importance in many engineering applications such as cooling electronic components, flows over skyscrapers, flow across overhead cables, heat exchanger geometries and cooling system for nuclear industry (nuclear power plant, nuclear fuel rods, etc.). A variety of fluid dynamics phenomena is presented, such as separation, vortex shedding and the transition to turbulence. The flows taking place on these elements are often turbulent and are thereby difficult to handle numerically and experimentally. In other words, comprehensive understanding of phenomena involved in these flows by experimental means has often proved expensive, leading to the numerical methods use as a complementary tool to explain turbulence phenomena occurring over these systems.

Turbulence is a 3-D phenomenon that occurs frequently in fluid flows, having complex and irregular dissipative behavior. It is observed both in nature and in almost all industrial flows. Furthermore, turbulent flows cover up a broad range of temporal and spatial scales whose numerical resolution requires high grid resolution. Time-dependent simulations and high grid resolution can provide detailed predictions of the flow field with unfortunately a very long CPU run time. Currently, predicting unsteady turbulent flows with efficient numerical simulation methods remain limited. This is mainly due to their three dimensional, unsteady, and irregular traits. The direct numerical simulations (DNSs) is the most accurate method for studying such flows, which solve the Navier-Stokes equations without modelling on a fine grid using a small-time step. For simple flows, handling this method is suitable, however in case of complex flows, it becomes computationally expensive. Thereby, they are still limited to academic studies or simple engineering applications. The overall cost of a complete calculation is proportional to Reynolds number, which is not suitable for industrial applications where sufficient computer resources are lacking. Thus, Large Eddy Simulation (LES) or Unsteady Reynolds Averaged Navier-Stokes (URANS) approaches are preferred.

Cooling electronic component is a typical example of this kind of flows in which a fluid is used to cool down electronic components and prevent overheating. An efficient cooling system of electronic components is required to ensuring their use in a temperature range compatible with their performances and prevent the material damage. Improving the cooling effectiveness is still the main challenge in various types of electronic systems and many other compact heat dissipated devices. The forced air, nanofluids and liquid coolant can be used as working fluid to cool down and transferring the heat generated by electronic devices. The system of electronic components can be simulated as single body or an array of heated obstacles arranged in aligned or staggered arrangement.

Objectives of the thesis

The objectives of the thesis have been set as follows:

- In the case of the flow past a single obstacle, the primary target is to investigate the impact of the top corners rounding electronic component which subjected to a cross-flow and a perpendicular impinging jet on the cooling efficiency. Simulations were conducted at a cross-flow Reynolds number of 3410. Based on the radius of the top corner, four cubic geometries were investigated at three different impinging-to-cross-flow Reynolds number ratios ($\alpha = 0.5,\ 1\ and\ 1.5$). In total, twelve (12) cases were computed. The transitional Shear Stress Transport (SST) K-ω model is implemented, and the assessment of this simulation is achieved by comparison with the available experimental data.
- In the second case, a large eddy simulation study is performed to investigate the turbulent dynamic structure of a fluid flow in two staggered tube configurations, one is composed of all circular cylinders and the second is composed of circular and square cylinders. Computations has been performed for $Re_D = 12{,}858$, which match available experiments. The grid convergence index method is handled to select the appropriate grid so that the wall-normal coordinate value is relevant for walls. Large eddy simulation method, based on the wall-adapting local eddy viscosity model, was implemented and the results extracted from CFD simulations were compared with available experimental data. The results are also compared with those of Patel (2010) [95], achieved via a numerical simulation with the SST model. The main objective of this study is to simulate the mean flow from Balabani and Yianneskis (1996) [45] for the circular staggered tubes bundle to assess the methodology and subsequently the flow features. After model validation, time averaged and normalized results of streamwise velocity components, velocity vector fields, vorticity contours, and turbulent quantities have been obtained and compared for both arrangements.

Thesis structure

The thesis is started with a general introduction that consists on the methodology, the objectives of the study and the scope of work. The reader is then introduced to the main content of the following chapters.

In chapter 1, we sum up research on flow past a single obstacle in the first part and a system of obstacles in the second part with a particular regard for previous simulations.

Chapter 2, discusses the theoretical background of basic equations describing fluid motion. It explains how CFD formulates those equations. By using those equations, the Navier-Stokes

equations are derived. In the middle part of this chapter, we discuss the principles of the CFD. The last part describes the definition of turbulence and different models.

Chapter 3 presents a numerical study on the performance of rounded corners on the top of electronic components on cooling effectiveness. The chapter focuses mainly on the geometry effect of a single electronic component on heat transfer and coherent structures. We start by an introduction and a description of the studied case in which the geometry, boundary conditions, and mesh resolution are outlined in section 1. Then, Section 2 includes the mathematic formulation of the problem. In Section 3, the implemented mesh and its dependency from the solution is examined. The main findings are presented and commented in section 4. Finally, Section 5 recaps our conclusions.

Chapter 4 contains work done on the flow past in a staggered tube bundle. Using the large eddy simulation method, a numerical comparative study is handled to investigate the turbulent dynamic structure of a fluid flow in two staggered tube configurations, one is composed of all circular cylinders and the second is composed of circular and square cylinders. An introduction, geometry, problem setting and boundary conditions are done in the beginning part of this chapter. Then, turbulence modeling of the problem is highlighted in section 2. In section 3, the mesh resolution and the validation of our model of simulation against experimental data is presented. Then, in section 4 the main findings are presented and commented for the two configurations. At the end, Section 5 recaps our conclusions.

Chapter 5 summarizes the main findings and conclusions of the whole thesis. This focuses on the objectives of the work and how they are achieved throughout the thesis.

CHAPTER I: LITERATURE REVIEW

I.1 Introduction

The study of flow behavior around obstructions plays an important role in many engineering fields, whether from the dynamic side, the thermal aspect, or both. We can encounter such types of flow in cooling electronic components, heat exchangers, environmental problems linked to the dispersion of pollutants through the agglomerations as well as the effects of wind on buildings, or solar collectors, urban drains. The main objectives of analyzing such flows are increasing heat transfer between the fluid and obstacles and ensure material stability.

A typical example of flow past obstacles can be observed in the electronic field (Fig. I-1). During functioning of electronic components such as processors, a huge amount of heat is generated form these devices that should be removed away from equipment to prevent overheating and as consequence the damage of the material. Moreover, the operating temperature range of electronic devices must be maintained at a reliable operation temperature. Another example of flow past obstacles can be observed in nuclear power plants. A significant number of steam generators were removed from service or repaired each year. They failed and were found to be defective. Therefore, it is necessary to investigate the dynamic behavior in addition to the thermal aspect. The design of heat exchangers must take into account the reduction of the complex vortex shedding developed behind the cylindrical tubes that can cause severe vibration of the tubes and may cause serious structural failure

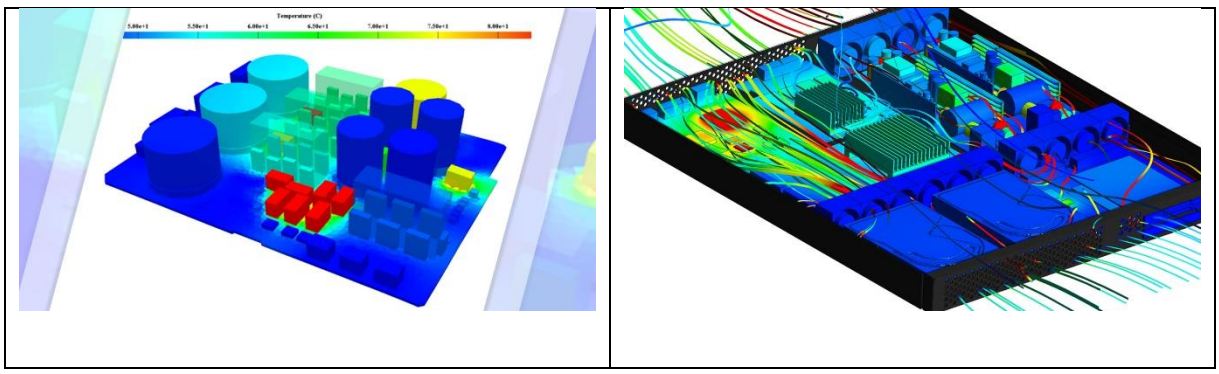

Figure I-1: Electronic components cooling

I.2 Flow past a wall mounted cube

Over the past few decades, there has been an enormous increase in the literature concerning the studying of the flow past bluff-body by experimental means, full scale measurements and recently numerical computation. This configuration has attracted increasing attention from researchers due to its application in many engineering fields. They studied the flow past a wall heated mounted cube from different perspectives in the aim of enhancing efficiency.

With the rapid growth of the Electronic Components Industry, the design size of electronic equipment is reduced; however, the generated heat amount is dramatically increased. Most failures in electrical and electronic components are commonly caused by overheating. An efficient cooling system is required to provide better cooling and prevent the material damage. In modern industry, research and optimization of electronic components cooling becomes increasingly important. The main objective of the cooling process is to ensure the use of electronic components within a safety zone. There are several methods to cool down electronic components. For example, the pin-fin heat sink, confined jet impingement, heat pipe and so on. The forced air flow is used to keep the heat generated by different parts of electronic devices within safety zone as can be achieved by nanofluids and liquid coolant. Numerical methods with experimental real-world verification are the main tools to evaluate efficiency of the cooling systems.

With the development of theoretical nanoscience, every year, a lot of new nanomaterials are produced in the laboratory [1]. These nano-fluids have been used with different volume fractions as the cooling fluid inside the system. Bahiraei et al. [2-5] and Goodarzi et al. [6] have examined the impact of using nanomaterials on cooling electronic components efficiency. They have found that nanoparticle concentration and nanofluid velocity have a major effect on the cooling improvement. Safaei et al. [7] studied numerically the effect of solid particles volume fraction and the inclination angle of microchannel on cooling effectiveness. They pointed out that the heat transfer is enhanced with the increasing of nanoparticle concentration or inclination angle. Dadsetani et al. [8] and Bahiraei et al. [9] explored and discussed the effect of the microchannel configuration on cooling enhancement. They showed that microchannel geometry has an important role in the cooling process system. Sahin et al. [10] investigated the impact of equilateral triangular bodies on flow characteristics and heat transfer at a Reynolds number ranged from 5000 to 10,000. They demonstrated that the cooling efficiency can be improved with the presence of the equilateral obstacles in the flow. Furthermore, they pointed out that the temperature profile behind the obstacles is affected by Reynolds number and the position of the triangles. A numerical study has been

performed by Octavio et al. [11] in order to examine the influence of aerodynamic shaping of the cooling fins in staggered heat sinks. The authors analyzed the aerodynamic efficiency for three different configurations (in-line rectangular, staggered rectangular and rounded staggered shape). They proved that the aerodynamic efficiency is significantly improved without affecting the thermal efficiency by the use of rounded cooling fins in heat sinks with staggered layout.

The task of sizing and designing a cooling process for electronic components is very difficult due to the complicated physical phenomena that take place. For this purpose, many researchers have developed algorithms which can be used as an alternative and a methodology for the design optimization of electronic components cooling systems [12-17]. The geometry of the heat sink was the subject of an optimization study carried out by Bhandari and Kulkarni [18] using particle swarm optimization. The objective function was the entropy generation minimization where the fin gap was chosen as the optimization parameter. They found that the optimized fin gap is 6.5 mm with an entropy generation of 21.4 W/K. Yildizeli and Cadirci [19] performed a simulation study of the fluid flow and conjugate heat transfer in a micro-channel heat sink and optimized with multi objective genetic algorithm known as elitist Non-Dominated Sorting Genetic Algorithm. They pointed out that the optimum results can be achieved with a higher channel width and a lower channel height.

The analysis of the fluid flow past a wall-mounted cube has been the subject of various studies, where a lot of papers have been presented in this regard. Several numerical studies have been carried out by Rundström and Moshfegh [20-24] in the aim to investigate the thermal performance of a cooling system on a heated wall-mounted cube with use of an impinging jet in a cross flow (Fig. I-2). In 2006, they [20-22] have examined the effect of combining the cross flow with an impinging jet on the thermal performance of a heated cube using the Reynolds-Stress-Model (RSM) as a turbulence model. The main finding of their study is that the cooling performance can be improved significantly with the use of an impinging jet in the cross-flow. They reported that the most cooling effect of the impinging jet is found at the top of the cube. However, increasing the cross-flow leads to more heat transfer at the side walls and at the rear face. In addition, the authors [22] conducted a comparative study on the heat transfer rate of an impinging jet in a cross flow on a heated cube using two turbulence models: the Reynolds Stress turbulence model (RSM) and the $\overline{v^2} - f$ model. They pointed out that, the RSM model is more accurate than $\overline{v^2} - f$ model for both the velocity and the heat transfer rate. In 2008, they investigated the effect of the channel height on the cooling performance in addition to the Reynolds numbers of the two streams [23]. Computational results were validated against experimental data obtained by an infrared imaging system for the surface

temperature and a particle image velocimetry for the velocity field. The authors revealed that the flow morphology over a cube is very complex and is related to several phenomena such as stagnation point separations, reverse flow and curvature effects. They found that the heat transfer efficiency is affected by these latter. There is considerable increase in the heat transfer efficiency when the channel height decreases and also when the velocity of the impinging jet increases. Furthermore, correlations for the average heat transfer coefficient on the cube and the pressure loss coefficients were established. Using the Large Eddy Simulation (LES) method, the previous authors carried out another numerical study of the flow around a wall mounted-cube subjected to an impinging jet in a cross flow [24]. The predicted mean velocity field, turbulence quantities and the heat transfer rate using the LES were validated against experimental data and compared with those of RSM model. They have reported that the LES results were in better agreement with the experimental data compared to the RSM model.

Hajime et al. [25] conducted an experimental investigation of the fluid flow and the local heat transfer around a wall mounted cube. The study was performed for five Reynolds numbers ranging from 4.2 10^3 to 3.3 10^4 based on the cube height and the inlet velocity. They have stated that there is a direct relationship between the heat transfer and the flow morphology. In front and on both sides of the cube, a horseshoe vortex is developed associated with high heat transfer. In addition, the Nusselt

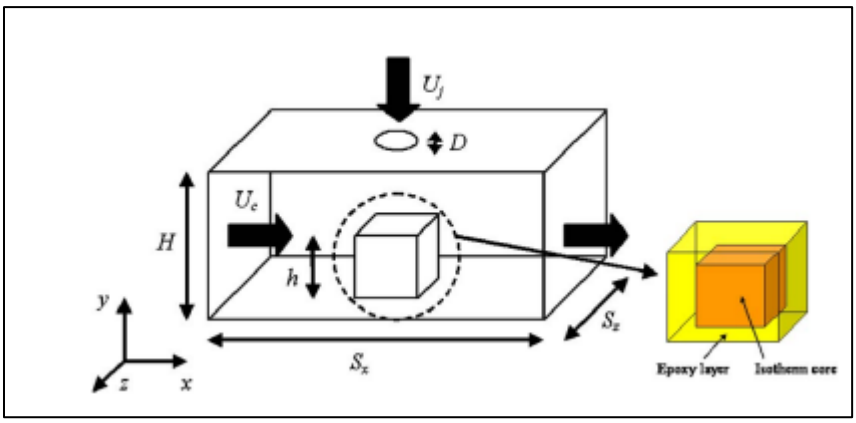

Figure I-2: Computational domain and a schematic sketch (Rundström and Moshfegh [20])

number reported in the front face is double than that on the base wall far from the cube. Moreover, expressions for the overall Nusselt number on the cube and the mean Nusselt number on each face as a function of the Reynolds number have been established. The fluid flow past an inline array of cubes was the subject of a numerical study carried out by Popovac and Hanjalic [26] using LES method. Five cubes were mounted on the bottom wall of the channel and subjected to a cross flow conjugated with a round impinging jet with a Reynolds number of 4800 and 5200, respectively. They demonstrated that there is a close relationship between the heat transfer and the flow structures

created around the central cube. Compared to experimental data, their results were moderately in good concordance. In addition, they reported that a horseshoe vortex wraps around the jet and creates a reverse flow is developed by the cross flow. Furthermore, the authors stated that the vortical structures contributed most to the heat removal from the cube. Focusing on the flow morphology and the thermal behavior, the previous authors handled another numerical study of the flow past a wall-mounted heated cube in an in-line array using LES method [27]. They found that, complex vortical structures were created due to the interaction between the two inflow streams, which improve the heat transfer efficiency. Furthermore, an arch vortex is established behind the cube, so the fluid can hardly reach the rear face and as a result poor heat removal from this face is shown. In addition, they concluded that there is a correlation between the turbulent stress and the turbulent heat flux. Tummers et al. [28] studied experimentally the flow features and temperature profile of a heated wall-mounted cube from an inline array subjected to a cross flow and an impinging jet (Fig. I-3). Two cases were studied: the first one is the jet nozzle is placed above the center of the cube, and the other one is when the jet nozzle is positioned just upstream of the front face of the cube. Their findings revealed that heat transfer efficiency is better for the second situation. Furthermore, they pointed out that the flow structures and the rolling up of separating shear layers influence considerably the heat transfer efficiency.

An experimental study of the turbulent flow past a wall-mounted cube placed in a channel center was performed by Massip et al. [29]. As depicted in Fig.I-4, the cube was exposed to a cross-flow and an impinging jet. The experiment was conducted for three cross-flow Reynolds numbers (Re_H=3410, 5752, 8880) and three values of the impinging to cross-flow Reynolds number ratio ($\mathrm{Re}_j / \mathrm{Re}_H = 0.5, 1 \; and \; 1.5$). In total, nine cases were studied. Using Planar Particle Image Velocimetry

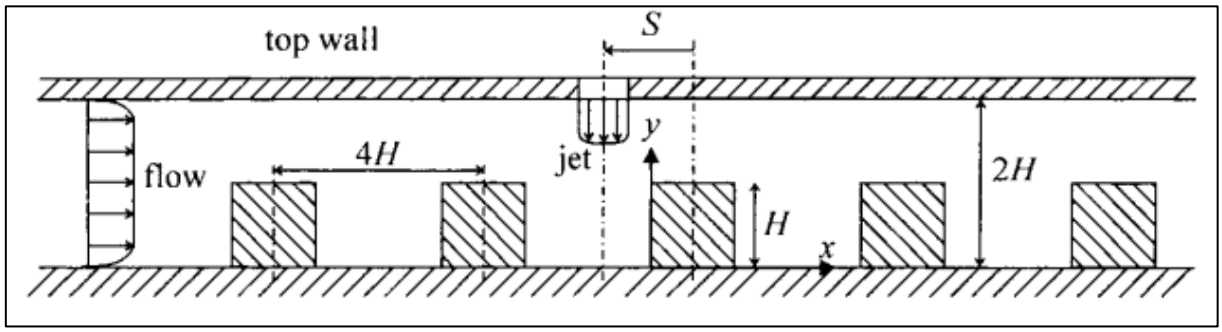

Figure I-3: Sketch of Flow configuration (Tummer et Al [28])

(PIV), the authors measured the instantaneous flow velocity on several planes, and as a result, they obtained the mean velocity and the Reynolds stresses. They noted that the Reynolds number ratio ($\mathrm{Re}_j / \mathrm{Re}_H$) has the greatest influence on the flow around the component than to the cross-flow

Reynolds number (Re_H). For the smallest ratio, they found that the jet was dragged and did not impact the component. The authors reported and discussed the morphology of the flow in term of vortices, recirculation bubbles, detachment and reattachment zones for the nine cases.

Nemdili et al. [30] investigated numerically the effect of a geometrical modification that consists of chamfering the top edges of the cube on the cooling efficiency using the Shear Stress Transport (SST) k-ω model. The study was performed at a Reynolds number of 3410 based on the bulk velocity and the channel height combined with three values of impinging jet Reynolds number

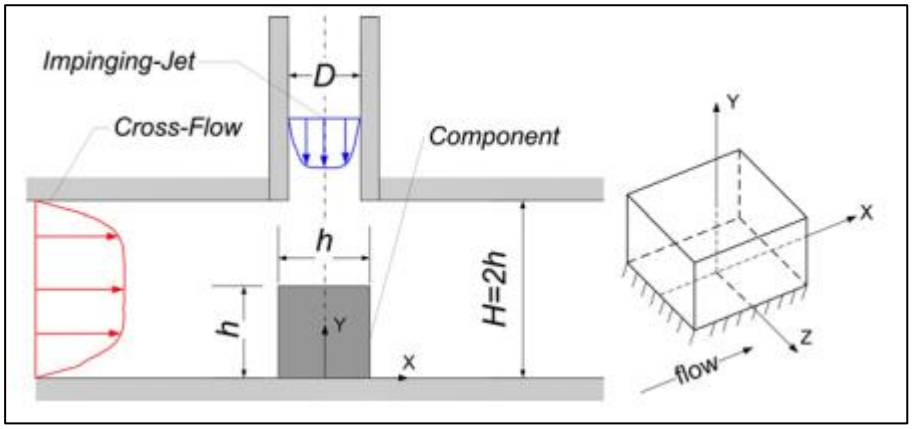

Figure I-4: Sketch of the side view of the test-section of the experiment of Massip et Al [29]

($Re_j / Re_H = 0.5, 1 \; and \; 1.5$). The obtained numerical results corroborate well available experimental data. They have found that there is no cooling improvement for the two first Reynolds number ratios ($Re_j / Re_H = 0.5 \; and \; 1$). However, they reported that for the largest ratio ($Re_j / Re_H = 1.5$), and with a chamfer top edge of 4 mm, the cooling effectiveness can be improved by 26% compared to the base case. Hearst et al. [31] experimentally examined the influence of the turbulence on the wake of a wall-mounted cube by creating turbulent boundary layers with different turbulence intensity and similar shear profiles. The experiment was conducted using particle image velocimetry and hot-wire anemometry at a Reynolds number of 1.8 *10^6 and cube height to boundary layer thickness of 0.47. They pointed out that the reattachment point in the wake region and the mean stagnation point are independent of the incoming profile. Moreover, they stated that with increasing the turbulence intensity and fixed normalized shear, the length of the wake is decreased. Meghdir et al. [32] numerically studied the effect of four different geometries of electronic components on cooling effectiveness using the Shear Stress Transport (SST) as turbulence model. The proposed geometries are illustrated in Fig. I-5. The component was exposed to two stream: cross-flow stream and an impinging jet. Their study consisted in varying the cross-flow Reynolds number (Re_H) and the ratio between the impinging jet and the cross-flow Reynolds number (α). They found that the geometry of

the element was of great importance in improving the cooling efficiency. Furthermore, they reported that the maximum exchanged heat flux can be achieved via the fourth element (C04).

From the literature survey, it is noticed that there is no great attention paid to the effect of the electronic component shape. For this raison, we will focus our study on the investigation of the influence of rounding the top corners of electronic components subjected to a cross-flow and a perpendicular impinging jet on the cooling effectiveness.

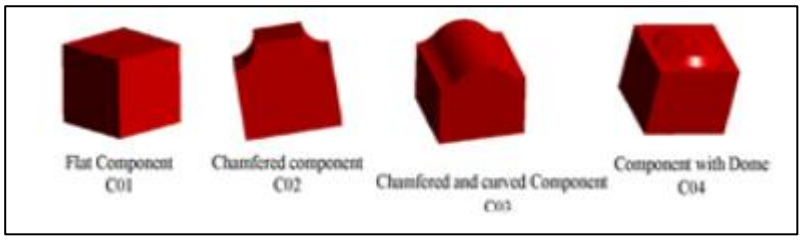

Figure I-5: The four proposed geometries (Meghdir et al. [32])

I.3 Flow past a tube bundle

The study of the fluid flow past a tube bundle is one of the most widely studied problems due to its application in many engineering applications such as flow across overhead cables, flows over skyscrapers, heat exchanger geometries, and in cooling systems for nuclear power plant [33-37]. Numerical simulation of flow through tubes bundle is a huge computational challenge due to the complexes flow features and unsteady flow phenomena presented. It is worthy to recall that early knowledge on rod bundle flows has come from experimental observations performed in the seventies. Circular cylinders, isolated or in bundles, are commonly seen in the offshore and ocean engineering structures. Subsea pipelines, marine risers and columns of semi-submersibles are salient examples. The flows taking place on these elements are often turbulent and are thereby difficult to handle numerically and experimentally. In other words, comprehensive understanding of phenomena involved in these flows by experimental means has often proved expensive, leading to the numerical methods use as a complementary tool to explain turbulence phenomena occurring over these systems (bundles) [38]. In practice, many configurations exist yielding the problem very complicated while leading to different flow patterns. The array may consist of purely circular tubes, as in heat exchangers, square tubes, as in buildings, or a mixture of tubes (circular and squares or wavy cylindrical), as in electronic component cooling systems and risers and supports offshore platform [39]. Apart from heat transfer considerations, we should take in account in the design the vortex-induced vibrations. The large-scale vortex shedding, the different wake interaction mechanisms and

the shear layers instability can cause a large amplitude vibrations or structural resonance in the bundle.

The turbulent cross-flow in tube bundles have been the subject of many researches to advance a physical understanding of such flows. Unfortunately, the URANS approach cannot predict well secondary flow regions, flow fields unsteadiness involving a separation and/or coherent turbulent structures [40]. Let's point out that, though RANS is unable to resolve turbulent fluctuations, it can provide insightful predictions for the mean flow at a much lower computing cost than the other approaches. Despite these defects, a study of coherent structures in a 7-rod bundle and in in a typical tight lattice has been performed via this approach with the Reynolds Stress Model (RSM) [41, 42]. On the other hand, LES has come to be as one of the most effective prediction methods for turbulent flows that can fill gaps URANS approach, as up noted and it provides more turbulent information with less computation efforts than the DNS [43]. Engineers take into account the available computing resources and the targeted physical precision level to choose the appropriate turbulence model. This is the LES which is adopted when, a proper unsteadiness prediction in wake regions flow separation prediction, etc. are sought. This approach becomes one of the most promising and successful methodology for simulating turbulent flows. The flow field is divided into large scale motions (large eddies) that are computed directly and modelled small scale (sub-grid scale (SGS)) via a filtering procedure. It is worthy to note that, large eddies contain most of the turbulent energy and are responsible for most of the momentum transfer and turbulent mixing. Current and future aspects of this approach have been reported by Piomelli [44].

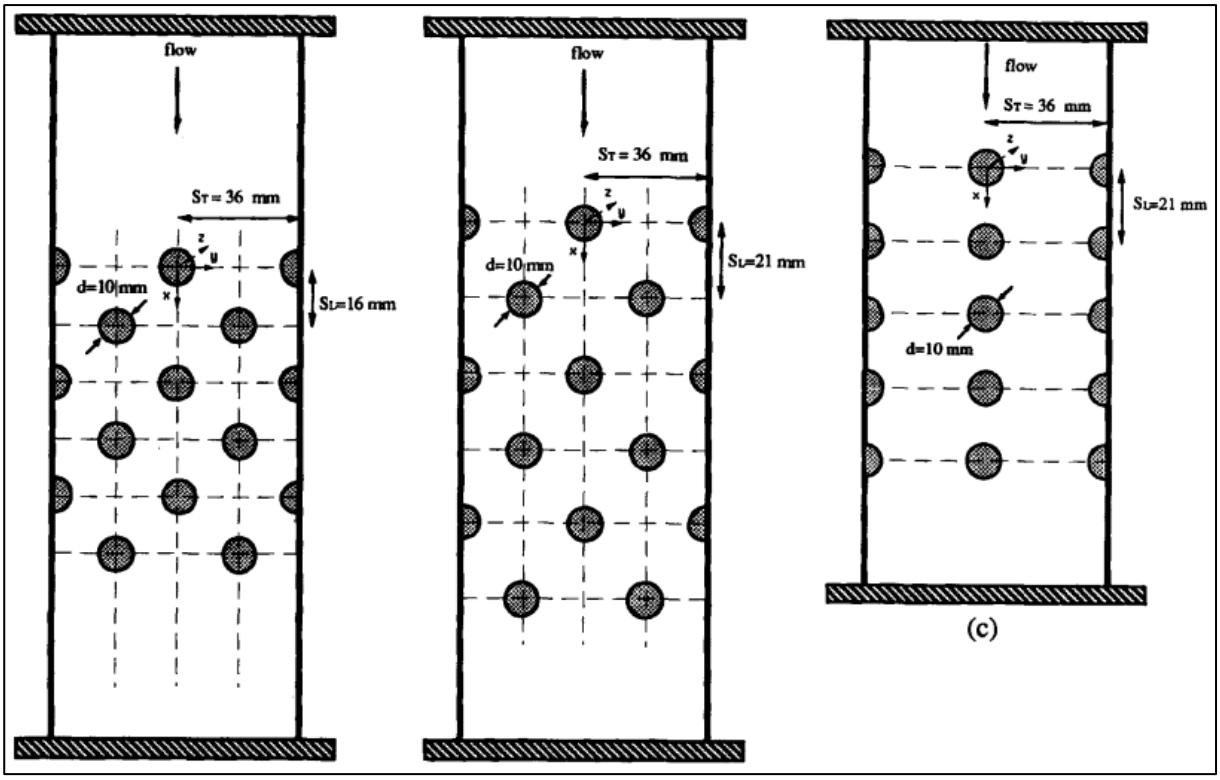

Figure I-6: Cross-section of the three tube bundles investigated (Balabani and Yianneskis [45])

Balabani and Yianneskis [45] have experimentally investigated the development of the turbulence level and flow features over three different circular tube array geometries based on the arrangement of cylinders in the bundle (Fig. I-6). For an in-line and two staggered arrays, they measured turbulence intensities and mean velocities from ensemble averaged and time resolved laser Doppler Anemometry (LDA) measurements. They revealed that the staggered geometries exhibit a higher pressure drop and generate higher levels of turbulence. Furthermore, in staggered geometries, strong interference from adjacent cylinders is observed. A numerical study of cross-fluid flow through a staggered tube bundle at subcritical Reynolds number with a large eddy simulation (LES) approach has been performed by Liang and Papadakis [46] at a Reynolds number of 8600. The studied configuration is shown in Fig. I-7. They report that their findings corroborate available correlations and experimental data.

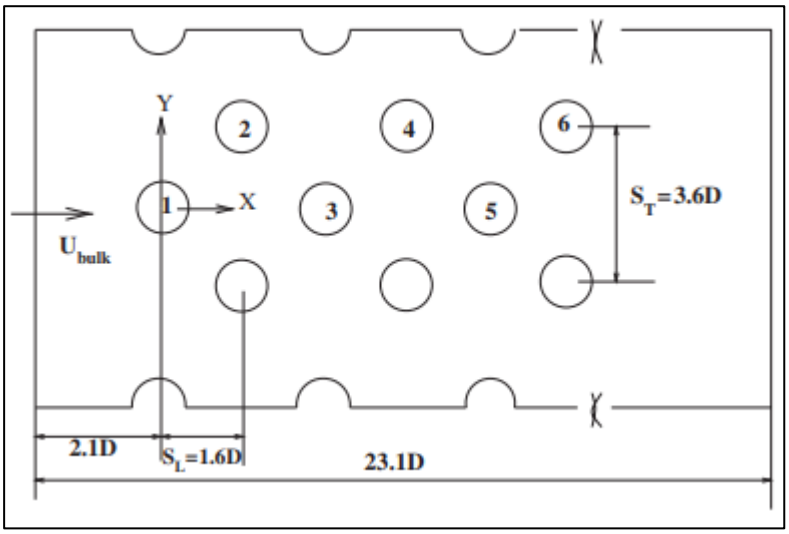

Figure I-7: Configuration of the six-row staggered tube array studied by Liang and Papadakis [46])

Da Silva et al. [47] conducted an experimental flow study past four confined in-line cylinder arrays using the laser Doppler anemometry technique with a Reynolds number of $\mathrm{Re}=1200$ based in the average inlet velocity. Array configurations considered in the experiments are depicted in Fig. I-8. They mainly investigated the effect of transversal and longitudinal spacing ratios on flow characteristics and on flow models identification. Their results for the different flow regimes examined were in good agreement with the literature. The authors reported that, for a given spacing ratio, there is no persistent flow regime along all cylinder rows. However, for a particular value of the spacing ratio, a quasi-steady behavior associated with a biased flow pattern has been identified. To confirm their measurements, da Silva et al. [48] performed an LES numerical investigation of a 3D flow on a five-row in-line bundle for the same subcritical Reynolds number. They reported that, in general, their results were in good agreement with experimental data relating to average velocities and fluctuations over time. Benhamadouche and Laurence [49] have examined the consistency of LES and transient Reynolds stress transport model (RSTM) in 2D and 3D, at a Reynolds number of 9×10^3. Two grid-refined levels have been used, a coarse and fine mesh. With the fine mesh, the authors have concluded that the LES results are more consistent with the DNS data and experiments. Moreover, they pointed out that with the coarse mesh, a reasonable agreement can be achieved. Satisfactory results in 3D were obtained with the RSTM model for the fine mesh, but when the grid was coarsened, no advantage of RSTM over the LES is showed. Also, they found that the 2D RSTM, generated strong vortex shedding, which is physically unreasonable.

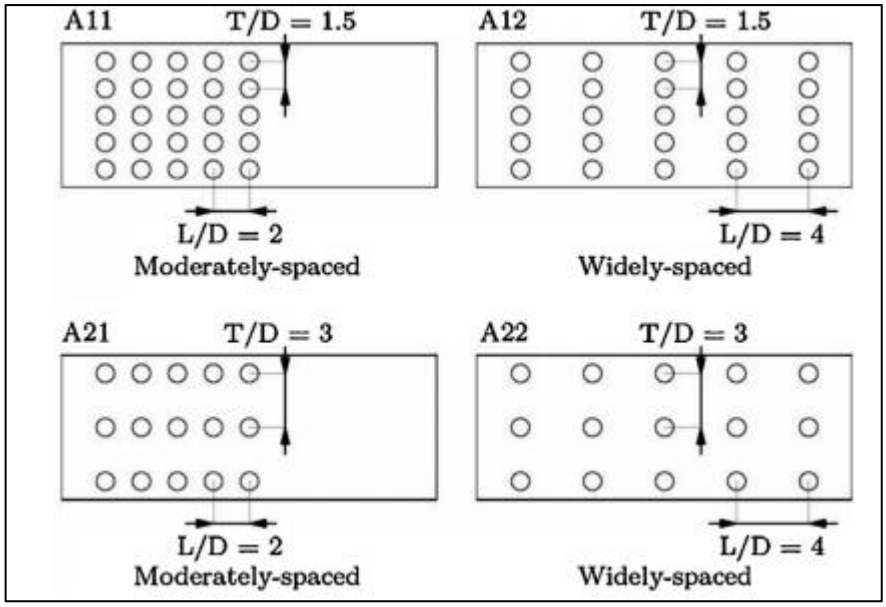

Figure I-8: Array configurations considered in the experiments of Da Silva et al. [47]

To our knowledge, few studies on flows past mixed tubes bundles have been performed. Fluid flow past cubes arrays have been studied by Zhengtong and Castro [50] (Fig. I-9). They carried out their computations with two Reynolds numbers, viz. 5×10^3 and 5×10^6 based on obstacle height and the stream velocity with the LES and RANS methods. They noted that, with overly coarse grids, LES is an effective tool for simulating airflow past urban obstacles at high Reynolds number. In addition, a comparative study has been done between LES and RANS, in which they have found that RANS is inadequate, especially in canopy region.

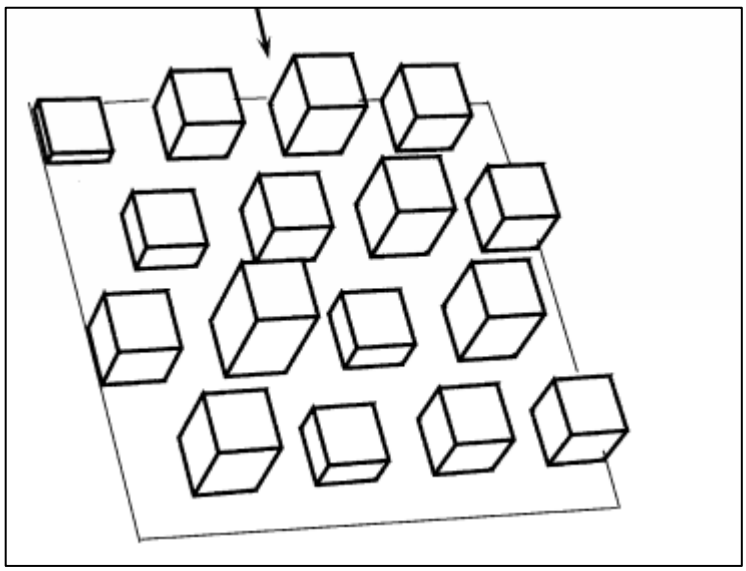

Figure I-9: Perspective view of the configuration studied by Zhengtong and Castro [50]

Oengören and Ziada [51] compiled experimental data on vortex shedding in a triangle arrangement. The study was carried out at a Reynolds number that ranges between 2700 and 52000. They found two Strouhal numbers in staggered rows cylinders. Kahil et al. [52] performed a numerical simulation of the flow past four cylinders using the LES based on the dynamic Smagorinsky model at a sub-critical Reynolds number of 3×10^3 and different pitch-to-diameter ratios (S_L/D). Cylinders were placed in square arrangement and the computation was carried out for five pitch to diameter ration ($S_L/D = 1.25,\ 1.4,\ 1.5,\ 1.75$ and 2.0). They pointed out that the flow pattern changed with the variation in spacing. Based on the analysis of the lift signals and the flow streamlines, a biased flow behavior was identified for spacing ratios 1.25, 1.4 and 1.5. Furthermore, they compared the velocity and pressure fields obtained from the simulation with experimental data and a good agreement between them was achieved. Chatterjee and Biswas [53] have investigated the dynamic behavior of flow around tube array composed of square cylinders at low Reynolds number (Re=100) (Fig. I-10). The cylinders were arranged in a staggered format with different transverse separation ratios (S/D=1, 2, 3 and 5; with S and d, are the transverse spacing and cylinder size). They have reported that for the larger separation ration, there is less flow interference effect, resulting in periodic and organized flow. However, as the separation ratio decreases, the flow interference becomes more prominent and as a result, the flow changes its state from an organized periodic to pseudo-periodic, and finally becomes completely chaotic. An antiphase shedding has been found to characterize the flow field for larger separation ratios (S/D=3 and S/D=5). In addition, they confirmed that the vortex shedding mechanism for larger spacing is completely controlled by the primary frequency, while secondary cylinder interaction frequency initiates at smaller spacing between cylinders.

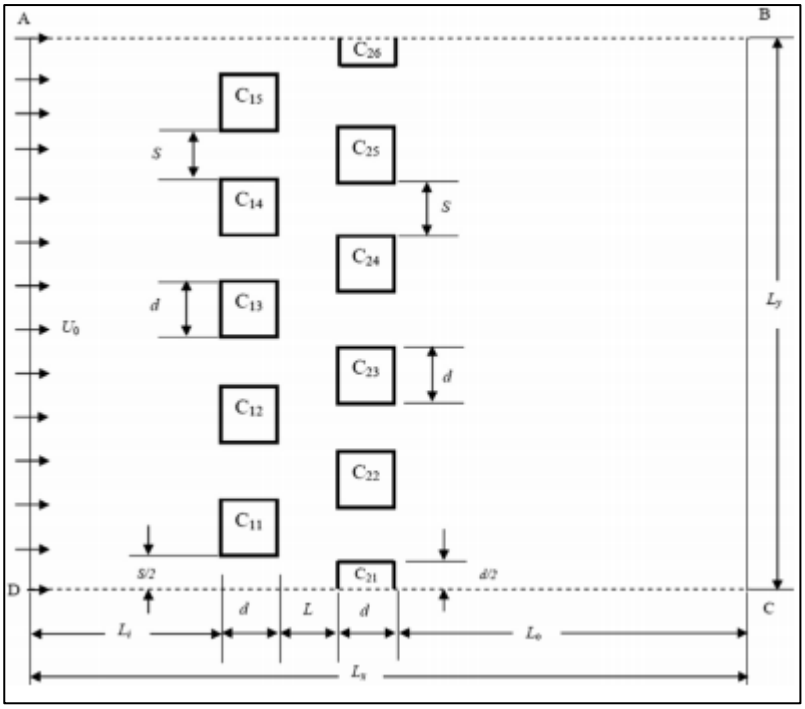

Figure I-10: Sketch of the computational domain (Chatterjee and Biswas [53]).

In 2010, the previous authors and Amiroudine [54], have studied numerically the flow around five square cylinders. The computations were conducted at a Reynolds number of 150 and four separation ratios (S/D= 1.2, 2, 3 and 4). The squares were arranged in side-by-side and normal to the on-coming flow. The purpose of their study is to explore and analyze the impact of the spacing between cylinders on vortex shedding mechanism and the wake structure. They reported that the primary (Strouhal) frequency is the dominant frequency associated to the vortex shedding and the secondary frequency effect is negligible. Furthermore, they noted that, there is similarity in the vortex shedding from two successive cylinders, however the vortices were in an arrangement of phase opposition when the distance of separation is more than twice the dimension of the cylinders (S/D > 2.0). Moreover, a clusters formation has been formed when the spacing is less than two diameters (S/D = 1.2) due to the deviation of the jets between cylinders and merging of wake structures. Lakehal [55] reported a detailed simulation analysis of turbulent convective flow upward along the heated rods of a PWR sub-channel using a highly-resolved LES approach. He noted that a large portion of the wall-to-flow heat transfer are caused by the secondary-flow motion induced by the mean flow. In addition, Labois and Lakehal [56] have developed and performed a Very-Large Eddy Simulation (VLES) modeling for a flow past a tube bundle and compared to traditional RANS and LES. The authors stated that such an approach well handles three-dimensional flow unsteadiness and it is clearly superior to any RANS approach. Lam et al. [57] conducted experimental study and an LES on turbulent flow around

wavy and circular cylinders tube bundles at subcritical Reynolds numbers ranging from 6,800 to 13,400. The experimental setup is illustrated in Fig. I-11. In such a range of Reynolds numbers, the authors set up that the drag is reduced significantly and that the fluctuating lift of the wavy cylinder is removed.

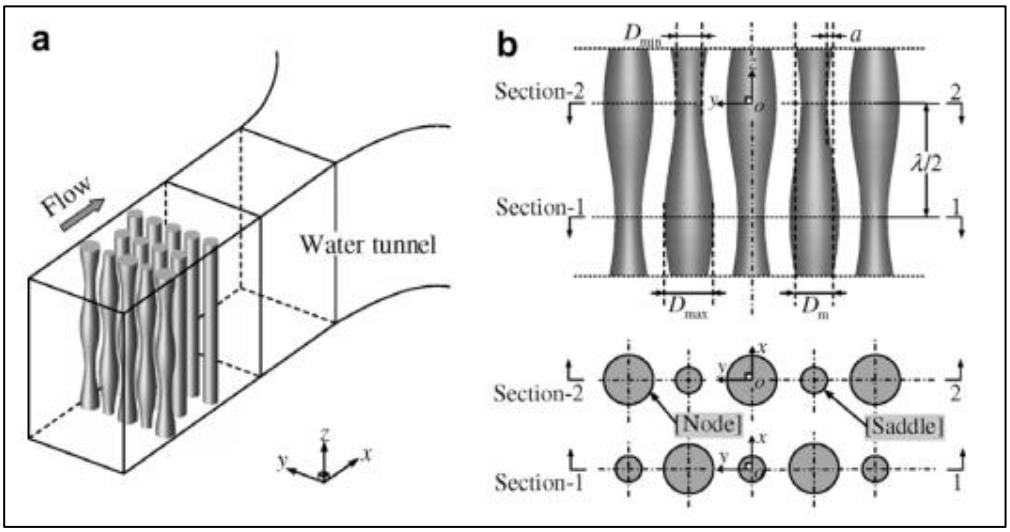

Figure I-11: Experimental setup of the tube bundle (Lam et al. [57]).

Mikuz and Tiselj [58] performed a LES of the turbulent flow in a 5×5 bar bundle. Their results corroborated the LDV benchmark data pointing that the WALE model is well suit to handle such a geometry. Samuel et al. [59] have used the large eddy simulation method to study the turbulent flow in an annular sector channel in which staggered semi-circular ribs was attached to both the inner and outer annular walls. Based on the mean inlet velocity, the computation was conducted at a reynolds number of 13900. Simulation results from LES were compared with experimental data and Reynolds-Averaged Navier-Stokes (RANS) simulation. They found that the unsteady flow features resolved from LES is better than RANS simulation. Moreover, they found that LES produces a good agreement with experimental data. The static pressure drop was also subject of comparison, in which they reported that higher accuracy is obtained from LES than RANS.

Our study focuses on the investigation of turbulent flow across circular and mixed tube bundles using the CFD Ansys™ Fluent 18.1 code in which the LES is implemented based on the WALE model with improved numerical and spatial resolution. The GCI method is used to check the independency of the solution from the mesh resolution. The assessment of this simulation is achieved by comparison with the experimental data of Balabani and Yianneskis [45].

CHAPTER II: COMPUTATIONAL FLUID DYNAMICS AND TURBULENCE MODELING

COMPUTATIONAL FLUID DYNAMICS AND TURBULENCE MODELING

Fluid dynamics is the science of fluid motion and with the development of computing technologies in the last decades, the Computational fluid dynamics, usually abbreviated CFD, becomes a powerful and potential tool to resolve engineering problems related to the fluid flow. Many problems in fluid mechanics requires the use of numerical approaches to solve them, in which experiments can't be handled due to many constraints as economic cost, physical limitations, environmental limits, safety and time constraints [60]. Furthermore, CFD provides engineers more data than experiments including data that is not currently measurable with available instrumentation equipment's.

II.1 Governing equations of fluid flow

In mid-18th century, the French engineer Claude Navier and the Irish mathematician George Stokes derived the well-known equations of fluid motion, known as the Navier-Stokes equations. These equations have been derived based on the fundamental governing equations of fluid dynamics, called the continuity, the momentum and the energy equations, which represent the conservation laws of physics.

Based on the concept of quantity conservation that stated conservation of a given quantity basically means that it is neither destroyed nor created, but is instead transformed from one form onto another. The conservation principle is applied to mass, momentum and energy.

II.1.1 Conservation of Mass

The derivation of the mass conservation equation is to write down a mass balance for mass element:

Rate of increase of mass in fluid element = Net rate of mass inflow - Net rate of mass outflow

Based on the above principle, the continuity equation can be written as [60]:

$$\frac{d\rho}{dt} + \vec{\nabla} \cdot \left(\rho \vec{V}\right) = 0 \qquad \text{(II-1)}$$

Where ρ is the fluid density, and $\vec{V}$ is the velocity vector that can be expressed in Cartesian coordinates as a function of the x, y, and z coordinates as well as time, as:

$$\vec{V} = \vec{V}(x,y,z,t) = u\,\vec{i} + v\,\vec{j} + w\,\vec{k} \qquad \text{(II-2)}$$

Where

u is the velocity distribution in the x-direction, $u(x,y,z,t)$.

v is velocity distribution in the y-direction, $v(x,y,z,t)$.

w is velocity distribution in the z-direction, $w(x,y,z,t)$.

II.1.2 Momentum equation

The key idea behind momentum conservation is that it is neither destroyed nor created but that rather it is transformed from one type of momentum onto another. This is really just Newton's second law of motion being applied to a fluid [60]:

$$\vec{F} = m\,\vec{a} \qquad \text{(II-3)}$$

Where F : force, m : mass, a : acceleration

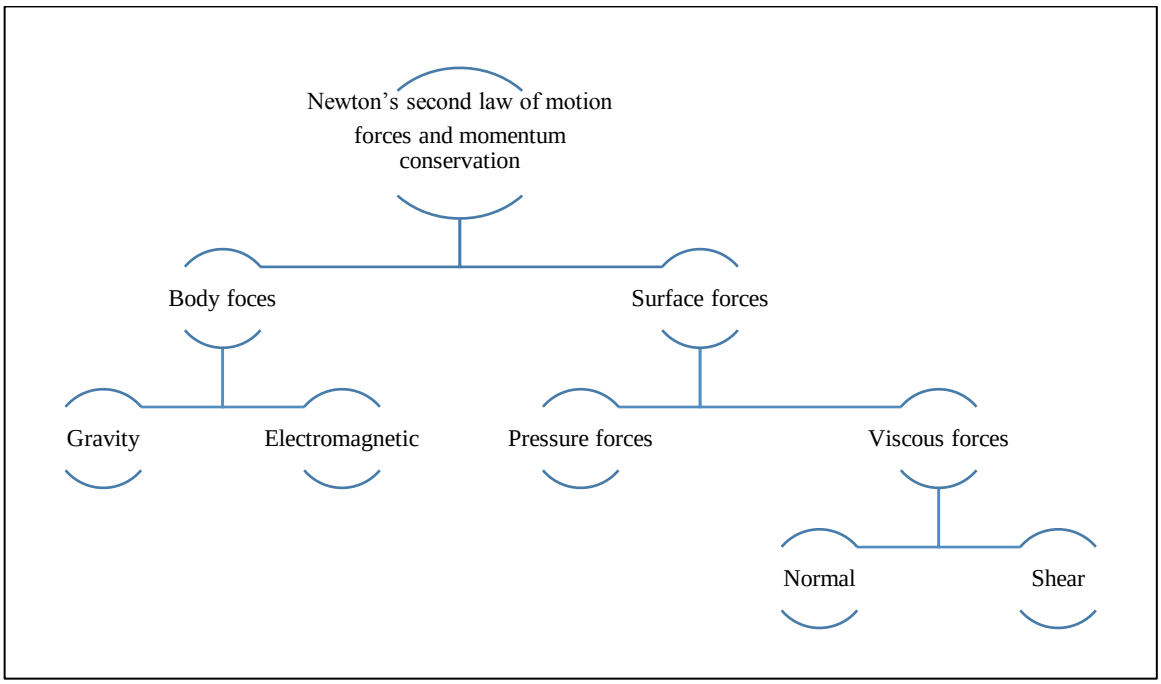

Figure II-1: forces on fluid particle.

Forces acting on fluid particle categorize on two types: body forces and surface forces, as shown conceptually in Fig. II-1. Forces that act directly upon the entire mass enclosed by the volume are known as body forces, such as gravity and electromagnetic forces. However, Surface forces are the

forces that act on the surface of the volume. Surface forces include two categories: pressure as a result of the action from the surrounding fluid and the viscous shear/normal stresses caused by frictional forces.

Considering body and surface forces, the momentum equation can be written as [60]:

$$\rho \frac{\partial \vec{V}}{\partial t} + \rho \vec{V}.\vec{\nabla}\vec{V} = -\vec{\nabla}\vec{\tau} - \vec{\nabla} P + \rho \vec{g} \qquad \text{(II-4)}$$

P: Pressure, τ : Shear stress and g : Gravity

At this point, fluid behavior can be modeled once a Newtonian or non-Newtonian shear function is specified. For Newtonian fluids, the stress is linearly proportional to the velocity gradients:

$$\tau_{ij} = Fluid\ Shear = \begin{vmatrix} \tau_{xx} & \tau_{xy} & \tau_{xz} \\ \tau_{yx} & \tau_{yy} & \tau_{yz} \\ \tau_{zx} & \tau_{zy} & \tau_{zz} \end{vmatrix} = 2\mu S_{ij} - \frac{2}{3}\left(\vec{\nabla}.\vec{V}\right)\delta_{ij} \qquad \text{(II-5)}$$

Where S_{ij} is the laminar shear.

$$S_{ij} = \frac{1}{2}\left(\frac{\partial u_i}{\partial x_j} + \frac{\partial u_j}{\partial x_i}\right) \qquad \text{(II-6)}$$

With a few exceptions, a fluid is said to be compressible if its speed reaches or exceeds 30% of its sound speed. The Mach number is expressed as the ratio of the fluid speed and its sound (Ma) [60].

$$Mach\ Number = Ma = \frac{u\ fluid}{u_{sound}} \qquad \text{(II-7)}$$

If this ration is less than 0.3, the fluid is then can be considered as incompressible [60].

II.1.3 Conservation of Energy

As with conservation of mass and momentum, the principle of energy conservation's states that the change of energy rate in a given body is the sum of the net heat fluxes plus the rate of work done on the body as a result of body and surface forces.

$$\dot{E} = \sum_i \dot{Q}_i - \sum_i \dot{W}_i \qquad \text{(II-8)}$$

The energy equation can be written in generalized form as [60]:

$$\underbrace{\frac{\partial(\rho E)}{\partial t}}_{\substack{\text{rate change}\\ \text{of total energy}\\ \text{in thefluid}}} + \underbrace{\vec{\nabla}.\left(\rho E\vec{V}\right)}_{\substack{\text{total energy}\\ \text{change due}\\ \text{tofluid convection}}} = \underbrace{\rho\dot{Q}}_{\substack{\text{volumetric}\\ \text{heat source}}} + \underbrace{\vec{\nabla}.(k\nabla T)}_{\substack{\text{rate of energy}\\ \text{change due}\\ \text{to conduction}}} - \underbrace{\left[\frac{\partial(uP)}{\partial x}+\frac{\partial(vP)}{\partial y}+\frac{\partial(wP)}{\partial z}\right]}_{\substack{\text{work done}\\ \text{on the fluid by}\\ \text{the pressure forces}}}$$

$$+\underbrace{\left[\begin{array}{l}\left(\frac{\partial(u\tau_{xx})}{\partial x}+\frac{\partial(v\tau_{xy})}{\partial x}\frac{\partial(w\tau_{xz})}{\partial x}\right)\\ +\left(\frac{\partial(u\tau_{yx})}{\partial y}+\frac{\partial(v\tau_{yy})}{\partial y}\frac{\partial(w\tau_{yz})}{\partial y}\right)\\ +\left(\frac{\partial(u\tau_{zx})}{\partial z}+\frac{\partial(v\tau_{zy})}{\partial z}\frac{\partial(w\tau_{zz})}{\partial z}\right)\end{array}\right]}_{\substack{\text{rate of work done on}\\ \text{the fluid by the viscous forces}}} + \underbrace{\rho\vec{F}.\vec{V}}_{\substack{\text{rate of work done on}\\ \text{the fluid by the body forces}}}$$

(II-9)

II.2 Introduction to Turbulence Theory

Turbulence is a three-dimensional unsteady viscous flow phenomenon that occurs frequently in fluid flows, both in nature and in almost all industrial flows (White 1991). For high Reynolds number flows and when momentum effects dominate viscous effects the flow becomes turbulent. In turbulent flows, high fluctuations are observed for fluid velocity, pressure and temperature both in time and in space [61,62]. These fluctuations refer to random, fast changes in a given variable, having dynamic spatial regions that are generated as molecular motion swirls collectively, forming coherent structures. Coherent structures are grouped fluid particles that move in unison as they rotate, stretch, translate, and decay. These are the “distinct curls” envisioned by Reynolds-turbulent eddies. As the flow becomes turbulent, it forms 3D coherent structures that are unstable both in time and space. This is what is best described classically by Hinze as turbulent flow with irregular (nondeterministic) fluid motion (Hinze 1987) [60]. Turbulent flow is irregular, random and chaotic. There exist a wide range of spatial and temporal scales for eddies. Their spatial range is as small as the Kolmogorov scale and about as large as the characteristic flow length scale. The time scales are associated with a range of eddy sizes, with the largest eddies having the largest time scales and the smallest eddies having the smallest time scales. The time and space scales can be modeled mathematically via Fourier analysis,

with the time scale being associated with a frequency, while the space scale is associated with a wavelength.

Turbulent flows require an energy source to feed its turbulent behavior, as eddies decay rapidly with time; that is, the coherent structures diminish in size and fluctuating magnitude, until they transform onto a laminar region in space having no fluctuations and no randomness.

II.2.1 Turbulence Modeling

There are three principal approaches to the prediction of turbulent flows based on what aspects of the turbulence structure are resolved. In the direct numerical simulation (DNS) approach, the unsteady Navier-Stokes equations are solved using highly accurate numerical schemes on a very fine spatial grid so that all characteristic time and length scales are resolved. Though fundamentally correct, the computing effort required for this approach, and the restrictions on the geometry of the flow domain and the boundary conditions that go with the methods used, restrict its applicability mainly to academic research. In the large eddy simulation (LES) approach, the large-scale structures of turbulence are fully resolved and computed while the Kolmogorov-scale structures are modeled using sub-grid closure relations. Since only large eddies are resolved, LES works with relatively coarse grids compared to DNS but shares its disadvantage of requiring three-dimensional, unsteady computations even when these are not warranted from an application point of view. The Reynolds-averaged Navier Stokes equations (RANS) approach (or its equivalent of Favre-averaged Navier-Stokes equations approach for compressible flows) is the most widely used of the three approaches used when dealing with industrial flow problems.

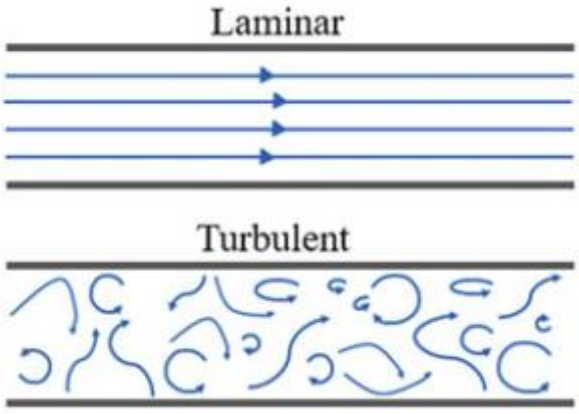

Figure II-2: Conceptual view of laminar and turbulent flow

To predict turbulent flows, two different approaches exist, statistical approach and non-statistical approaches. In a statistical approach ensemble averaging is carried out to separate mean quantities from fluctuating parts. While averaging the basic equations of motion, correlations

involving fluctuating velocities appear. These are additional unknowns for which no equation can be derived without again introducing additional unknowns. This is known as the closure problem of turbulence. To solve this problem, closure models are used so that we get additional relations between the correlations and mean quantities. These closure models generally work well for simple flows but become less and less accurate with an increase in the complexity of flow geometry. Despite this fact they are still widely popular in industry due to their lesser computational resource requirement. Turbulence models commonly available in CFD are summarized in Fig. II-3.

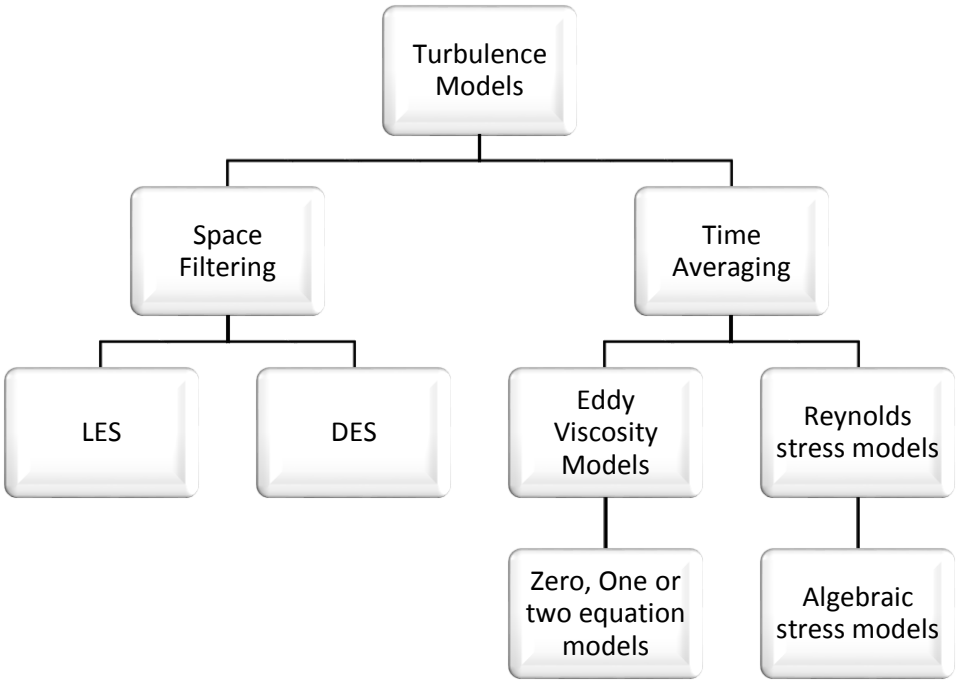

Figure II-3: Turbulence models classification

II.2.1.1 Statistical approaches

The first attempt to tract a seemingly intractable problem consisted of considering eddy behavior over a sufficiently long period of time. This allows their behavior to be time-averaged, thereby greatly simplifying its mathematical behavior (Reynolds1895). Based on the desired Reynolds-averaged Navier-Stokes (RANS) modeling complexity; there are zero-, one-, and two-equation models, as well as the so-called second-order closure models. The latter are also referred as second-moment closure models, stress transport models, Reynolds stress models (RSM), and Reynolds stress transport (RST) models. This is particularly so for the Reynolds stress tensor R, to point out what is still needed to have a full set of n independent turbulence equations, thereby solving n unknowns. Then, it is shown that applying the Boussinesq approximation is not sufficient for closure, so the path forward is to perform a set of mathematical operations that lead to additional

independent equations, with the aim of finally providing closure to the turbulence problem. In particular, the R tensor is derived mathematically in its exact form from the unoperated Navier-Stokes momentum equation by taking its first moment based on the fluctuating velocity, and then a time-average is performed. The resultant R tensor is used in RSM models and is therefore part of the motivation. But most importantly, the k PDE is derived from R by taking its trace, and it is this k PDE that is used in most zero-, one-, and two-equation RANS models (e.g., Prandtl, k-ε, k-ω,SST, etc.).

The Reynolds decomposition consists in the splitting of instantaneous flow into an average quantity and its associated fluctuating quantity [60].

$$u = \bar{u} + u' \tag{II-10}$$

Where $u, \bar{u}$ *and* u' are the instantaneous, mean and fluctuating components respectively. The other scalar quantities are also decomposed on the same principle.

Considering an incompressible fluid, the mass conservation can be written as [60]:

$$\frac{\partial u}{\partial x} + \frac{\partial v}{\partial y} + \frac{\partial w}{\partial z} = 0 \tag{II-11}$$

Using Reynolds' decomposition, let

$$\begin{cases} u = \bar{u} + u' \\ v = \bar{v} + v' \\ w = \bar{w} + w' \end{cases}$$

After substituting the decomposed velocities into the conservation of mass, we obtain:

$$\frac{\partial \bar{u}}{\partial x} + \frac{\partial v'}{\partial x} + \frac{\partial \bar{v}}{\partial y} + \frac{\partial v'}{\partial y} + \frac{\partial \bar{w}}{\partial z} + \frac{\partial w'}{\partial z} = 0 \tag{II-12}$$

Performing time-averaging on the conservation of mass and knowing that:

$$\bar{u'} = 0 \; and \; \bar{\bar{u}} = \bar{u}$$

Therefore, the mass conservation for turbulent flow becomes:

$$\frac{\partial \bar{u}}{\partial x} + \frac{\partial \bar{v}}{\partial y} + \frac{\partial \bar{w}}{\partial z} = 0 \tag{II-13}$$

From the above equation, we can conclude that the mass conservation is solely a function of the time-averaged velocities. Then, a similar approach can be applied to the momentum equations.

Considering a Newtonian, incompressible and unheated fluid, the momentum equations for a turbulent flow in the x direction can be written as [60]:

$$\rho\frac{\partial u}{\partial t}+\rho\left(u\frac{\partial u}{\partial x}+v\frac{\partial u}{\partial y}+w\frac{\partial u}{\partial z}\right)=-\frac{\partial P}{\partial x}+\mu\nabla^2 u \qquad (\text{II-14})$$

Now apply Reynolds' decomposition, equation (II-14) becomes:

$$\rho\frac{\partial \bar{u}}{\partial t}+\rho\left(\bar{u}\frac{\partial \bar{u}}{\partial x}+\bar{v}\frac{\partial \bar{u}}{\partial y}+\bar{w}\frac{\partial \bar{u}}{\partial z}\right)+\rho\left(\frac{\partial \overline{u'u'}}{\partial x}+\frac{\partial \overline{u'v'}}{\partial x}+\frac{\partial \overline{u'w'}}{\partial x}\right)=-\frac{\partial \bar{P}}{\partial x}+\mu\nabla^2\bar{u} \qquad (\text{II-15})$$

Since the fluid is incompressible, Equation II.15 can be transformed into:

$$\rho\frac{\partial \bar{u}}{\partial t}+\rho\left(\frac{\partial \overline{uu}}{\partial x}+\frac{\partial \overline{uv}}{\partial y}+\frac{\partial \overline{uw}}{\partial z}\right)+\rho\left(\frac{\partial \overline{u'u'}}{\partial x}+\frac{\partial \overline{u'v'}}{\partial x}+\frac{\partial \overline{u'w'}}{\partial x}\right)=-\frac{\partial \bar{P}}{\partial x}+\mu\nabla^2\bar{u} \qquad (\text{II-16})$$

Applying the same operations to the y- and z-momentum equations, we obtain

$$\rho\frac{\partial \bar{v}}{\partial t}+\rho\left(\frac{\partial \overline{vu}}{\partial x}+\frac{\partial \overline{vv}}{\partial y}+\frac{\partial \overline{vw}}{\partial z}\right)+\rho\left(\frac{\partial \overline{v'u'}}{\partial y}+\frac{\partial \overline{v'v'}}{\partial y}+\frac{\partial \overline{v'w'}}{\partial y}\right)=-\frac{\partial \bar{P}}{\partial y}+\mu\nabla^2\bar{v} \qquad (\text{II-17})$$

$$\rho\frac{\partial \bar{w}}{\partial t}+\rho\left(\frac{\partial \overline{wu}}{\partial x}+\frac{\partial \overline{wv}}{\partial y}+\frac{\partial \overline{ww}}{\partial z}\right)+\rho\left(\frac{\partial \overline{w'u'}}{\partial z}+\frac{\partial \overline{w'v'}}{\partial z}+\frac{\partial \overline{w'w'}}{\partial z}\right)=-\frac{\partial \bar{P}}{\partial z}+\mu\nabla^2\bar{w} \qquad (\text{II-18})$$

In vector-tensor format, the above equations can be written succinctly as:

$$\rho\frac{D\vec{\vec{V}}}{Dt}=\rho\frac{\partial\vec{\vec{V}}}{\partial t}+\rho\vec{\vec{V}}\vec{\nabla}.\vec{\vec{V}}=-\vec{\nabla}.\bar{P}-\vec{\nabla}\left(\vec{\vec{\tau}}+\vec{\vec{R}}\right) \qquad (\text{II-19})$$

With

$$\bar{\tau}_{ij}=\begin{vmatrix}\bar{\tau}_{xx} & \bar{\tau}_{xy} & \bar{\tau}_{xz}\\ \bar{\tau}_{yx} & \bar{\tau}_{yy} & \bar{\tau}_{yz}\\ \bar{\tau}_{zx} & \bar{\tau}_{zy} & \bar{\tau}_{zz}\end{vmatrix}$$

$$\overrightarrow{\overrightarrow{R}} = \begin{vmatrix} \overline{u'u'} & \overline{u'v'} & \overline{u'w'} \\ \overline{v'u'} & \overline{v'v'} & \overline{v'w'} \\ \overline{w'u'} & \overline{w'v'} & \overline{w'w'} \end{vmatrix}$$

Where $\bar{\tau}_{ij}$ is the shear tensor and $\overrightarrow{\overrightarrow{R}}$ is the Reynolds stress tensor.

The mean strain rate tensor S is defined as

$$\overrightarrow{\overrightarrow{S}} = \frac{1}{2\mu}\overrightarrow{\overrightarrow{\tau}} \qquad \text{(II-20)}$$

Because there are six unknown quantities, an additional six independent quantities are still needed. These unknown terms, called Reynolds stress terms, are related not only to fluid physical properties but also to local flow conditions. However, no further physical laws are available to resolve them. This is known as the "closure problem" that has plagued turbulence modeling since 1895 to the present and is not going away any time soon. To solve this problem, closure models are used so that we get additional relations between the fluctuating and mean quantities. These closure models generally work well for simple flows but become less and less accurate with an increase in the complexity of flow geometry. Despite this fact they are still widely popular in industry due to their lesser computational resource requirement.

A new quantity was introduced, called "turbulent kinematic viscosity", to relate the fluctuating properties onto the averaged quantities.

$$-\overline{u_i'\phi'} = \nu_t \frac{\partial \bar{\phi}}{\partial x_i} \qquad \text{(II-21)}$$

Where ϕ is any primitive variable, e.g., u, v, w, T, P, ρ, etc.

The kinematic viscosity is based on the fluid type, pressure, and temperature and is a measure of damping. However, the turbulent kinematic viscosity is based on Re, where the higher Re is, the higher the turbulent kinematic viscosity. Thus, the turbulent viscosity is a measure of the degree of turbulence being experienced by the fluid, with higher turbulent viscosities implying a higher degree of turbulence.

Therefore, Reynolds stresses can finally be approximated using the above assumption:

$$R \equiv -\begin{vmatrix} \overline{u'u'} & \overline{u'v'} & \overline{u'w'} \\ \overline{v'u'} & \overline{v'v'} & \overline{v'w'} \\ \overline{w'u'} & \overline{w'v'} & \overline{w'w'} \end{vmatrix} \approx \upsilon_t \begin{vmatrix} \frac{\partial \bar{u}}{\partial x} & \frac{\partial \bar{u}}{\partial y} & \frac{\partial \bar{u}}{\partial z} \\ \frac{\partial \bar{v}}{\partial x} & \frac{\partial \bar{v}}{\partial y} & \frac{\partial \bar{v}}{\partial z} \\ \frac{\partial \bar{w}}{\partial x} & \frac{\partial \bar{w}}{\partial y} & \frac{\partial \bar{w}}{\partial z} \end{vmatrix} \quad \text{(II-22)}$$

The approximation from Eq. (II-21) takes inspiration from the Newtonian stress tensor.

Boussinesq turbulence approximation

The Boussinesq turbulence approximation assumes an analogous expression to the laminar Newtonian stress tensor, thereby asserting that:

$$\vec{\vec{R}} \equiv 2\nu_t \vec{\vec{S}} - \frac{2}{3} k \vec{\vec{I}} = \nu_t \left(\frac{\partial \overline{u_i}}{\partial x_j} + \frac{\partial \overline{u_j}}{\partial x_i} \right) - \frac{2}{3} k I \quad \text{(II-23)}$$

Where k is the turbulence kinetic energy.

The approximation asserts that the Reynolds stress tensor R is proportional to the mean strain rate tensor S, with the proportionality being twice the turbulent kinematic viscosity. The vast majority of the RANS-based turbulence models use this linear constitutive relationship for closure to estimate the Reynolds stresses; this is at the core of many modern one- and two-equation RANS models. In any case, from dimensional analysis and the Newtonian analogy, Boussinesq related the nine Reynolds stresses (with their primed quantities) into averaged quantities.

The three RANS momentum equations can almost be solved numerically for the time-averaged turbulence velocities, $u, v \; and \; w$. Two quantities are needed at this point for closure: (1) an expression for k must somehow be derived for the large, energy-bearing eddies and (2) a relationship for ν_t, which is usually derived using dimensional arguments as functions of k and some characteristic length or equivalent.

II.2.1.1.1 Zero-Equation Models

In this model and as the name designates, no additional transport closure equations is required. A simple algebraic relation is used to close the problem. In direct analogy to the molecular transport

of momentum, Prandtl's mixing length model assumes that the kinematic turbulent viscosity can be expressed as:

$$\nu_t = 2\ell_m\sqrt{S_{ij}S_{ij}} \qquad \text{(II-24)}$$

Where ℓ_m is the mixing length.

Although the zero-equation model is not theoretically sound, it has demonstrated a good prediction for some flows such thin shear layers.

II.2.1.1.2 Prandtl's One-Equation Model

For one-equation models, a turbulence transport variable is used; such variable is predominantly the turbulence kinetic energy, k, in conjunction with auxiliary closure expressions. The first one-equation full-closure turbulence transport model was developed by Ludwig Prandt in 1945. The PDE for the turbulence kinetic energy is expressed as follow [60]:

$$\frac{\partial k}{\partial t} + \overline{u}_j\frac{\partial k}{\partial x_j} = R_{ij}\frac{\partial \overline{u_i}}{\partial x_j} - \varepsilon + \frac{\partial}{\partial x_j}\left[\left(\nu + \frac{\nu_t}{\sigma_k}\right)\frac{\partial k}{\partial x_j}\right] \qquad \text{(II-25)}$$

The dissipation, turbulent kinematic viscosity, and the eddy length scale are defined by Prandtl to provide closure as follow:

$$\varepsilon = \frac{C_D k^{3/2}}{\ell}\ , \nu_t = \ell k^{1/2} \qquad \text{and} \qquad \ell = \kappa y$$

The closure coefficients are:

Kolmogorov's constant, $\kappa = 0.41$, $C_D = 0.3$ (for shear flows) And $C_D \approx C_\mu = 0.085$ (In general)

One-equation models have a somewhat better history for prediction of separated flows; however, they share most of the failures of the mixing length model. The specification of the mixing length by an algebraic formula is still almost entirely dependent on empirical data, and is usually incapable of including transport effects on the length scale [63].

II.2.1.1.3 Two-Equation Models

Two-equation models have been the most popular models for a wide range of engineering analysis and research. It gained popularity and formed the basis for much of the turbulence simulations over the past 40 years. As their name implicates, two PDEs are developed in these models: one for the turbulent kinetic energy and one depends on what type of two-equation model it is. Common choices are the turbulent dissipation, ε , or the specific dissipation, ω .

II.2.1.1.4 Standard $k-\varepsilon$ (SKE) Model

This model was originally presented by Launder and Spalding (1972) although a lot of modified versions now exist [62]. The model transport equations are solved for turbulent kinetic energy k and the turbulent dissipation rate ε . The transport equation for k is given as:

$$\frac{\partial k}{\partial t}+\frac{\partial\left(k\overline{u_i}\right)}{\partial x_j}=\frac{\partial}{\partial x_j}\left[\left(\nu+\frac{\nu_t}{\sigma_k}\right)\frac{\partial k}{\partial x_j}\right]+P_k-\varepsilon \qquad \text{(II-26)}$$

and the transport equation for ε is given as:

$$\frac{\partial \varepsilon}{\partial t}+\frac{\partial\left(\varepsilon\overline{u_i}\right)}{\partial x_j}=\frac{\partial}{\partial x_j}\left[\left(\nu+\frac{\nu_t}{\sigma_\varepsilon}\right)\frac{\partial \varepsilon}{\partial x_j}\right]+C_{\varepsilon 1}\frac{\varepsilon}{k}P_k-C_{\varepsilon 2}\frac{\varepsilon^2}{k} \qquad \text{(II-27)}$$

Where P_k is the production term and is given as:

$$P_k=-\overline{u_i'u_j'}\frac{\partial\overline{u_i}}{\partial x_j} \qquad \text{(II-28)}$$

Using Boussinesq approximation, equation (II-28) becomes:

$$P_k=2\nu_t S_{ij}S_{ij} \qquad \text{(II-29)}$$

The turbulent viscosity for this model is approximated as

$$\nu_t=C_\mu\frac{k^2}{\varepsilon} \qquad \text{(II-30)}$$

The constant parameters used in the above equations take the following values:

$$C_\mu=0.09;\ \sigma_k=1.00;\ \sigma_k=1.30;\ C_{1\varepsilon}=\ 1.44\ and\ C_{2\varepsilon}=1.92$$

II.2.1.1.5 Standard $k-\omega$ Model

The standard $k-\omega$ model was developed by Wilcox (1988) and over the years has become a widely popular model. The model is very similar in structure to the $k-\varepsilon$ model but the variable ε is replaced by the dissipation rate per unit kinetic energy ω. The model consists of transport equation for *k* given by:

$$\frac{\partial k}{\partial t}+\frac{\partial\left(k\overline{u_i}\right)}{\partial x_j}=\frac{\partial}{\partial x_j}\left[\left(\nu+\frac{\nu_t}{\sigma_k}\right)\frac{\partial k}{\partial x_j}\right]+P_k-\varepsilon \qquad \text{(II-31)}$$

and a transport equation for ω given as:

$$\frac{\partial \omega}{\partial t}+\frac{\partial\left(\omega\overline{u_i}\right)}{\partial x_j}=\frac{\partial}{\partial x_j}\left[\left(\nu+\frac{\nu_t}{\sigma_\omega}\right)\frac{\partial \omega}{\partial x_j}\right]+\frac{\alpha}{\nu_t}P_k-\beta\omega^2 \qquad \text{(II-32)}$$

The turbulent viscosity and dissipation rate of k are now defined as:

$$\nu_t=\alpha^*\frac{k}{\omega} \quad and \quad \varepsilon=\beta^* k\omega$$

The model coefficients take the following values:

$$\sigma_k=2.0,\sigma_\varepsilon=2.0,\alpha=5/9,\alpha^*=1.0,\beta=0.075\ and\ \beta^*=0.09$$

II.2.1.1.6 Shear-Stress Transport (SST) Model

The SST K-ω turbulence model developed by Menter (1994) [64], combines the advantages of the original k-ε model and the standard k-ω model. It has been widely used due to its accurate description of the physics of the flow and its numerical stability. The model can be written as follows [65-68]:

$$\frac{\partial \rho\overline{u_j}k}{\partial x_j}=\frac{\partial}{\partial x_j}\left[\left(\mu+\sigma_k\mu_t\right)\frac{\partial k}{\partial x_j}\right]+P_k-B^*\rho\omega k \qquad \text{(II-33)}$$

$$\frac{\partial \rho\overline{u_j}\omega}{\partial x_j}=\frac{\partial}{\partial x_j}\left[\left(\mu+\sigma_\omega\mu_t\right)\frac{\partial \omega}{\partial x_j}\right]+P_\omega-\beta\rho\omega^2+2(1-f_1)\frac{\rho\sigma_{\omega 2}}{\omega}\frac{\partial k}{\partial x_j}\frac{\partial \omega}{\partial x_j} \qquad \text{(II-34)}$$

With P_k and P_ω are the production terms of the term k and the term ω, and μ_t is the turbulent viscosity.

The P_k and P_ω can be expressed as:

$P_k = \mu_t \Omega^2$ *and* $P_\omega = C_\omega \rho \Omega^2$

Where Ω is the vorticity magnitude.

The turbulent viscosity μ_t is defined as:

$$\mu_t = \frac{a_1 \rho K}{max\left(a_1 \omega, f_2 \|\Omega\|\right)} \quad \text{(II-35)}$$

Where:

$$\phi = f_1 \phi_1 + (1 - f_1)\phi_2,\ f_1 = tanh\left(\Gamma_1^4\right)$$

$$\Gamma_1 = min\left[max\left(\frac{\sqrt{K}}{0.09\omega d}, \frac{500\mu}{\rho \omega d^2} \right), \frac{4\rho\sigma_{\omega 2} K}{CD_{K\omega} d^2} \right] CD_{K\omega} \quad \text{(II-36)}$$

$$f_2 = tanh\left(\Gamma_2^4\right), \Gamma_2 = max\left(\frac{2\sqrt{K}}{0.09\omega d}, \frac{500\mu}{\rho \omega d^2} \right) \quad \text{(II-37)}$$

d is the distance to the nearest wall

The constants are as follow:

$K = 0.41, a_1 = 0.31, \sigma_{k1} = 0.85, \sigma_{k2} = 1.0, \sigma_{k1} = 0.85, \sigma_{\omega 1} = 0.5$

$\sigma_{\omega 2} = 0.856, \beta_1 = 0.075, \beta_2 = 0.0828, C_{\omega 1} = 0.533, C_{\omega 2} = 0.44$

II.2.1.2 Non-Statistical Approaches

II.2.1.2.1 Direct Numerical Simulation (DNS)

DNS is a turbulence approach that solves the unsteady Navier-Stokes equations such that all turbulence scales are resolved with no modelling assumptions are used. It is the most straight-forward approach in solving turbulent flow problems. DNS requires multiple high mesh resolution that can be in order of tens of millions to billions of computational nodes (Day et al. 2009). The mesh size is a function of the Reynolds number, the higher the Re, the higher the required node count because eddies become smaller.

It is found that DNS results corroborate well the experimental data when fine enough mesh and higher order accurate numerical schemes are used. Furthermore, DNS provides much more detailed data which are sometimes even difficult to measure by experiments. The main limitations of DNS are the high computational cost and the need for higher order accurate discretization techniques. With the increasing in computational power, DNS will not only be used for turbulence research and small systems but for larger engineering designs.

II.2.1.2.2 Large Eddy Simulation

Large Eddy Simulation (LES) is the process in which a filtering method is applied to separate large eddies from smaller ones instead of modelling everything like RANS. The larger eddies contain most of the turbulent kinetic energy that is obtained from bulk fluid energy. These eddies are responsible for the majority of the diffusive processes involving mass, momentum, and energy. For these reasons, the simulation of large eddies is highly desirable. However, the smaller eddies take the kinetic energy from the larger eddies and transfer their energy back to the fluid through viscous shear. For high Re, the small-scale turbulent eddies are statistically isotropic. As a result, and based on Kolmogorov principles, these small scales of motion can be modelled, however the larger scales which depend on boundary and flow conditions are calculated like *DNS*. LES can be considered as an intermediate methodology between RANS and DNS, and it is a balance between output and computational effort.

In LES, a filter function based on cell volume size is used to distinguish between the large scales and small scales. The computational approach is achieved by choosing a filtering length scale, Δ. In particular, if the eddy size is greater than Δ, such eddy is resolved, however it is modeled when the eddy is smaller than Δ.

1. Filtering In LES

Filtering is applied to introduce the separation of resolved scales from unresolved ones. Typically, the filtering strategy employs a filter function G that involves the parameter Δ. Then, as a general and well-proven LES approach, the large eddy filtered velocity is obtained by employing a "convolution filter" as follows:

$$\overline{u_i}\left(\vec{x},t\right)=\iiint G\left(\vec{x},\vec{x'}\right)u_i\left(\vec{x},t\right)d^3\vec{x} \qquad \text{(II-38)}$$

In particular, the LES velocity field is averaged in space (vs. RANS, which is averaged in time). Therefore, the entire LES velocity field is given by:

$$u_i=\sum\left(resolved+subgrid\right)=\overline{u_i}+u_i'$$

To produce the filtered large eddy velocity, a convolution takes the instantaneous velocity and filters it as a function of eddy dimension Δ. Thus, the direct consequence of the filtering operation is to eliminate the small fluctuations from u_i. The most commonly used filters are box filter. It includes the element volume Δ^3 in its filtering criteria for cutoff. It is defined as:

$$G\left(\vec{x}-\vec{x}';\Delta\right)=\begin{cases}1/\Delta^3, \left\|x-x'\right\|\le \Delta/2\\ 0\ otherwise\end{cases} \qquad \text{(II-39)}$$

$$\Delta=\sqrt[3]{\Delta x\,\Delta y\,\Delta z} \qquad \text{(II-40)}$$

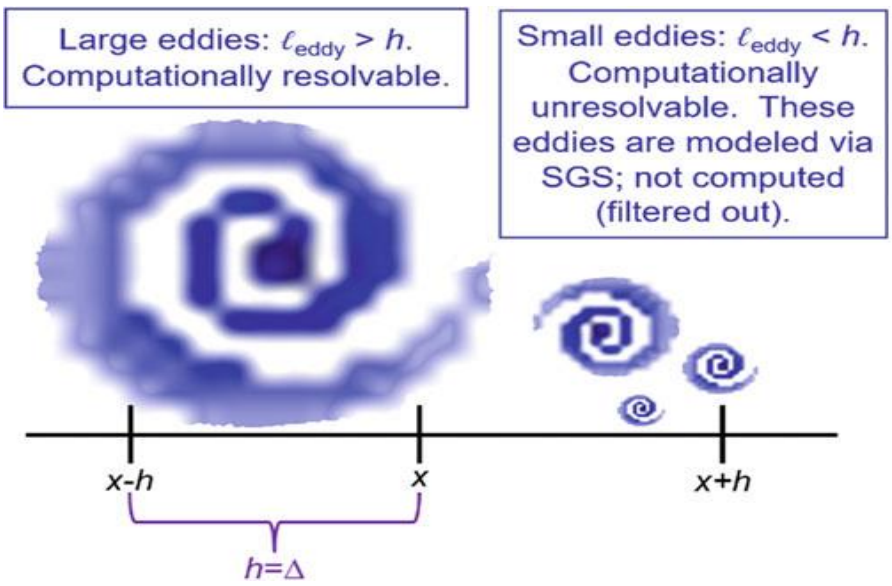

Figure II-4: filter process in LES [60]

2. LES Mass and Momentum Conservation

Assume an incompressible, Newtonian flow, the unfiltered conservation of mass PDE is given by:

$$\frac{\partial u_i}{\partial x_i} = 0 \qquad \text{(II-41)}$$

And the unfiltered momentum conservation PDE is as follow:

$$\frac{\partial u_i}{\partial t} + \frac{\partial \left(u_i u_j\right)}{\partial x_j} = -\frac{1}{\rho}\frac{\partial \tau_{ij,lam}}{\partial x_i} - \frac{1}{\rho}\frac{\partial P}{\partial x_i} = \frac{\mu}{\rho}\frac{\partial}{\partial x_j}\left(\frac{\partial u_i}{\partial x_j} + \frac{\partial u_j}{\partial x_i}\right) - \frac{1}{\rho}\frac{\partial P}{\partial x_i} \qquad \text{(II-42)}$$

With

$$\tau_{ij,lam} = -\mu\left(\frac{\partial u_i}{\partial x_j} + \frac{\partial u_j}{\partial x_i}\right) \qquad \text{(II-43)}$$

To derive the LES momentum equation, we perform the LES space-filtering operation for the unfiltered NS equation:

$$\frac{\partial \overline{u_i}}{\partial t} + \frac{\partial \left(\overline{u_i u_j}\right)}{\partial x_j} = \frac{\mu}{\rho}\frac{\partial}{\partial x_j}\left(\frac{\partial \overline{u_i}}{\partial x_j} + \frac{\partial \overline{u_j}}{\partial x_i}\right) - \frac{1}{\rho}\frac{\partial \overline{P}}{\partial x_i} \qquad \text{(II-44)}$$

Note that the convective $\overline{u_i u_j}$ term is unknown, so some mathematics and physics are required. The convective ($\overline{u_i u_j}$) component is breaking as below:

$$\overline{u_i u_j} = \overline{\left(\overline{u_i} + u_i'\right)\left(\overline{u_j} + u_j'\right)} = \overline{\overline{u_i}\,\overline{u_j}} + \overline{\overline{u_i}\,u_j'} + \overline{u_i'\,\overline{u_j}} + \overline{u_i'\,u_j'} \qquad \text{(II-45)}$$

At this point, more succinct and universal notation can be used to represent the tensors that were derived from the convective term, namely,

$$\overline{u_i u_j} = \overline{\overline{u_i}\,\overline{u_j}} + \overline{\overline{u_i}\,u_j'} + \overline{u_i'\,\overline{u_j}} + \overline{u_i'\,u_j'} = \overline{u_i}\,\overline{u_j} + C_{ij} + L_{ij} + R_{ij} \qquad \text{(II-46)}$$

Where

$C_{ij} = \overline{\overline{u_i}\,u_j'} + \overline{u_i'\,\overline{u_j}}$: Cross term stress (Clark et al :1979)

$L_{ij} = \overline{\overline{u_i}\,\overline{u_j}} - \overline{u_i}\,\overline{u_j}$: Leonard stress (Leonard 1974; Stefano and Vasilyev 2002)

$R_{ij} = \overline{u_i' u_j'}$: SGS Reynolds stress (Clark et al:1979)

Analyzing the above terms, we see that the Leonard stress tensor has only the resolved scales in it, thus we can say that the Leonard stress represents the interaction between the large scales and might be responsible for transferring the energy to the unresolved small scales. Since the Leonard stress tensor contains only the resolved scales one can easily calculate the stresses from the resolved or filtered velocities. However, the cross stress tensor has cross product of filtered and unfiltered fields in it, this means it has two known terms and two unknowns, but as a whole it is an unknown quantity and needs to be modelled. This cross-stress term shows the interaction between the resolved and the unresolved scales and is hence responsible for the transferring of energy from large to small scales or small to large scales. It is inversely proportional to the Reynolds number. This term cannot be computed directly; it must be approximated. The final term in equation (II-46) is the Reynolds stress which contains only the unresolved scales and needs to be approximated.

Thus, the LES space-filtered NS can be written as [60]:

$$\frac{\partial \overline{u_i}}{\partial t} + \frac{\partial\left(\overline{u_i}\,\overline{u_j} + C_{ij} + L_{ij} + R_{ij}\right)}{\partial x_j} = \frac{\mu}{\rho}\frac{\partial}{\partial x_j}\left(\frac{\partial \overline{u_i}}{\partial x_j} + \frac{\partial \overline{u_j}}{\partial x_i}\right) - \frac{1}{\rho}\frac{\partial \overline{P}}{\partial x_i} \qquad \text{(II-47)}$$

Rearranging terms of equations (II-47), after space-averaged exact LES PDE is given as:

$$\frac{\partial \overline{u_i}}{\partial t} + \frac{\partial\left(\overline{u_i}\,\overline{u_j}\right)}{\partial x_j} = \frac{\mu}{\rho}\frac{\partial}{\partial x_j}\left(\frac{\partial \overline{u_i}}{\partial x_j} + \frac{\partial \overline{u_j}}{\partial x_i}\right) - \frac{\partial\left(C_{ij} + L_{ij} + R_{ij}\right)}{\partial x_j} - \frac{1}{\rho}\frac{\partial \overline{P}}{\partial x_i} \qquad \text{(II-48)}$$

The previous space-filtered NS form is conveniently reformulated as follows,

$$\frac{\partial \overline{u_i}}{\partial t} + \frac{\partial\left(\overline{u_i}\,\overline{u_j}\right)}{\partial x_j} = \frac{\mu}{\rho}\frac{\partial}{\partial x_j}\left[\underbrace{\left(\frac{\partial \overline{u_i}}{\partial x_j} + \frac{\partial \overline{u_j}}{\partial x_i}\right)}_{Large\ resolved\ eddies} - \underbrace{\tau_{ij}}_{Small\ modeled\ eddies}\right] - \frac{1}{\rho}\frac{\partial \overline{P}}{\partial x_i} \qquad \text{(II-49)}$$

Where

$$\tau_{ij} \equiv C_{ij} + L_{ij} + R_{ij} \equiv \overline{u_i u_j} - \overline{u_i}\,\overline{u_j} \equiv SGS\ Model$$

3. Subgrid Scale Modelling SGS

In the LES approach, the model is divided into two parts: the large scales and the small scales. The large scales solved by the Navier Stokes equations however the small scales have to be modelled. The latter scales can be approximated using a modeling approach since the small scales are isotropic

and universal. These models are known as the Subgrid scale models (SGS). Variety of SGS models have been developed to approximate the SGS Reynolds stress. The Smagorinsky model presented in 1963 is the oldest. The SGS models can be classified into two categories: the first classes are the models that are based on the concept of eddy viscosity and the other classes of models are scale similarity models, transport models and de-convolution models.

3.1. Eddy viscosity models

For Eddy viscosity models, the local energy events associated with convection and diffusion can be neglected and only global effects of SGS terms such as dissipation are important. Another assumption in Eddy viscosity models is that the rate of production of energy is equal to the rate of dissipation. This latter is known as equilibrium hypothesis and is defined as [62]:

$$\varepsilon = -\tau_{ij}\overline{S_{ij}} \qquad \text{(II-50)}$$

3.2. Smagorinsky model

The Smagorinsky model (Smagorinsky 1963) is the simplest and most commonly used eddy-viscosity model. The basic concept behind this model is that dimensionally viscosity is a product of length scale and velocity scale [62].

$$\nu_t \propto u_{sgs}\Delta \qquad \text{(II-51)}$$

Where u_{sgs} is the subgrid scale velocity and Δ is the filter width.

Using the Boussinesq approximation can be written as [62]:

$$\tau_{ij} - \frac{\delta_{ij}}{3}\tau_{kk} = -2\nu_t\overline{S_{ij}} = \nu_t\left(\frac{\partial\overline{u_i}}{\partial x_j} + \frac{\partial\overline{u_j}}{\partial x_i}\right) \qquad \text{(II-52)}$$

Coupling the above equation with equilibrium equation, we obtain:

$$\varepsilon = -\tau_{ij}\overline{S_{ij}} = 2\nu_t\overline{S_{ij}}\,\overline{S_{ij}} - \frac{\delta_{ij}}{3}\tau_{kk}\overline{S_{ij}} \qquad \text{(II-53)}$$

Where τ_{ij} is the subgrid scale stress, ν_t is the eddy viscosity and S_{ij} is the resolved strain rate tensor.

From equation (II-53) We can state that:

$$\varepsilon \propto 2\nu_t\overline{S_{ij}}\,\overline{S_{ij}} \qquad \text{(II-54)}$$

Inserting value of ν_t from Equation (II-51) we get

$$\varepsilon \propto 2\, u_{sgs}\, \Delta\, \overline{S_{ij}}\,\overline{S_{ij}} \qquad \text{(II-55)}$$

The Kolmogorov hypothesis states that the rate of dissipation is proportional to:

$$\varepsilon \propto \frac{u_{sgs}^3}{\Delta} \qquad \text{(II-56)}$$

Therefore, we can get an estimation of u_{sgs} as:

$$u_{sgs} \propto \Delta \sqrt{2\, \overline{S_{ij}}\,\overline{S_{ij}}} \qquad \text{(II-57)}$$

So, the subgrid scale viscosity is proportional to:

$$\nu_t \propto \Delta^2 \sqrt{2\, \overline{S_{ij}}\,\overline{S_{ij}}} \qquad \text{(II-58)}$$

And introducing a Smagorinsky constant we get,

$$\nu_t = C_s\, \Delta^2 \sqrt{2\, \overline{S_{ij}}\,\overline{S_{ij}}} \qquad \text{(II-59)}$$

For the value of Smagorinsky constant C_s , Some authors use $0.1 \le C_s \le 0.3$ (Tutar and Holdo 2001), while others use $0.1 \le C_s \le 0.24$ (Fuego 2016a). For large Re and isotropic flows, the standard Smagorinsky model is suitable, however, for low Re number it is not as good. Zhiyin 2015 have pointed out that this model is too dissipative near the laminar to turbulent transition for low Reynolds number. Another shortcoming of the model is flows are not well-resolved when there is a large deviation from isotropy (anisotropic).

3.3. Dynamic Smagorinsky Model

The dynamic Smagorinsky model automatically calculates C_s in both space and time as the calculation proceeds based on the information provided by the resolved scales of motion. In the dynamic model, an additional test filter is applied. The difference between the test filter and grid filter leads to an estimate of the dynamic Smagorinsky coefficient C_{dyn} . Germano and Lilly conceived a procedure in which the Smagorinsky model constant, C_s is dynamically computed.

Unfortunately, the standard Smagorinsky calculates a nonzero value for ν_t at the wall, so some LES models use a damping function such as van Driest. Nevertheless, for LES and DNS turbulence modeling, this issue can be overcome by using sufficiently discretized resolution near the wall, without having to use damping functions (but at a higher computational cost) (Rodi et al. 1997; Tutar and Holdo 2001; Zhiyin 2015). Given the choice between the 1963 Smagorinsky model and the

dynamic Smagorinsky model, the latter is preferred because of its ability to calculate Cs as a function of space and time based on turbulence dynamics (Germano et al. 1991; Lilly 1992), and there is no need to specify Cs a priori based on flow type; a "constant" CS can never fully represent a dynamic situation involving spatial and temporal changes. Newer models with reduced dissipation near the wall and during transition have been developed recently (Vreman 2004), with excellent comparison with DNS for friction coefficients in channel flow. In addition, the σ-SGS model captures the cubic y dependence near the wall (Nicoud et al. 2011). Certainly, more validation is desirable.

Recalling that the grid filtered Navier-Stokes equations are given as [62]:

$$\frac{\partial \overline{u_i}}{\partial t}+\frac{\partial\left(\overline{u_i}\,\overline{u_j}\right)}{\partial x_j}=\nu\frac{\partial}{\partial x_j}\left[\left(\frac{\partial \overline{u_i}}{\partial x_j}+\frac{\partial \overline{u_j}}{\partial x_i}\right)-\tau_{ij}\right]-\frac{1}{\rho}\frac{\partial \overline{P}}{\partial x_i} \qquad \text{(II-60)}$$

The test filter is done by:

$$f(x)=\int f(x')\,G(x,x')\,dx' \qquad \text{(II-61)}$$

Applying the test filter to the filtered Navier-Stokes equations leads to:

$$\frac{\partial \overline{u_i}}{\partial t}+\frac{\partial\left(\overline{u_i}\,\overline{u_j}\right)}{\partial x_j}=\nu\frac{\partial}{\partial x_j}\left[\left(\frac{\partial \overline{u_i}}{\partial x_j}+\frac{\partial \overline{u_j}}{\partial x_i}\right)-T_{ij}\right]-\frac{1}{\rho}\frac{\partial \overline{P}}{\partial x_i} \qquad \text{(II-62)}$$

Where the test filtered subgrid-scale stresses is given as:

$$T_{ij}=\overline{u_i u_j}-\overline{u_i}\,\overline{u_j} \qquad \text{(II-63)}$$

Now we define the resolved turbulent stresses (ζ_{ij}) which represents the contribution of the Reynolds stresses of the scales which have a length scale smaller than the test filter and bigger than the grid filter [69].

$$\zeta_{ij}=\overline{u_i}\,\overline{u_j}-\overline{u_i}\,\overline{u_j} \qquad \text{(II-64)}$$

Germano (1990) proposed an algebraic relationship for the resolved turbulent stresses as bellow:

$$\zeta_{ij}=T_{ij}-\tau_{ij} \qquad \text{(II-65)}$$

Using Boussinesq approximation and the expression of SGS viscosity, we get

$$\tau_{ij} - \frac{\delta_{ij}}{3}\tau_{kk} = -2\nu_t \overline{S_{ij}} = -2\, C_s\, \Delta^2 \sqrt{2\, \overline{S_{ij}}\,\overline{S_{ij}}}\; \overline{S_{ij}} \qquad \text{(II-66)}$$

$$T_{ij} - \frac{\delta_{ij}}{3}T_{kk} = -2\nu_t \overline{S_{ij}} = -2\, C_s\, \Delta^2 \sqrt{2\, \overline{S_{ij}}\,\overline{S_{ij}}}\; \overline{S_{ij}} \qquad \text{(II-67)}$$

Now substituting values of τ_{ij} and $\tilde{\tau}_{ij}$ from equations (II-66) and (II-67) into equation (II-65) yields

$$\zeta_{ij} = \tau_{ij} - \tau_{ij} = \left(-2\, C_s\, \Delta^2 \left|\overline{S_{ij}}\right| \overline{S_{ij}}\right) - \left(-2\, C_s\, \Delta^2 \left|\overline{S_{ij}}\right| \overline{S_{ij}}\right) \qquad \text{(II-68)}$$

Where

$$\left|\overline{S_{ij}}\right| = \sqrt{2\, \overline{S_{ij}}\,\overline{S_{ij}}} \;\; \textit{and} \;\; \left|\overline{S_{ij}}\right| = \sqrt{2\, \overline{S_{ij}}\,\overline{S_{ij}}} \qquad \text{(II-69)}$$

Computing the tested filtered quantities by external filtering, we can calculate the C_s, which is the only unknown of equation (II-68). However, we cannot determinate the Smagorinsky coefficient if the right hand side of equation (II-68) equals zero, this leads ill-conditioned system. The coefficient is computed at every spatial grid point and every time step, directly from the current resolved variables. Two significant improvements to the original model proposed by Germano et al. (1991). Lilly (1992) proposed a least-squares procedure for evaluating the coefficient. The second improvement has done by Wong and Lilly (1994) in which they introduced new base model to replace the Smagorinsky model.

3.4. Wall-Adapting Local Eddy-Viscosity Model (WALE)

Wray and Hunt (1989) showed from DNS of isotropic turbulence that energy is actually concentrated around zones of vorticity and strain. Thus, using only the strain rate like in the Smagorinsky model is inadequate. For this purpose, Nicoud and Ducros (1999) developed a new model based on the square of velocity gradient tensor that accounts for the effects of both the strain and the rotation rate of the smallest resolved turbulent fluctuations.

For subgrid-scale viscosity modelling the WALE model is finally proposed as [62]:

$$\nu_t = (C_w \Delta)^2 \frac{(\overline{S}^d : \overline{S}^d)^{3/2}}{(\overline{S} : \overline{S})^{5/2} + (\overline{S}^d : \overline{S}^d)^{5/4}} \qquad \text{(II-70)}$$

Where the traceless symmetric tensor $\overline{S}^d$ reads [56]:

$$S_{ij}^{d} = (\bar{g}_{ij}^{2} + \bar{g}_{ji}^{2})/2 - \bar{g}_{kk}^{2}\delta_{ij}/3 \qquad \text{(II-71)}$$

with $\bar{g}_{ij} = \partial \bar{u}_i / \partial x_j$, $\bar{g}_{ij}^{2} = \bar{g}_{ik}\bar{g}_{kj}$, and δ_{ij} is the Kronecker tensor (in terms of components). Here, the Einstein summation convention applies.

The salient points of the relationship (II-70) are threefold: 1) ν_t involves the strain and rotation tensors, thereby allowing to pick up turbulent structures relevant for the kinetic energy dissipation, 2) ν_t automatically tends towards zero near the wall with appropriate scaling ($\propto y^{+3}$), and 3) ν_t can be neither negative nor infinite.

CHAPTER III: FLUID FLOW PAST A WALL MOUNTED CUBE

III.1 Introduction

Improving the cooling effectiveness is still the main challenge in various types of electronic systems and many other compact heats dissipated devices [70]. In this context, we emphasize on study the cooling enhancement of electronic components with a geometry modification on the top edge. The component is of cubic form placed in a channel and exposed to two streams: cross flow and impinging jet stream. In this chapter, twelve cases were investigated and analyzed in terms of flow morphology and heat transfer efficiency.

III.2 Case Description and numerical approach

The studied case consists of a cube object representing an electronic component placed in the center of a square channel subjected to a cross-flow and a perpendicular impinging jet. The computational setup is similar to the experimental conditions of Massip et al. [29] where our numerical results are validated with those of this experiment. The sketch of the computational domain geometry including boundary conditions are shown in Fig. III-1. The height of the component is 15 mm and the total length of the channel (x axis) is fixed to 20h, where h is the height of the cube. The width of the channel is 15h and the domain height in the spanwise direction (y axis) is 2h. The dynamic and the thermal behaviour of the flow past four different cube configurations is investigated based on the radius of the rounded top corner which ranges from 0 to 6 mm with an increment of 2 mm. Incompressible air is used as the cooling fluid with a temperature of 293 K. The study was carried out at a cross flow Reynolds number of 3410 based on the inlet cross flow velocity (U_H) and the channel height (H=2h). In addition to the channel flow, the component is exposed to a perpendicular impinging jet where three impinging to cross flow Reynolds number ratios are investigated ($\alpha = \mathrm{Re}_j / \mathrm{Re}_H = 0.5, 1 \; and \; 1.5$). In total, twelve (12) cases were computed. The channel flow and the impinging jet flow streams are imposed as inlet boundary conditions with a temperature of 293 K. At the exit, an outlet relative pressure is imposed (P= 0 pa). No-slip smooth walls are considered for the remaining boundaries with a temperature equals to the fluid temperature (293 K) except for the heated cube where the temperature is fixed to 348 K. To sum up, Table III.1 summarises further details.

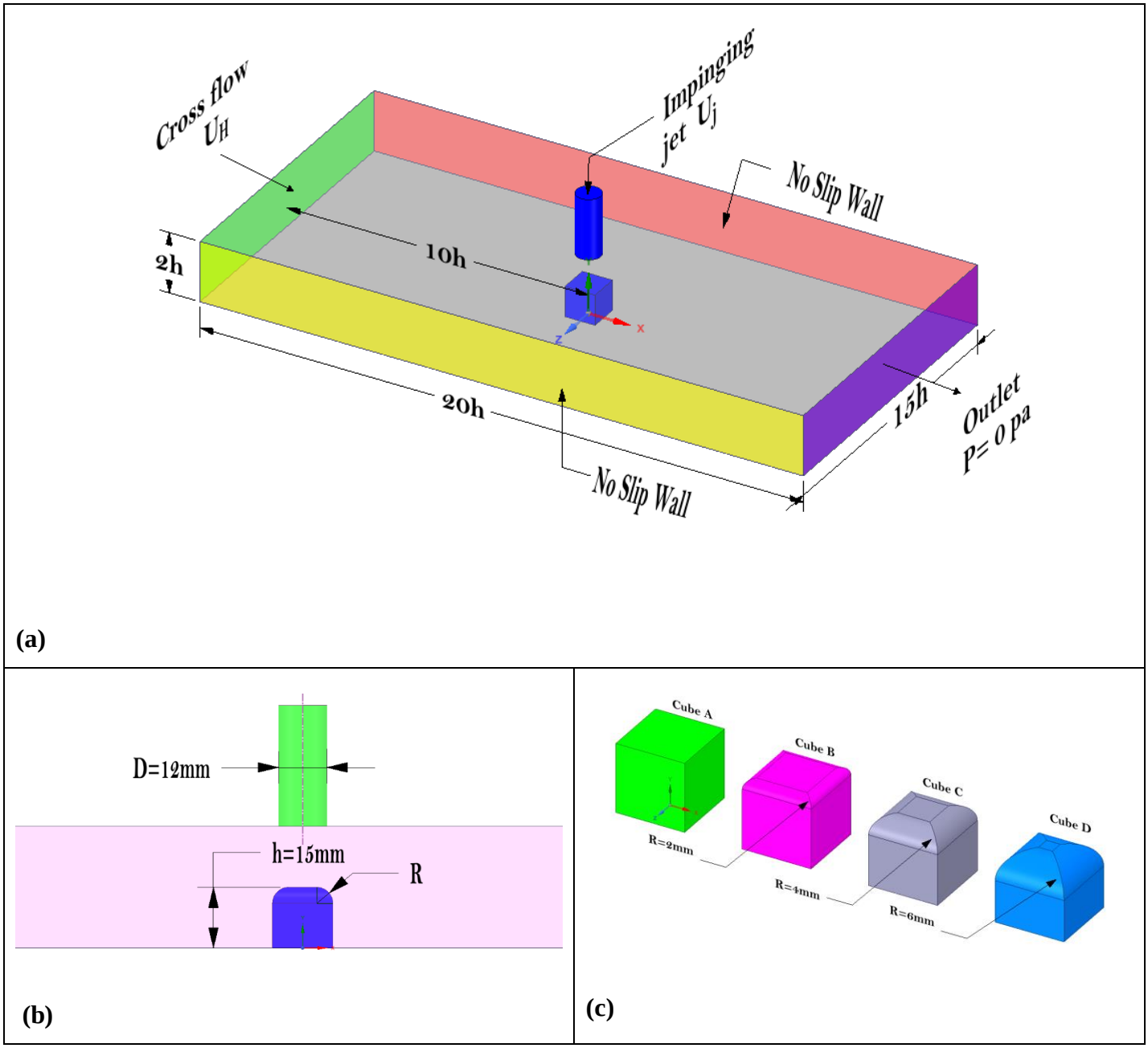

Figure III-1: (a) Sketch of the computational domain including boundary conditions: (b) Cross-sectional views, (c) cube geometries.

Table III-1: Simulation Settings parameters and boundary conditions

Settings parameters	
Simulation type	3D steady
Turbulence model	SST K-ω
Convergence criterion	10^{-5}
Cylinder diameter	$d = 12mm$
Cube height	$h = 15mm$
Cross flow Reynolds number	$Re_H = 3410$
Jet Impinging to cross flow ratio	$\alpha = Re_j / Re_H = 0.5, 1$ and 1.5
CFD code	Ansys™ Fluent package
BCs	
Inlet cross flow	$U_{in} = 1.705\ ms^{-1}$ & $T = 293K$
Outlet	Relative pressure: $P_{out} = 0\ Pa$
All walls	No-slip wall: $U = 0$
Cube walls	Temperature T = 348 K
Channel walls	Temperature T = 293 K

III.3 Turbulence modeling:

In the present work we have assumed that the fluid is incompressible and that the flow is statistically steady. The continuity, momentum and energy equations (RANS equations) can be written in the differential form and using the tensor notation as [71-73]:

$$\frac{\partial U_i}{\partial x_i} = 0 \qquad \text{(III-1)}$$

$$\rho \frac{\partial \left(U_i U_j\right)}{\partial x_j} = -\frac{\partial P}{\partial x_i} + \frac{\partial}{\partial x_j}\left[\mu\left(\frac{\partial U_i}{\partial x_j} + \frac{\partial U_j}{\partial x_i}\right) - \rho\overline{u_i' u_j'}\right] \qquad \text{(III-2)}$$

$$\rho C_p U_i \frac{\partial T}{\partial x_i} = \frac{\partial}{\partial x_i}\left[\lambda \frac{\partial T}{\partial x_i} - \rho C_p \overline{u_i' T'}\right] \qquad \text{(III-3)}$$

Where U_i and T denote the mean velocity and temperature; μ is the dynamic viscosity; ρ is the fluid density; P is the pressure; C_p specific heat capacity at constant pressure, λ is the thermal conductivity; u_i', u_j' and T' are the corresponding fluctuation components; $-\rho\overline{u_i'u_j'}$ and $-\rho C_p\overline{u_i'T'}$ are the average Reynolds stresses and turbulent heat fluxes which need to be modelled to close the equations [74-76].

No slip condition is assumed at the channel walls and cube faces

$$U = 0_{|walls} \qquad \text{(III-4)}$$

In this work, the SST K-ω model is based on the Boussinesq eddy-viscosity hypothesis that determines the Reynolds stresses from [77]:

$$-\rho\overline{u_i'u_j'} = \mu_t\left(\frac{\partial U_i}{\partial x_j}+\frac{\partial U_j}{\partial x_i}\right)-\frac{2}{3}\left(\rho k+\mu_t\frac{\partial U_i}{\partial x_i}\right)\delta_{ij} \qquad \text{(III-5)}$$

Where μ_t is the turbulent viscosity, k is the turbulent kinetic energy, δ_{ij} is the strain rate tensor. Using the Boussinesq approximation, where the heat flux is assumed to be proportional to the turbulent eddy viscosity, the turbulent heat fluxes can be expressed as [78]

$$-\rho\overline{u_i'T'} = \frac{\mu_t}{\mathrm{Pr}_t}\frac{\partial T}{\partial x_i} \qquad \text{(III-6)}$$

Where Pr_t is the turbulent Prandtl number, a property of turbulent flow that can be considered as a parameter to evaluate the turbulence mixing efficiency. For this study $\mathrm{Pr}_t = 0.85$.

The SST K-ω turbulence model developed by Menter [64] combines the advantages of the original k-ε model and the standard k-ω model. It has been widely used due to its accurate description of the physics of the flow and its numerical stability. The model can be written as follows [67-68 : 79-80]

$$\frac{\partial \rho U_j k}{\partial x_j} = \frac{\partial}{\partial x_j}\left[\left(\mu+\sigma_k\mu_t\right)\frac{\partial k}{\partial x_j}\right]+P_k-B^*\rho\omega k \qquad \text{(III-7)}$$

$$\frac{\partial \rho U_j \omega}{\partial x_j} = \frac{\partial}{\partial x_j}\left[\left(\mu+\sigma_\omega\mu_t\right)\frac{\partial \omega}{\partial x_j}\right]+P_\omega-\beta\rho\omega^2+2(1-f_1)\frac{\rho\sigma_{\omega 2}}{\omega}\frac{\partial k}{\partial x_j}\frac{\partial \omega}{\partial x_j} \qquad \text{(III-8)}$$

With k denoting the turbulent kinetic energy, ω is the turbulent dissipation rate, $\mathrm{P_k}$ and $\mathrm{P_\omega}$ are the production terms of the term k and the term ω, and μ_t is the turbulent viscosity.

The $\mathrm{P_k}$ and $\mathrm{P_\omega}$ can be expressed as:

$P_k = \mu_t \Omega^2$ *and* $P_\omega = C_\omega \rho \Omega^2$

Where Ω is the vorticity magnitude.

The turbulent viscosity μ_t is defined as:

$$\mu_t = \frac{a_1 \rho K}{max\left(a_1 \omega, f_2 \|\Omega\|\right)} \quad \text{(III-9)}$$

$$\phi = f_1 \phi_1 + (1 - f_1)\phi_2, \; f_1 = tanh\left(\Gamma_1^4\right)$$

$$\Gamma_1 = min\left[max\left(\frac{\sqrt{K}}{0.09\omega d}, \frac{500\mu}{\rho \omega d^2} \right), \frac{4\rho\sigma_{\omega 2} K}{CD_{K\omega} d^2} \right] CD_{K\omega} \quad \text{(III-10)}$$

$$f_2 = tanh\left(\Gamma_2^4\right), \Gamma_2 = max\left(\frac{2\sqrt{K}}{0.09\omega d}, \frac{500\mu}{\rho \omega d^2} \right) \quad \text{(III-11)}$$

d is the distance to the nearest wall.

The constants are as follow:

$$K = 0.41, a_1 = 0.31, \sigma_{k1} = 0.85, \sigma_{k2} = 1.0, \sigma_{k1} = 0.85, \sigma_{\omega 1} = 0.5$$
$$\sigma_{\omega 2} = 0.856, \beta_1 = 0.075, \beta_2 = 0.0828, C_{\omega 1} = 0.533, C_{\omega 2} = 0.44$$

The local Nusselt number can be obtained by:

$$Nu = \frac{h\, q}{\lambda\,(T_w - T_b)} \quad \text{(III-12)}$$

Where, T_w and T_b are the local temperature of the heated cube and the local bulk temperature of the fluid, respectively; q is the heat flux.

III.4 Meshing implementation and dependency

In order to achieve simulation convergence quickly with sufficient precision, the mesh must be generated with great attention. The grid was non uniform, with high density in zones of high gradient and low density is adopted in zones of less interest, so that minimal computational effort was required while gaining sufficient accuracy [81]. A structured hexahedral mesh is employed in these simulations and is generated using ANSYS™ ICEM. Fig. III-2a displays the mesh generation in the computational domain. Fig. III-2b shows the grid near the cube surface of the domain. Near the cube and walls, very fine meshes are implemented to resolve boundary layer separation and the vortex street.

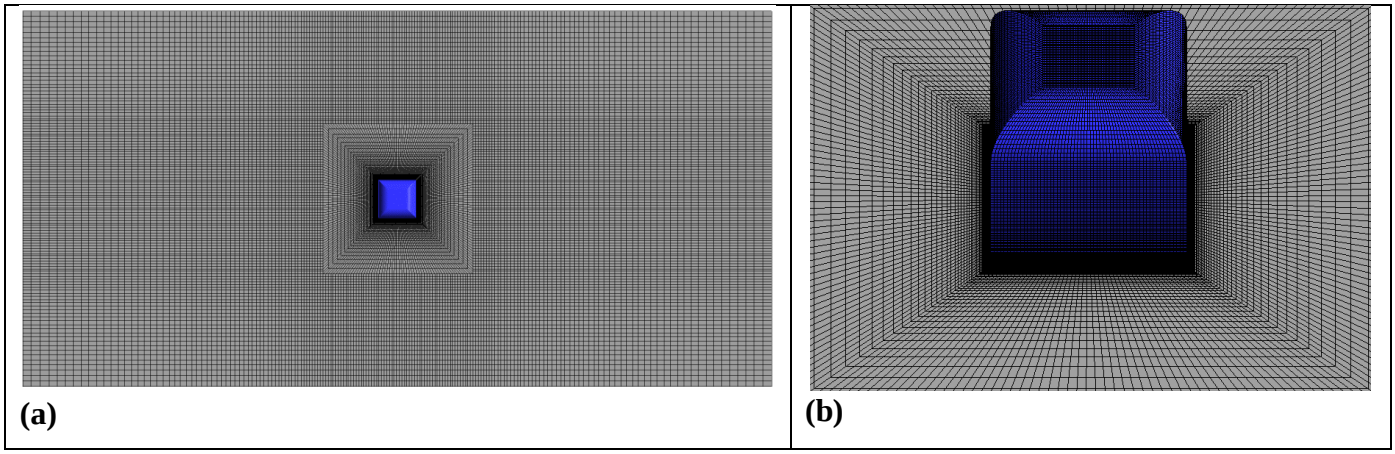

Figure III-2: Mesh topology: (a) Computational grid of the domain, (b) grid near the cube.

Four meshes with different grids sizes are handled to check the solution independency from the grid quality and cell size. Simulations have been performed for the regular cube. The details of these grids, which all have a hexahedral structure, are settled in Table III.2.

Table III-2: Grid independence tests

Grid	Cell size	y+ average	Mean Nusselt number
Grid A	3 489 340	4.15	29.4
Grid B	4 685 356	2.25	28,3
Grid C	**6 105 948**	**0.04**	**27,91**
Grid D	7 025 568	0.039	27,82

It is noted that the mean Nusselt number depends on the grid size for the cases A, B and C. However, the y^+ and average Nusselt number remain almost constant with increasing grid size from grid C to grid D without significant change occurring.

In order to capture the laminar and transitional boundary layers correctly, the grid C is used in this study. The distance from the closest mesh node to the cube was set at 0.00066 h with a growth ratio of 1.05 and 0.0066 h to the channel walls with a growth ratio of 1.1. This refinement near the walls has provided a maximum value of y^+=0.19 for the cube and y^+= 0.78 for the walls as shown in Fig. III-3. Here $y^+ = u_t y / \nu$ is the non-dimensional cell distance from wall; u_t is the friction velocity;

y is the distance to the nearest wall measured in the normal direction; ν is the kinematic viscosity of the fluid [82]. The computations for all cases were conducted with a mesh size of 6 105 948 nodes.

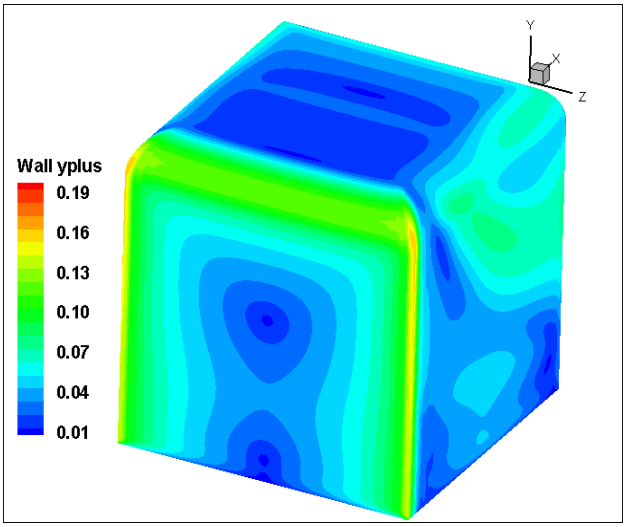

Figure III-3: y+ values at one cell above the surface of cube.

III.5 Computational results and discussion

Three-dimensional, steady simulations have been performed for four cube geometries using the Shear Stress Transport K-ω turbulence model. This turbulence model provides accurate results both at near wall and in the free stream and has been adopted in solving many numerical simulations of jet impingement problems [83]. computations were carried out using the ANSYS™-Fluent package to solve the governing equations of continuity, momentum and energy equations. The coupling between the continuity and momentum equations are done through the SIMPLEC algorithm and second-order upwind scheme has been used to interpolate the face values of the different quantities from the cell-averaged values for convection terms. For the viscous flux terms, a second-order central scheme was considered. To evaluate the face values of pressure terms, the PRESTO (PREssure STaggering Option) method is applied. The main objective of this study is to simulate the mean flow from Massip et al (2012) [29] for the regular cube to assess the methodology. After model validation, both dynamic and thermal behaviour are inspected for the nine studied cases.

III.5.1 Validation of the Numerical Simulation

To validate the present numerical model, the computational results are compared with experimental data of Massip et al. [29] at $Re_H = 3410$ and $\alpha = 0.5$ for the base case (Cube A). Six locations are chosen to assess the implemented model, viz., x/h = -0.75, -0.25, 0, 0.5, 0.75, and 1. Fig. III-4 highlights stations where our numerical results are compared with experimental data.

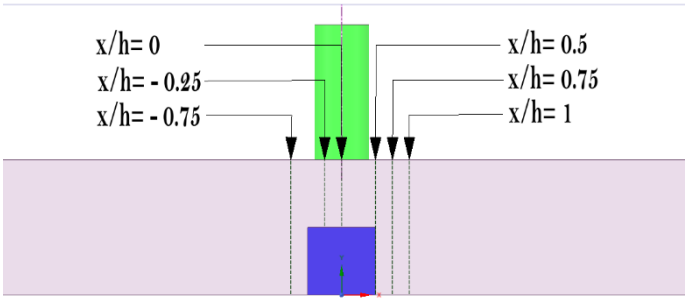

Figure III-4: Stations location where comparisons with experimental data are made.

Fig. III-5 demonstrates the Streamwise dimensionless velocity profiles (u / U_j) for the computed numerical results and experimental data at selected axial location. Globally, it is observed that the computed dimensionless streamwise velocity profiles are in good agreement with the experimental data in almost all locations. We should note that the velocity becomes negative indicating the existence of a reverse flow as can be seen in Fig. III-7. For the first station, x/h=-0.75, which is located upstream of the cube, the flow accelerates in the top half of the channel due to the blockage effect of the component placed in the bottom half. A maximum value is recorded at y/h=1.5. However, when looking at the second, third and fourth stations, the streamwise velocity increases to reach its maximum value at y/h=1.2 and with approaching to the nozzle jet, the flow is decelerated due to the interaction between the two streams. In the wake zone of the component, the flow accelerates in the middle part of the channel with maximum values reported at y/h=1. It can be seen that the correct trend is reproduced by the SST K-ω model but with small differences for the first station. For the other stations, the computed results are in better agreements with experimental data. Through these results, we can conclude that the model, grid and parameters adopted herein have been validated and the implemented model can be used to assess the effect of different cube geometries on the flow field features and the heat transfer efficiency.

III.5.2 Dynamic behaviour

The study of the dynamic behavior of the flow past the four component geometries and the different Reynolds number ratios is essential to well understand the effect of coherent structures on the heat transfer efficiency. Streamlines, turbulent quantities and flow features have to be identified to make a reliable correlation between the dynamic and the thermal behaviors.

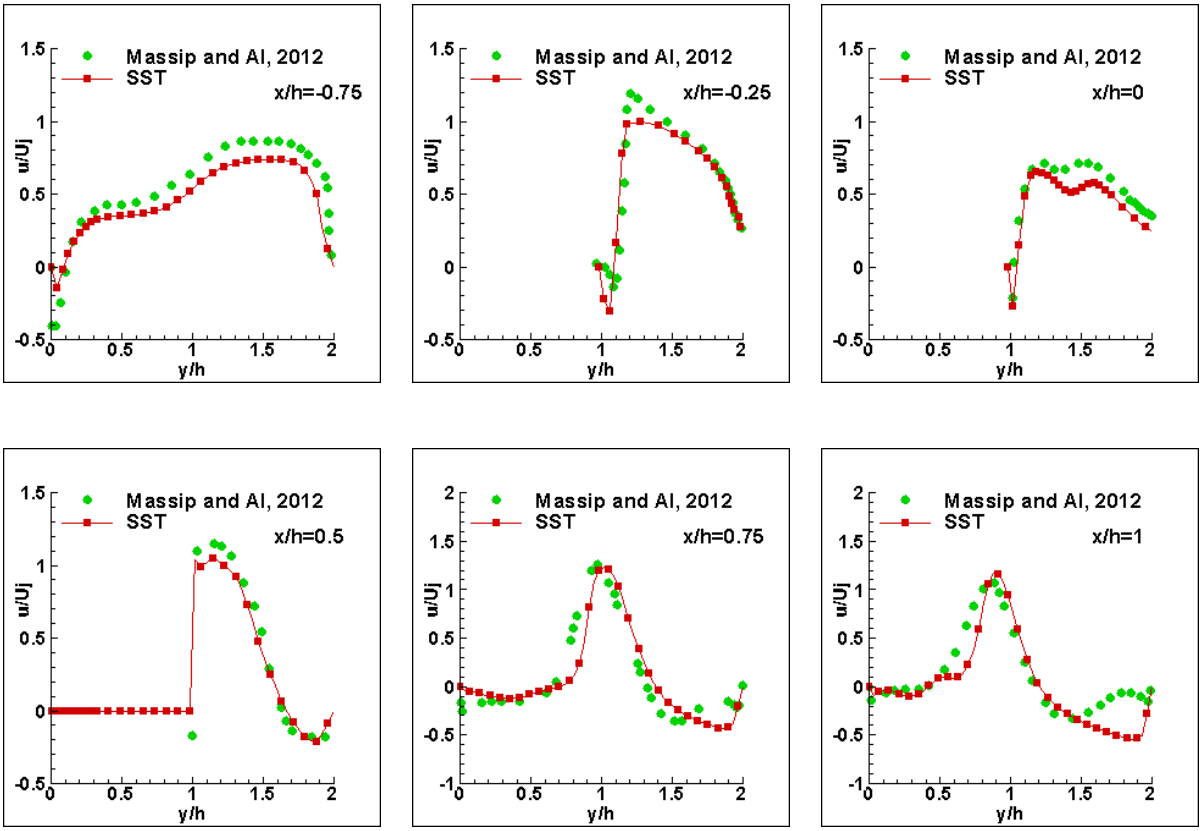

Figure III-5: Streamwise dimensionless velocity profiles compared with experimental data at selected axial locations and z=0.

Massip et Al. [29] highlights and describes the morphology of the flow around a cube subjected to a cross flow and an impinging jet. The different coherent structures that can be identified around the component in the Upper, Frontal, Wake and Side zones are elucidated in Fig. III-6. An upper horseshoe vortex (1) can be established in the upper region which is induced by the interaction between the channel flow and the impinging jet flowing outward radially from the stream impinging point (2). In the near-wake area, a reverse flow forms and expands to the reattachment point position (4), which results in the presence of an arc-shaped vortex (5). In the vicinity of the two lateral faces of the cube and due to the interaction between the channel flow and the lateral faces, side vortices (6) have been created. The blockage effect of the obstacle makes the flow separate and trail off along the obstacle, forming a lower horseshoe vortex (3).

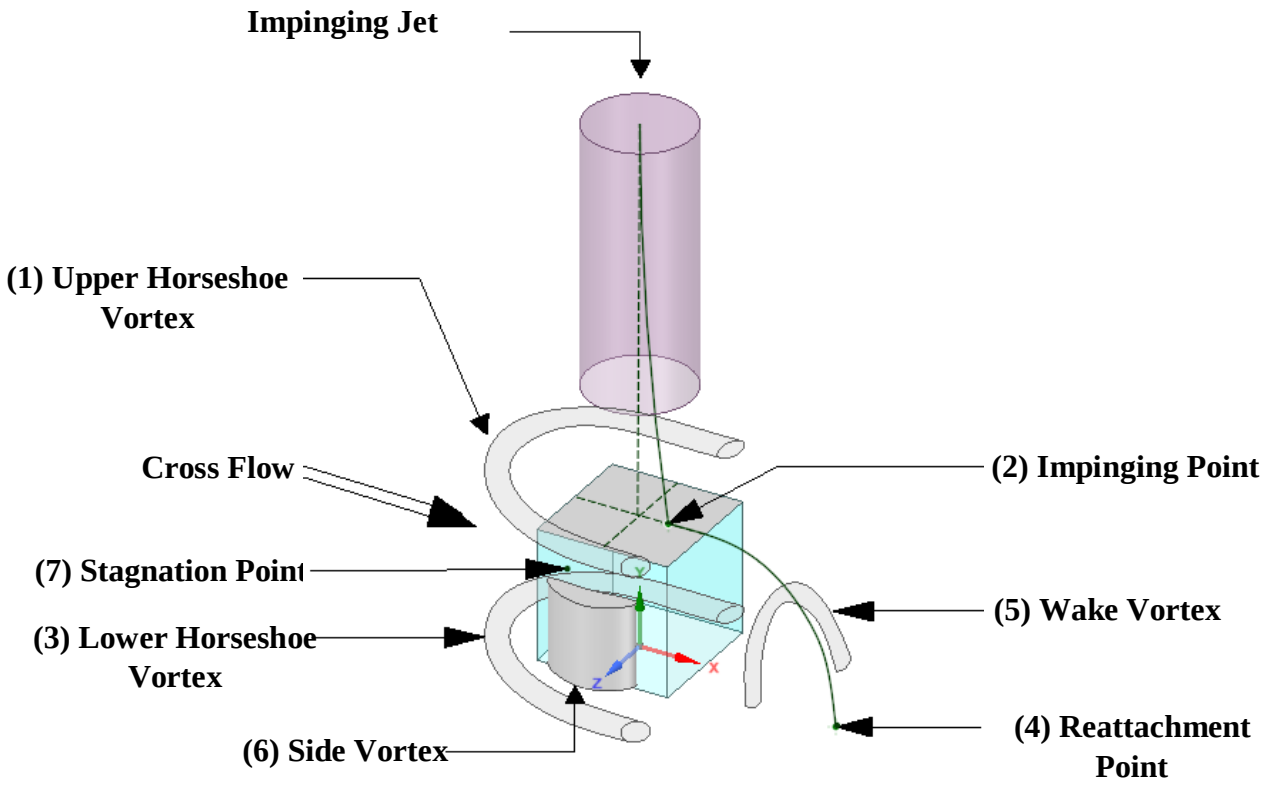

Figure III-6: Schematic representation of the flow features in a surface-mounted obstacle.

Fig. III-7 presents the streamlines contours for the three Reynolds number ratios and the four cubic geometries on x-y plane at z=0 colored by velocity magnitude. It demonstrates that different flow fields are developed depending on the cube geometry and the value of the ratio $\mathrm{Re}_j / \mathrm{Re}_H$. As the cross flow impacted the upper part of the component's front face, there was a stagnation point (see Fig. III-5) that appears on the front face and its position is at approximately y/h = 0.7 for all cases.

When $\alpha = 0.5$, the impinging jet did not reach the top face of the cube since it is dragged by the cross flow and deviated into the downstream direction. A development of four principal vortices is observed in this case. Downstream the rear face of the component, the shear layer separates and subsequently reattaches to the bottom channel wall producing a recirculation bubble just behind the component. Because of the separation of the flow, a bound vortex is formed in the vicinity of the leading edge of the cube A. With the increase in curved radius, this vortex gets smaller until disappears completely the last cube (Cube D). Due to the interaction between the channel flow and the jet flow, an upper vortex is created far away from the cube. Similar recirculation zone is developed for all cubes in the lower part before components.

As the impinging jet flow is boosted to a ratio of unity with the oncoming flow ($\alpha = 1$), an impingement zone appears in the upper area and it is produced by the impact of the jet on the top face of the component. The separation of the flow results in the formation of a recirculation zone in the wake region. It can be seen that with the increase of the rounded edge radius, the reattachment length of the flow to the bottom wall downstream the rear face decreases. Consequently, the size of the recirculation bubble is decreased and the impinging jet is swept closely to the rear face. Compared with the lowest ratio ($\alpha = 0.5$), the size of the bound vortex increases and this vortex shrinks with the increase of the curvature radius. Upstream of the front face, and since the impinging jet does not reach this area, vortices similar to those observed for the first case ($\alpha = 0.5$) develop.

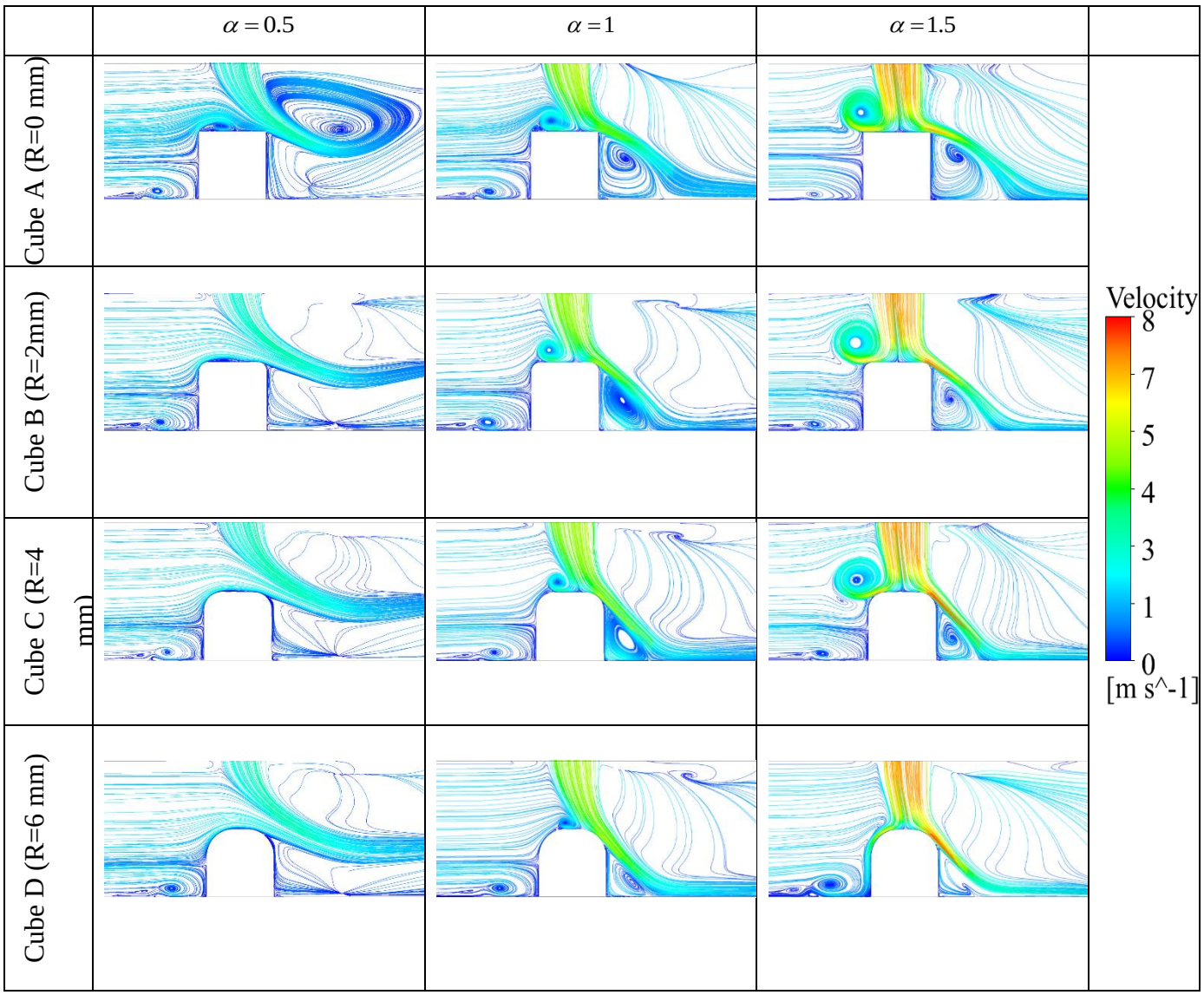

Figure III-7: Streamlines colored by velocity magnitude in x-y plane at z=0 .

For $\alpha = 1.5$, the same vortices observed in the previous cases are developed with bigger sizes. The location of the impinging point (Fig III.5 (2)) from the center of the cube is found to be lower than for $\mathrm{Re}_j / \mathrm{Re}_H = 1$. Furthermore, the use of rounded edges leads to more jet flow sweeping the rear face and even the front face as the case for the cube D which is helpful for cooling efficiency.

Fig. III-8 depicts the pressure contours at the bottom wall of the channel and the cube walls. It is noticed that increasing the jet-to-channel Reynolds number ratio increases slightly the pressure upstream the component that leads to a higher pressure drop in the channel. High pressure zones are observed from the impinging point to the leading edge of the component on the top face as can be seen also on the front face in the vicinity to the stagnation point. Due to the flow separation, a negative pressure region is produced on the side faces. For $\alpha = 0.5$, the pressure profiles are almost similar for all geometries. An over pressure is observed on the top face of the cube A just behind the bound vortex. For $\alpha = 1 \; and \; 1.5$, it is found that increasing the curved radius reduces depression zones.

The three-dimensional vortical structures for twelve cases using the iso-surface of Q-criterion are demonstrated in Fig. III-9. The iso-surfaces are colored by velocity magnitude. This criterion is introduced by Hunt [84] and it is used to identify vortices. It is defined as follow:

$$Q = \frac{1}{2}\left(\|\Omega\|^2 - \|S\|^2\right) \qquad \text{(III-13)}$$

Where: Ω is the antisymmetric vortex tensor and it is defined as:

$$\Omega = \frac{1}{2}\left(\frac{\partial u_i}{\partial x_j} - \frac{\partial u_j}{\partial x_i}\right) \qquad \text{(III-14)}$$

And S is the symmetric strain rate tensor, defined by:

$$\mathrm{S} = \frac{1}{2}\left(\frac{\partial u_i}{\partial x_j} + \frac{\partial u_j}{\partial x_i}\right) \qquad \text{(III-15)}$$

When the Q>0, that means that the vorticity tensor dominates that of the rate of strain, the vortex exists. The size of Q characterizes the vortex's energy. The plot of the iso-surface of Q demonstrates the developing of four vortices around the cubes. For $\alpha = 0.5$, the effect of rounding the top corner on the flow morphology is found to be negligible. The coherent structures are almost identical the four geometries. However, for other ratios, it appears that higher density of vortices is located near the curved edge cubes compared to the regular cube. For $\alpha >= 1$, an upper horseshoe vortex (UHV, Fig. III-6) is produced due the interaction between the cross flow and the fluid moving radially from the jet. For the lowest ratio ($\alpha = 0.5$), this vortex doesn't develop since the impinging jet was dragged and didn't affect the component. Furthermore, the size of the UHV is growing up with the increase of the Reynolds number ratio and it is found to deviate down with the increase of the curved edge

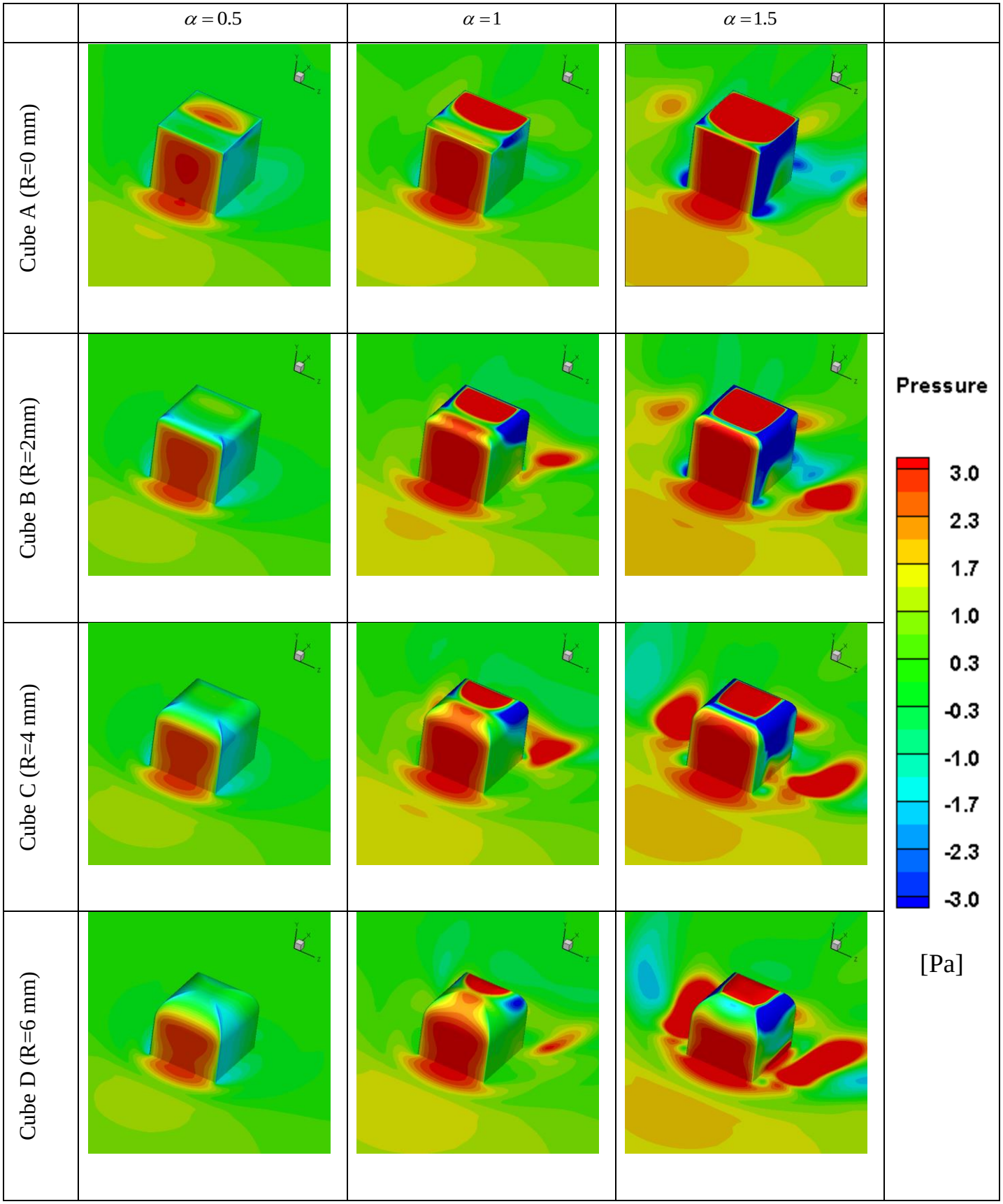

Figure III-8: Pressure profile at the bottom wall of the channel and the cube walls

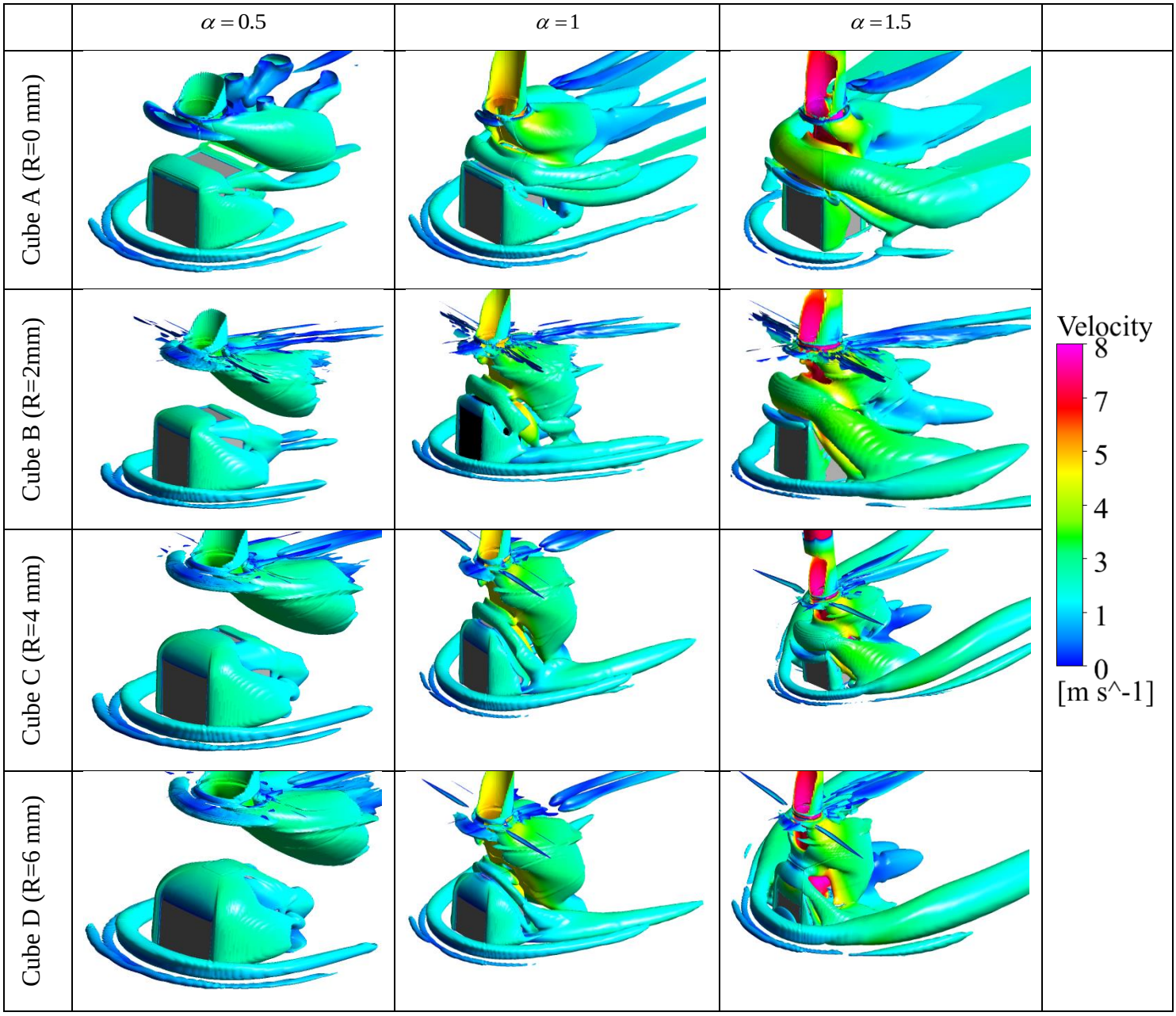

Figure III-9: Three-dimensional vortical structures using the iso-surface of Q-criterion ($Q=10^4\ s^{-2}$) colored by velocity magnitude.

Fig. III-10 shows the turbulence kinetic energy contours around the component in mid-plane z. It is found to be associated with the flow structures and recirculation zones demonstrated in Fig. III-7 and Fig. III-9. It should be noted that the turbulent kinetic energy increases with increasing the jet-to- channel Reynolds number ratio. Furthermore, high turbulent intensity is observed in the wake of the cube and then dissipated gradually in the mainstream flow. The tke contours are quasi similar for the lowest ratio due to the similarity of the flow morphology. However, for $\alpha \geq 1$, increasing the radius of the top corner results in an increase of the turbulent kinetic energy.

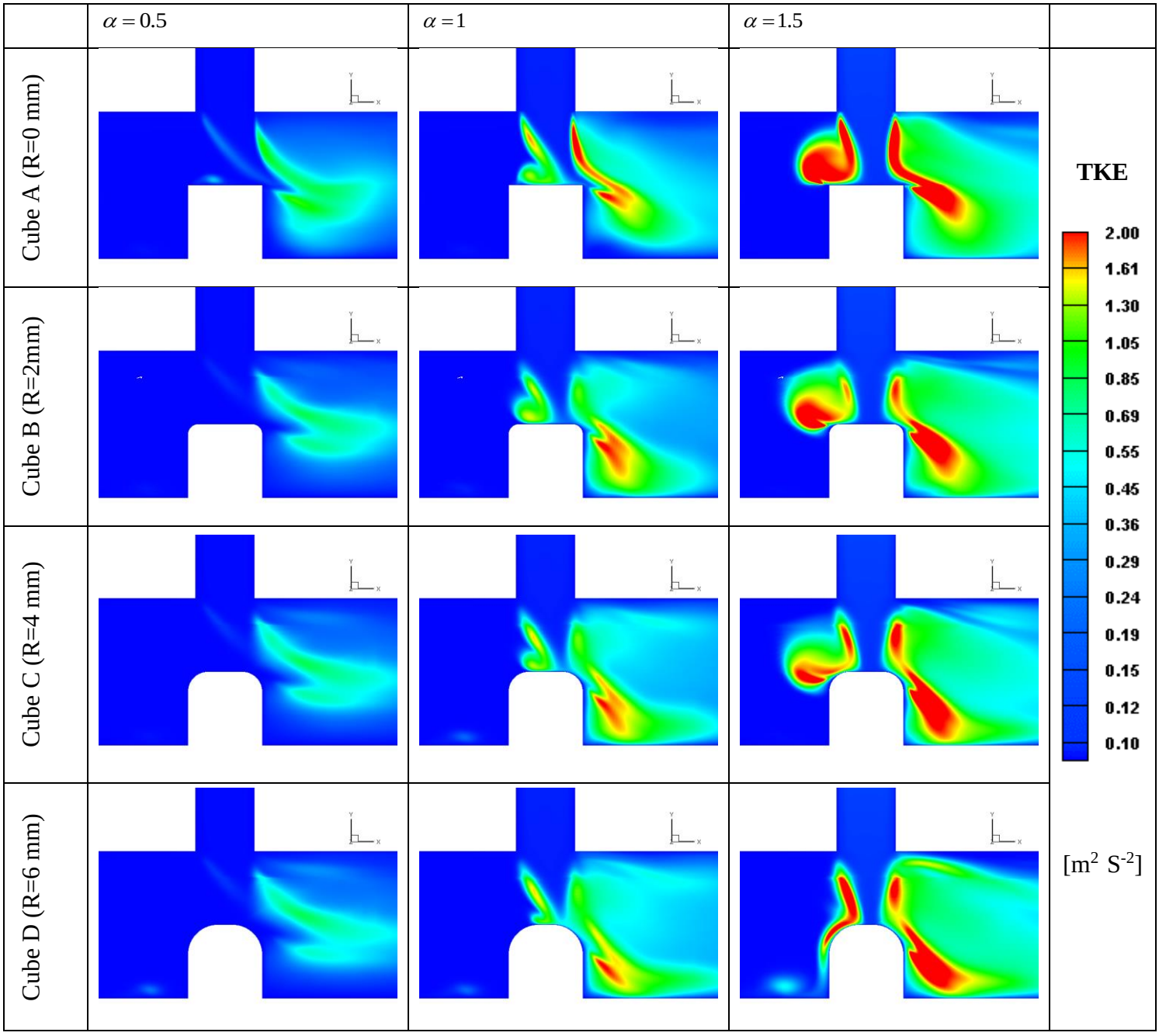

Figure III-10: Turbulent kinetic energy contours around the cube in x-y plane at z=0

III.5.3 Thermal behavior

Fig. III-11 shows the contours of the local Nusselt Number on the cube faces after folded out and projected on the plane. It is important to note that for all geometries, the Nusselt number increases with an increase in the Reynolds number ratio.

For $\alpha = 0.5$, almost the same patterns of Nusselt number are observed in all geometries, and no significant enhancement of the cooling efficiency is gotten by rounding the top edge of the component. This confirms the similarity of coherent structures illustrated in Fig. III-9 since they generally corresponded to the heat flux. Moreover, on the front and top sides, high Nu values are obtained, implying a good transfer of heat in those faces. However, local hot spots are found on the side and rear faces which can cause thermal stress and material damage to the electronic components. It is observed that use of rounded edges enhances heat flux on the rear face. The high density of coherent structures behind curved edge cubes can explain this increase on the cooling efficiency. However, there is a substantial decline on the top face. for the top face, we have demonstrated in the previous section (Fig. III-9) that the bound vortex is shrinking when the radius is increased, until it disappears completely for the R=6 mm that explains the decrease of heat flux in this area.

As the jet impinging Reynolds number equalized with those of the channel ($\alpha = 1$), the cooling performance is increased, in particular on the top and rear faces of the four cubes. With rising the radius of curved edge, the cooling performance for the front face is found to be improved. In addition, a clear enhancement of the heat flux is noticed for $R = 2\,mm$ (Cube B) on the top, side and rear faces compared to the regular cube (Cube A). In this case, the production of the upper horseshoe vortex has carried out a large amount of heat from the top of the component. As the curved edge radius increases from 2 to 4 and 6 mm, a drop in the Nusselt number is associated on the top, side and rear faces. Thus, we can conclude that cube B is the best in terms of cooling efficiency in this case. We should recall that for cube A and B, the local hot spots identified in the previous Reynolds number ratio are removed from the rear face, and it gets smaller for the side face.

In the case of the highest Reynolds number ratio ($\alpha = 1.5$), the Nusselt number levels are higher than in prior cases ($\alpha = 0.5$ and $\alpha = 1$) and consequently the heat transfer is enhanced in all cube faces. In addition, as the curved radius increases, the amount of wall heat flux transferred over-face is increased. This heat flux improvement is a result of the changing in the flow morphology induced by the rounded top corners, in which a good sweeping of the impinging jet flow to the rear and front face is obtained. Moreover, for cubes with rounded edges, the moving down of the UHV to be closer to the rear face carries a large amount of heat. Downstream the rear face, the reduction in recirculation zone sizes with the increasing of the radius assisted in the cooling improvement, due to the fact that

the hot fluid stays trapped in that region which acts as an insulation layer preventing the removal of heat from the surface of the cubes. It is important to point out that an almost homogeneous cooling is achieved for the cube D (R=6mm), and the top face that is exposed directly to the impinging jet flow is with the greatest heat flux. Through these findings, it can be argued that there is a relationship between the flow features and the heat transfer efficiency.

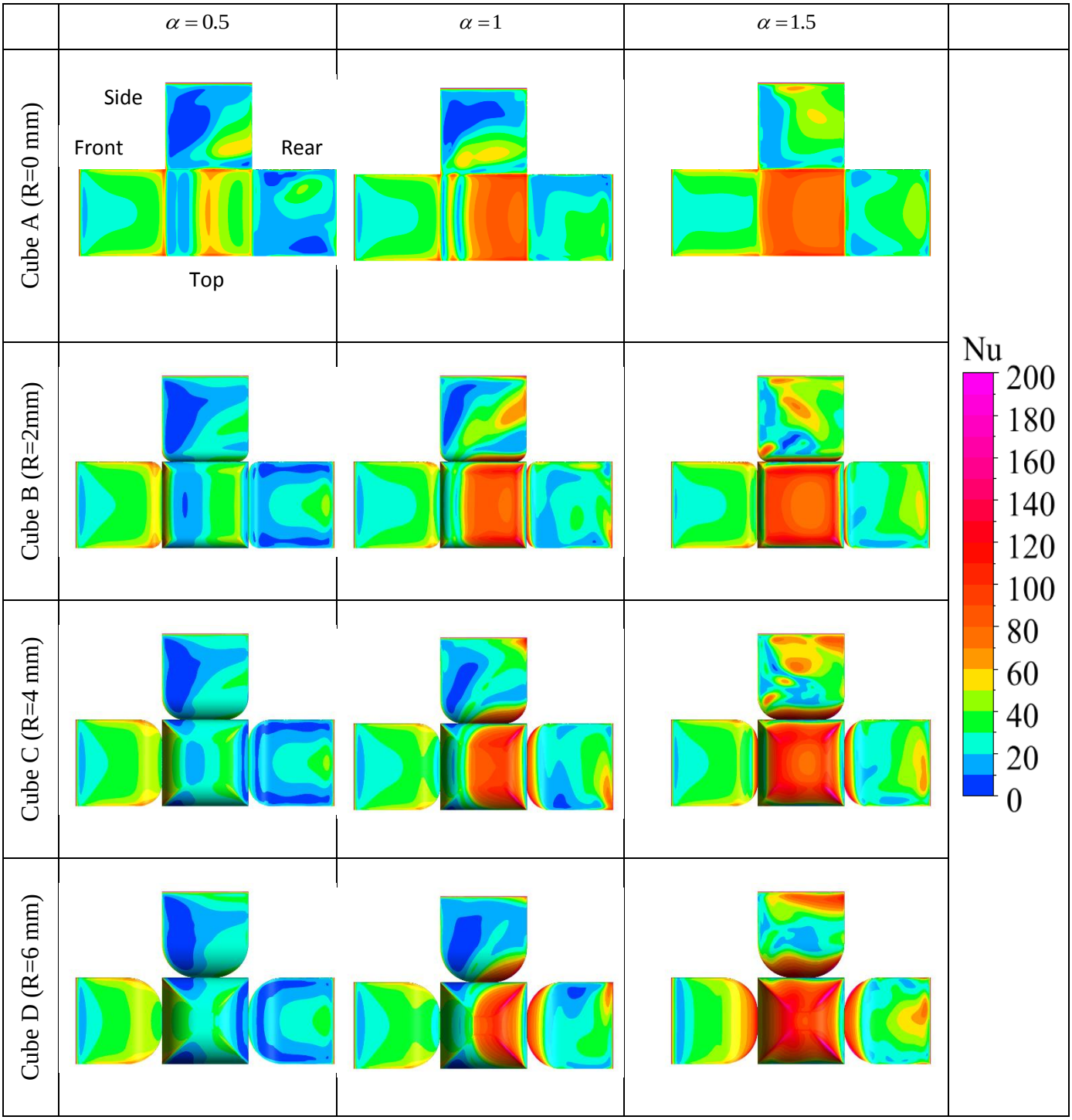

Figure III-11: Contours of local Nusselt number on cube faces for the four cube geometries

Fig. III-12 depicts the temperature distribution in x-y plane at midplane (Z=0). It is noticeable that the thermal boundary layer thickness reduces for all components' configurations when impinging to cross flow Reynolds number ratio is increased. For $\alpha = 0.5$, as expected by previous results, temperature contour levels seem to be similar near the cube since the flow morphology does not change considerably for the modified geometries. A little improvement of the cooling process is achieved for the cube B when the ratio is increased to reach unity. Low temperature levels are observed indicating better heat flux compared to others. For the highest Reynolds number ratio, the exchanged heat flux is enhanced on the front and rear faces of the heated cube D (R=6mm) in counter to the base element (cube A) where there is a poor heat transfer. Through these findings, it is important to note that there is a direct relationship between the temperature profile and flow features developed near cubes demonstrated in Fig. III-7 and Fig. III-9.

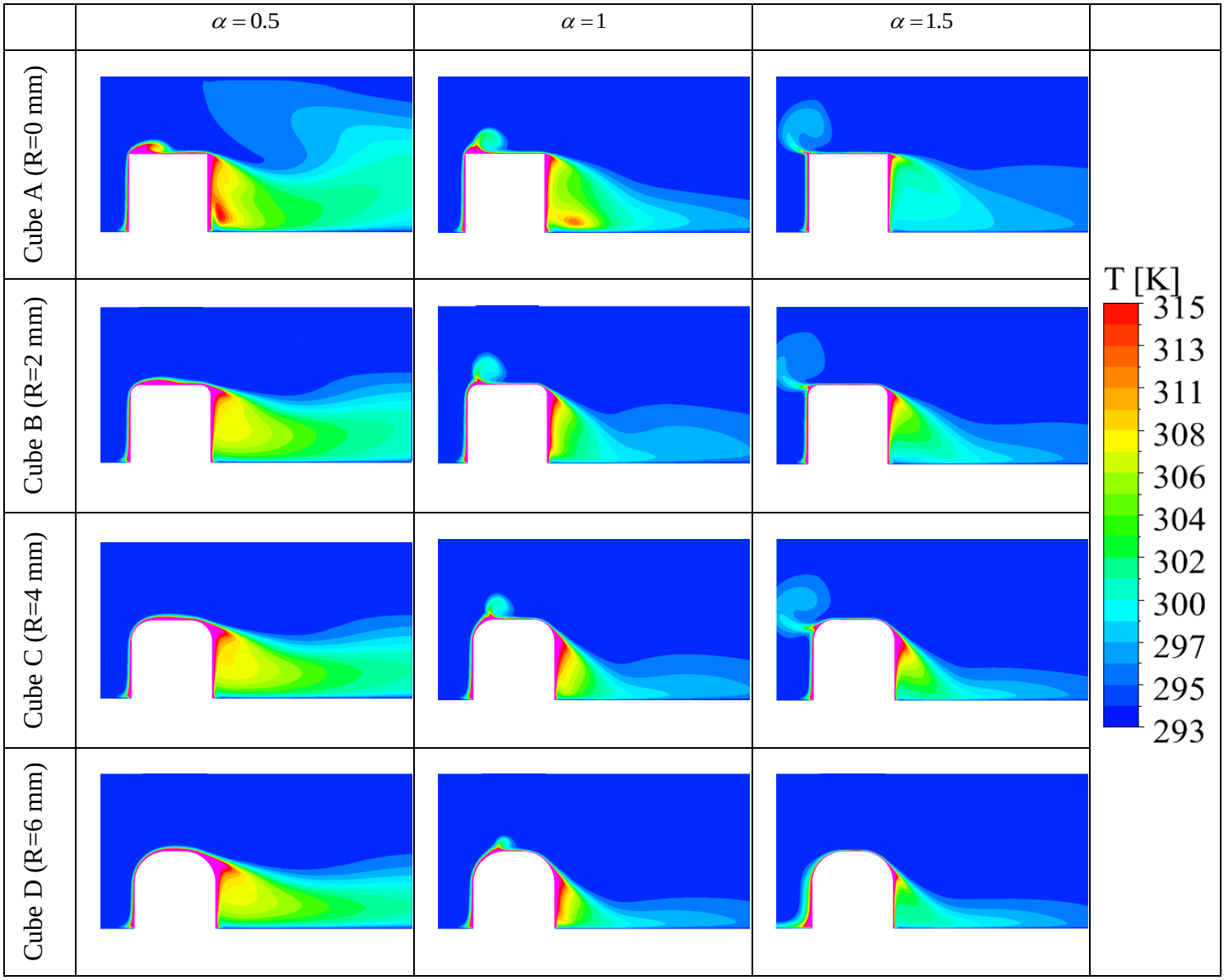

Figure III-12: Temperature contours in x-y plane at z=0

The wall heat flux at the surface of the cube is demonstrated in Fig. III-13 in a front view. It is clear that the exchanged heat flux is improved with the increasing of the jet-to- channel Reynolds number ratio. Maximum heat flux is achieved on the top face since this later is directly subjected to the cold impingement jet. Moreover, a little decrease of the heat flux can be observed around the impingement point. For $\alpha = 0.5$, no improvement of the cooling efficiency is gotten by rounding the

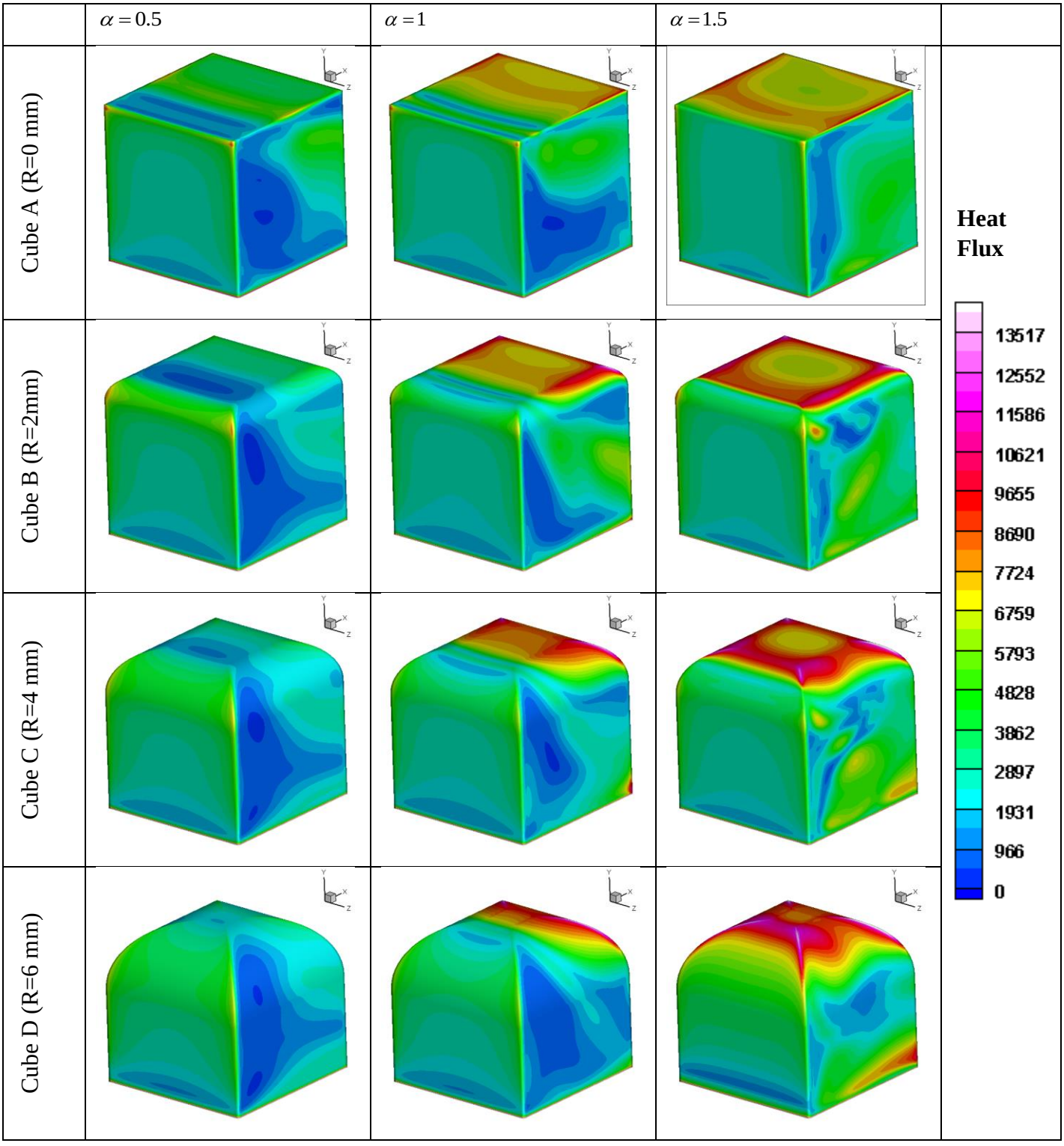

Figure III-13: Heat flux contours on the surface of the component, front view

top corners. When the ratio is boosted to unity, the cooling efficiency is improved for the top face, however for the side face, no significant improvement is shown. For $\alpha = 1.5$, and since the jet sweeps all the faces of the cube D as can be seen in Fig. III-7, a remarkable enhancement is achieved associated with an almost homogeneous cooling.

The distribution of the Nusselt number along the pathline ABCD, highlighted in Fig. III-14, is presented in Fig. III-15. The Nusselt number profile is almost similar Along the line [AB] located in the front face, with a slight convective heat transfer improvement is observed in the upper part of the face for the rounded edge cubes. For $\alpha = 1.5$, there is an enhancement in the cooling efficiency resulting from the sweeping of cold air on the front face as indicated in Fig. III-7. For the top face (line [BC]), a meaningful enhancement is achieved when the $\mathrm{Re}_j / \mathrm{Re}_H >= 1$ for all cubes geometries which can be explained by the impact of cold air jet on the component and the production of the UHV that carries a huge amount of heat. Additionally, the rounding of the cube edges results in more heat flux transferred along the latter line for the highest ratio. The Nusselt number trend along the line [CD] is similar for all ratios. For $\alpha = 1.5$, a maximum heat convection is observed for cube D due the sweeping of cold jet fluid along the rear face. When $\alpha = 0.5$, a little improvement is shown for the modified geometries in the lower part of this face.

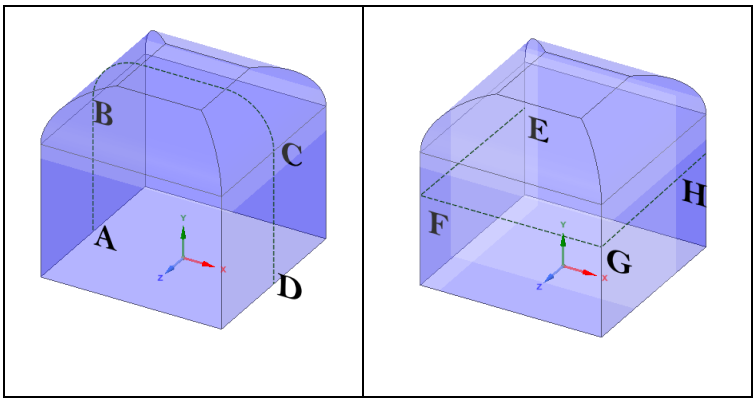

Figure III-14: Position of the values of Nusselt number for various lines.

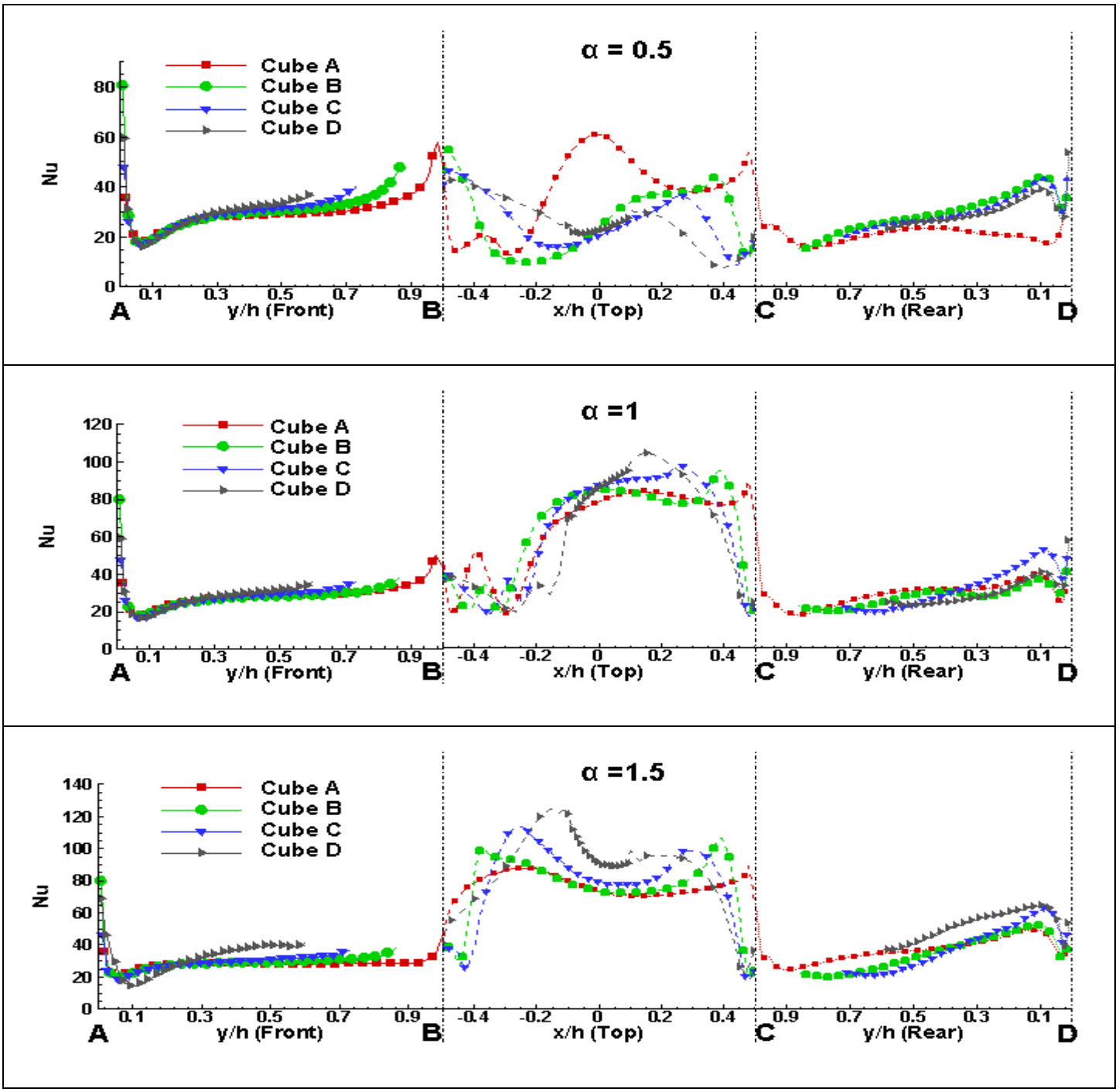

Figure III-15: Profiles of the Nusselt number along the pathline ABCD.

Fig. III-16 demonstrates the evolution of the Nusselt number along the pathline EFGH showed in Fig. III-14. The Nusselt number profile across the line [EF] for the different R radii has the same tendency for the front face. As can be seen, the heat transfer rate increases near the edges and decreases in the center. The minimum heat transfer is observed near the stagnation point. For $\alpha = 0.5$ and $\alpha = 1$, the increasing of the curved edge radius R gives rise to a little enhancement of the

cooling effectiveness. However, For the cube D, a significant improvement is achieved for the highest ratio $\alpha = 1.5$ due to the sweeping of the cold jet fluid along the front face (see Fig. III-7). For the other cases, the jet did not reach this face. For the side face, the rounding edges did not improve the cooling effectiveness for $\alpha = 0.5$, the Nusselt number profiles overlapped in the range of $-0.1 > x/h > -0.5$ and decreases for $x/h > -0.1$ with the increasing of R. A better improvement of this face is achieved

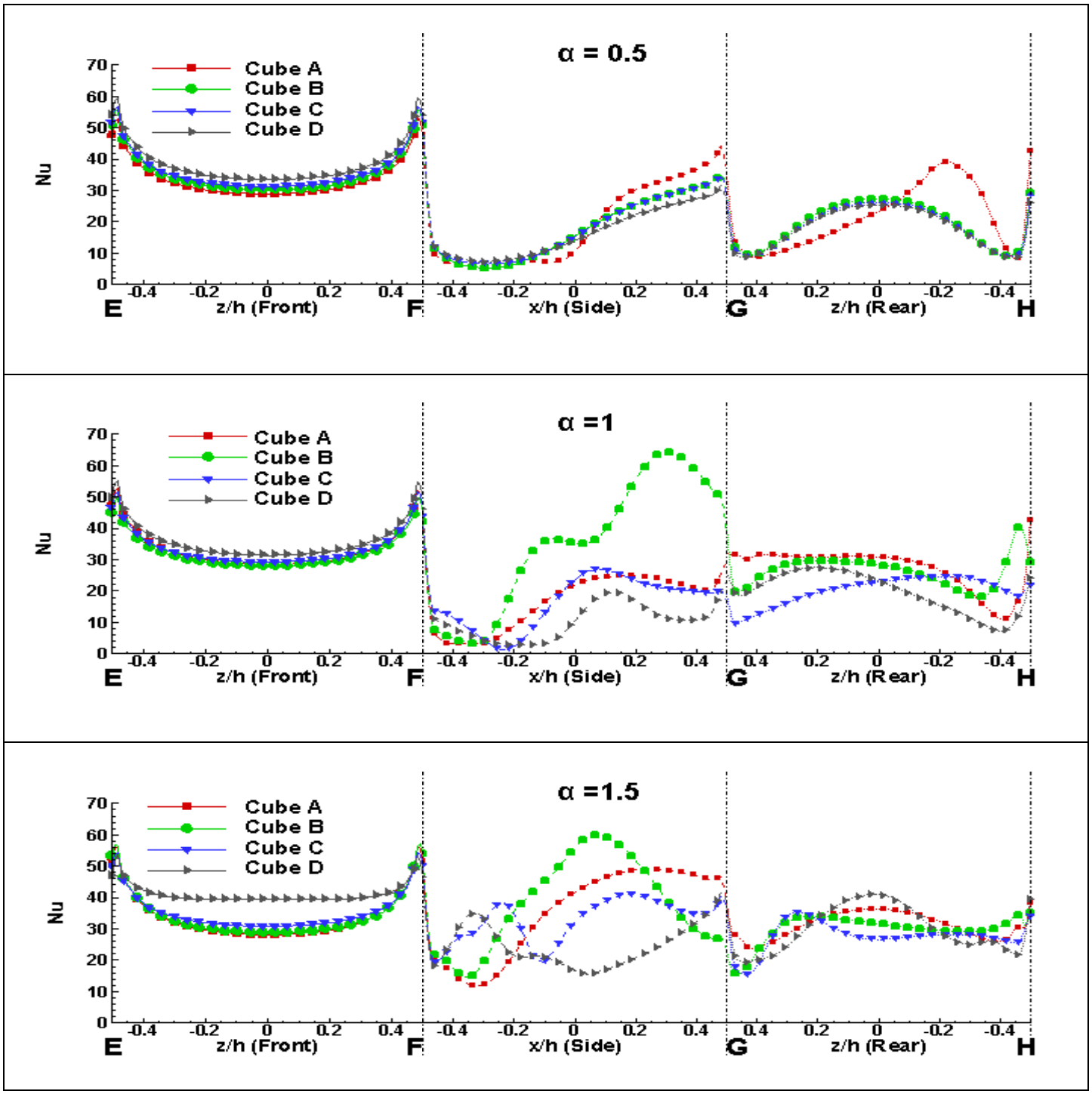

Figure III-16: Profiles of the Nusselt number along the pathline EFGH.

for the Cube B $(R = 2mm)$ and $\alpha = 1$. For the highest ratio, the exchanged heat flux is enhanced for the cube B especially in the middle part of the face. Along the line [GH] which corresponds to the rear face, the heat transfer is increased in the center part and no significant improvement is obtained for the rounded edges cubes across this line. For the lowest Reynolds number ratio $(\alpha = 0.5)$, it is important to note that the front face is the best cooled compared to other faces due to the fact that the jet did not reach the component. However, for higher Reynolds number ratios, it is the top face that has a maximum heat flux exchanged.

Fig. III-17 illustrates the average Nusselt number on the cube surface. It is clear that the increase of the impinging jet Reynolds number significantly improves the cooling efficiency. The global Nusselt number increases as the Reynolds number ratio increases. For $\alpha = 0.5$, the regular cube (cube A) is the best cooled component with a value of Nu=28. The cooling efficiency is decreased for the cubes with a rounded top edge. For a ratio of unity, a little improvement of the exchanged heat flux is achieved in cube B with an average Nu=39 and increasing the radius from 2 mm to 4 and 6 mm leads in a reduction of the heat transfer efficiency. Using a cube with a radius to height ratio of 2/15 would increase the cooling performance by over 6%. For $\alpha = 1.5$, as the radius of curved edges increases, the average Nusselt number increases to reach a maximum value of 53 in the case of cube D (R= 6mm) with an enhancement of more than 23% compared to the base case (cube A).

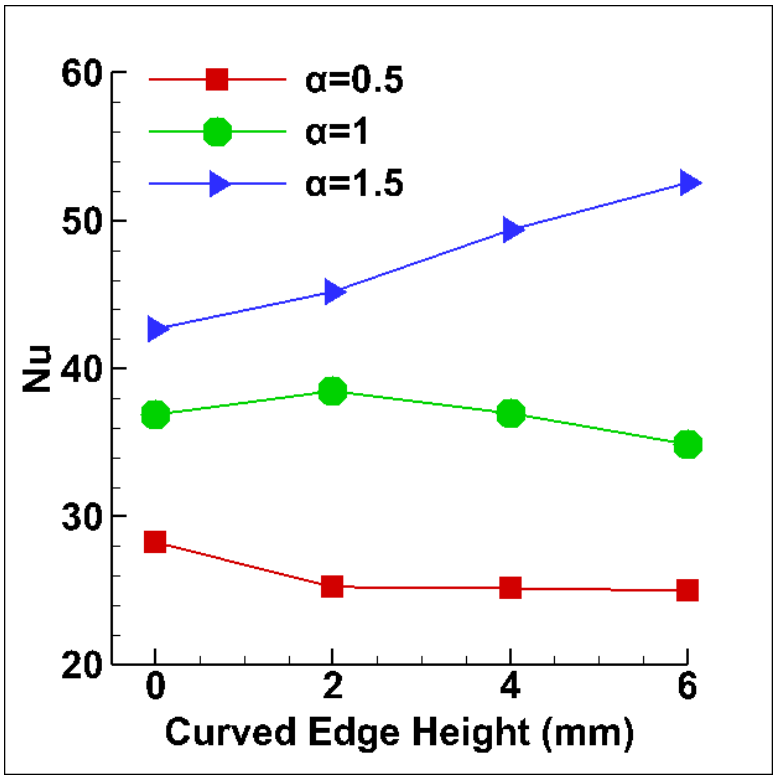

Figure III-17: Average Nusselt number on the global surface of the cube versus curved edge height.

III.6 Conclusion

The study of the flow past a wall heated mounted cube placed in the middle channel is the subject of this chapter in which both the dynamic and thermal aspects are studied numerically. Simulations are performed at a Reynolds number of 3410 for the channel flow and three different impinging-to-cross-flow Reynolds number ratios ($\alpha = 0.5,\ 1\ and\ 1.5$). The study is handled using the Shear Stress Transport K-ω turbulence model. The assessment of the implemented methodology is validated against the experimental data of Massip et Al. [29]. Comparisons were made for the streamwise mean velocity and it should be emphasized that the obtained numerical results are in well agreement with available data. Once the methodology is validated, we have investigated the impact of rounding the top corners of electronic component on the cooling process. In addition to the regular cube, three more modified cubes were examined based on the radius of the rounded top corner. Different flow features have been identified in the vicinity of the component such as flow separation, vortices and recirculation zones. The main finding is that there is a direct relationship between the flow morphology and the cooling efficiency. The impact of the Reynolds number ratio is analyzed and is found to be of a great influence on the cooling efficiency. As the ratio increases from 0.5 to 1 and 1.5, the amount of heat transfer is increased. For the lowest impinging jet Reynolds number and due to the fact that the impinging jet is dragged away from the component by the channel flow, no improvement of the exchanged heat flux is achieved by rounding the top corners of the cube. The Nusselt number is decreased with the increasing of the curved radius. With a ratio of unity, the impinging jet impacts the top face of the components and enhances the cooling process. For this case, the analysis reveals that with rounding the top corners of the cube by a radius of 2 mm (cube B), the cooling efficiency can be improved by more than 6%. Furthermore, the cooling effectiveness is enhanced for all rounded cubes for the highest ratio ($\alpha = 1.5$). It can be enhanced by more than 23% by rounding the top corners of the components with a radius of 6 mm (cube D).

CHAPTER IV: FLOW PAST AN ARRAY OF STAGGERED OBSTACLES

IV.1 Introduction

The cross-flow past an array of obstacles has received considerable attention and has been investigated extensively both experimentally and numerically due to its presence and importance in many fields. In such types of flow, several complicated phenomena are presented. In this chapter, the flow past two different tube bundle geometries was performed using the large eddy simulation method based on the WALE model. The obtained results were compared with experimental data and those obtained by Patel [95] using SST method. Time averaged and normalized results of streamwise velocity components, velocity vector fields, vorticity contours, and turbulent quantities have been obtained and compared for both arrangements.

IV.2 Problem setting and boundary conditions

Fig. IV-1 depicts the computational domain that consists of a system of staggered obstacles (cylinders' system) placed in a square channel. Flow past two different configurations is investigated; the first system includes cylinders all of circular shape, while the second configuration comprises a combination of intercalated circular and square cylinders. The bundle comprises six cylinders' rows (circular and square) arranged in staggered configuration with square cylinders having a side of 8.86 mm and circular cylinders having an outer diameter of 10 mm. The transverse and longitudinal pitch to diameter ratios, S_T and S_L, are 3.6 and 4.2, respectively. The length to diameter ratio of the rods is 7.2. Each row has 1 or 2 full cylinder, as shown in the Fig. IV-1. The same conditions of the experiment of Balabani and Yianneskis [45] have been imposed in our numerical study in the aim to validate the results. The study was carried out at a Reynolds number ($\mathrm{Re}_D = uD/\nu$) of 12,858 based on the gap velocity ($=1.29\ ms^{-1}$), the cylinder diameter, the working fluid being water at $20\,°C$ whose kinematic viscosity is $\mu = 1.003\times10^{-3}\ Pa.s$ and density is $\rho = 998.2\ Kgm^{-3}$. The rods were rigidly mounted on the walls. Using a Doppler Laser Velocimeter technique, the authors measured mean velocities and turbulence levels. As shown in Fig. IV-1, the geometry used in the LES computations is rectangular. The left and right side of the domain are located 4.2D upstream of the first line and downstream of the last row, respectively. They are set as input and output flow boundaries. For these boundaries, a uniform velocity (U_∞ = 0.93 m/s) is imposed at the inlet and a downstream relative pressure condition ($\overline{p} = 0\ Pa$) is applied. Its central zone has a length of $10.5D$. The height of the cylinders is thus the whole height of the tube ($7.2\mathrm{D}$). A stationary no-slip smooth

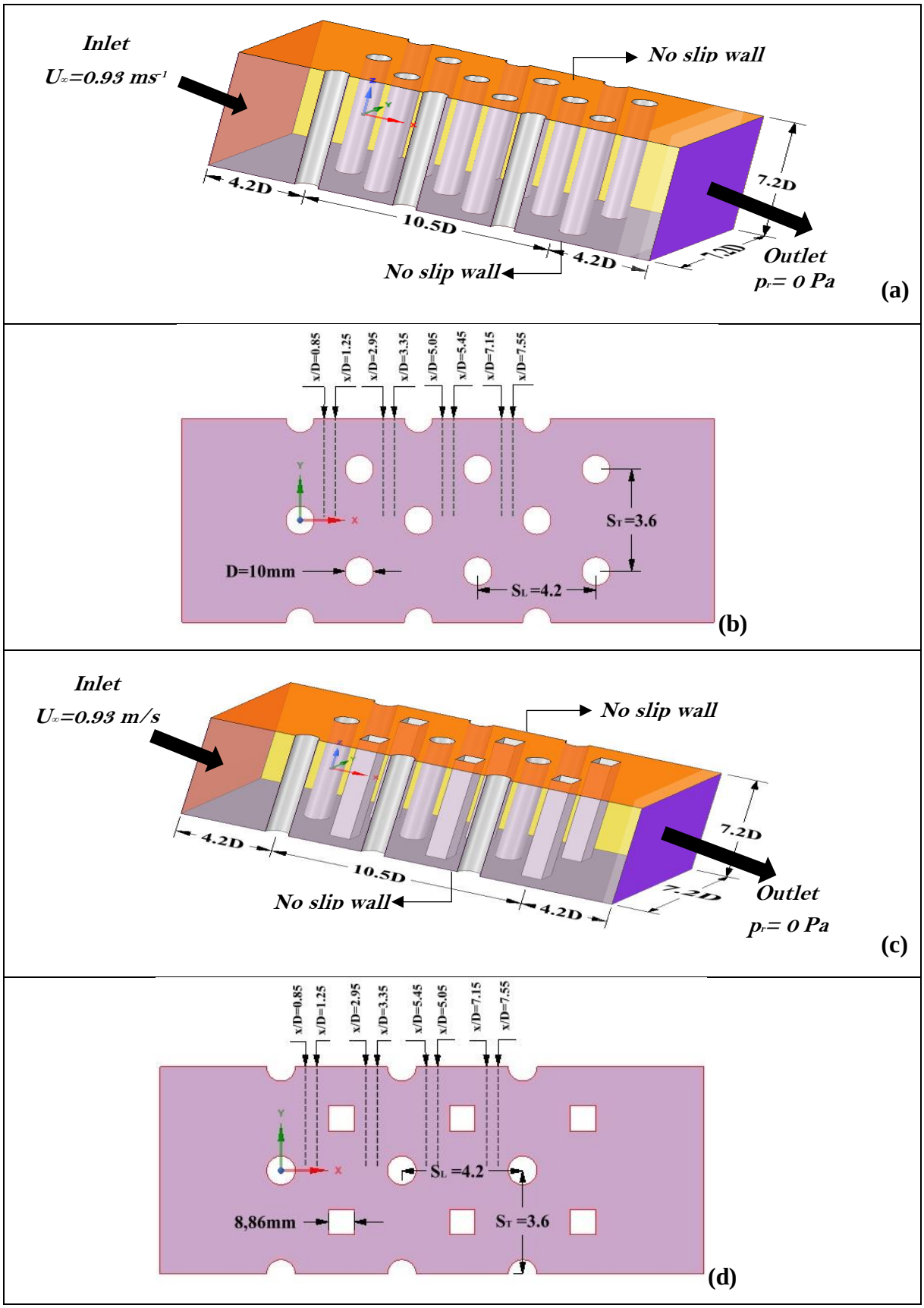

Figure IV-1: Sketch of the computational domain including boundary conditions (not to scale): (a) circular tube bundle, (b) – (d) Cross-sectional views of tubes bundle, and (c) mixed tube bundle.

walls ($\overline{U}=0$) is considered for the top and bottom sides. A square section channel with a total length of 18.9D comprising 6 rows has been considered herein to prevent an excessively wide mesh of computing. It should be noticed that our main objective is to simulate such a bundle flow using the LES technique. To summarize, the sketch shown in Fig. IV-1 illustrates the complete flow simulation area concerned.

IV.3 Mathematic formulation

The flow applied to the problem is three dimensional, incompressible, steady, and turbulent. The fluid is Newtonian and incompressible with constant density ρ and dynamic viscosity μ and without buoyancy effects. A brief summary of the equations for governance is given here. We focus in this study on the dynamic effect, so the governing equations are the Continuity and the momentum equations.

In the LES context, these can be written as follows [50, 85], to name a few:

$$\nabla.\overline{U}=0 \qquad \text{(IV-1)}$$

$$\frac{\partial\overline{U}}{\partial t}+\overline{U}.\nabla\overline{U}=-\nabla\left(\overline{p}/\rho\right)+\nu\nabla^2\overline{U}-\nabla.\tau_{sgs} \qquad \text{(IV-2)}$$

Here $\overline{U}(\overline{u},\overline{v},\overline{w})$ and $\overline{p}$ are the filtered velocity and pressure, respectively, ρ is the fluid density and ν is the fluid's kinematic viscosity, and $\overline{(.)}$ denotes any grid-filtered quantity. The small scales influence in Eq. 2 appears through the sub-grid scale (SGS) stress tensor which can be defined as follows [86, 87]:

$$\tau_{ij}^{sgs}=\overline{u_iu_j}-\overline{u}_i\overline{u}_j \qquad \text{(IV-3)}$$

Such a tensor is split into an isotropic part and anisotropic part. The second (deviatoric part), relevant in incompressible flows and reflecting the interaction between resolved and unresolved scales, is modeled (approximated) according to the Smagorinsky-Lilly closure [86, 88] as follows:

$$\tau_{ij}^{sgs}\simeq-2\nu_t\overline{S}=-2(C_s\Delta)^2\left\|\overline{S}\right\|\overline{S} \qquad \text{(IV-4)}$$

wherein $\Delta=Min\left(\kappa y,C_sV^{1/3}\right)$ is the filter length scale, κ being the Von Karman constant ($=0.42$), C_s is the parameter that may not be universal (i.e. fixed or dependent on the flow), whose value varies

from 0.1 (for shear flows) to 0.2 (for high Reynolds number flows), y is the closest wall distance, V is the computational cell volume,

$$\overline{S} = \left(\nabla\overline{U} + \nabla^T\overline{U}\right)/2 \qquad \text{(IV-5)}$$

and

$$\|S\| = \left(2\overline{S} : \overline{S}\right)^{1/2} \qquad \text{(IV-6)}$$

$\overline{S}$ being the resolved-scale strain rate tensor, $\left\|\overline{S}\right\|$ the Frobenius norm (second invariant) of $\overline{S}$, and ν_t is the sub-grid-scale kinematic turbulent viscosity ($\nu_t = C_k\sqrt{k_{sgs}}$ k_{sgs} being the SGS kinetic energy). The SGS stress tensor's trace is incorporated in the pressure term, thereby modifying the pressure ($\overline{P} = \overline{p} + \tau_{kk}\delta_{ij}/3$).

For more information on the Smagorinski model and/or its dynamic variant (DSGM), the reader can refer to the ample literature in this area, and in particular to Lilly [87]. Unfortunately, such a model incorrectly handles the near-wall region by providing a non-zero turbulent viscosity at the wall. To fix this imperfection, the van Driest's damping approach is often used, so that the turbulence near the wall has a good parietal behavior, i.e. $\nu_t \propto y^{+3}$, $y^+ (= yu_\tau/\nu)$ being the dimensionless wall distance.

The SGS model adopted here to perform this study is the WALE model (Wall Adapting Local Eddy-Viscosity) in which the SGS eddy viscosity is set in terms of invariants such as [85-87]:

$$\nu_t = (C_w\Delta)^2 \frac{(\overline{S}^d : \overline{S}^d)^{3/2}}{(\overline{S} : \overline{S})^{5/2} + (\overline{S}^d : \overline{S}^d)^{5/4}} \qquad \text{(IV-7)}$$

where the traceless symmetric tensor $\overline{S}^d$ reads [84]:

$$S_{ij}^d = (\overline{g}_{ij}^2 + \overline{g}_{ji}^2)/2 - \overline{g}_{kk}^2\delta_{ij}/3 \qquad \text{(IV-8)}$$

with $\overline{g}_{ij} = \partial\overline{u}_i/\partial x_j$, $\overline{g}_{ij}^2 = \overline{g}_{ik}\overline{g}_{kj}$, and δ_{ij} is the the Kronecker tensor *(in terms of components*). Here, the Einstein summation convention applies.

The salient points of the relationship (7) are threefold: 1) ν_t involves the strain and rotation tensors, thereby allowing to pick up turbulent structures relevant for the kinetic energy dissipation, 2) ν_t automatically tends towards zero near the wall with appropriate scaling ($\propto y^{+3}$), and 3) ν_t can be neither negative nor infinite.

It should be recalled that these equations are those of Navier-Stokes, implicitly filtered in space, in which the spatial filter is determined by a filtered computational cell size (Δ). In other words, the process consists in filtering out the small eddies with size smaller than the filter width so that the model can solve only the large scales of the flow field while modeling the small scales.

In our study a value of $C_w = 0.325$ is used, according to the procedure advised by Nicoud and Ducros [85], which is taken up in the literature (see, e.g. Refs. [58, 59, 88]), to name a few. According to Busco and Hassan [89], the WALE model is able to provide a physical insight of secondary flows, and it scales the eddy viscosity appropriately near to walls avoiding any damping function while being is less sensitive to the model coefficient C_w**.** Moreover, it behaves well to handle wall-bounded flows, is less dissipative, and is able to accurately capture the near wall behavior (in thin shear layer). It is worth noting that it is this model which has been used in this study unless otherwise stated.

IV.4 Meshing implementation

It is well known that meshing plays a crucial role in performing precise simulations, especially in LES. In this aim to reduce the computational effort while at the same time maintaining adequate precision, high density grid is implemented in high gradient zones, however a low density is adopted in less interest zones. A structured hexahedral mesh is handled in these simulations and is generated using ANSYS™ ICEM. The hexahedral grids are finer in the near-wall regions of the cylinder and the channel walls and slightly coarse elsewhere as shown in Figs. 2b-d. The distance between the nearest mesh node has been defined such that the maximum value of y^+ is proper (~ 0.87 for the D grid; see Table 2).

Figs. IV-2(a) and (c) display the mesh generation in the computational domain for the two configurations. Figs. IV-2(b) and (d) show the grids around circular and square tubes, respectively. In the vicinity of the cylinder, very fine meshes are needed to well resolve the flow physics in the near-wall regions (boundary layer separation and the shedding process). Note that only a reduced number of grid points are displayed to make the figure readable.

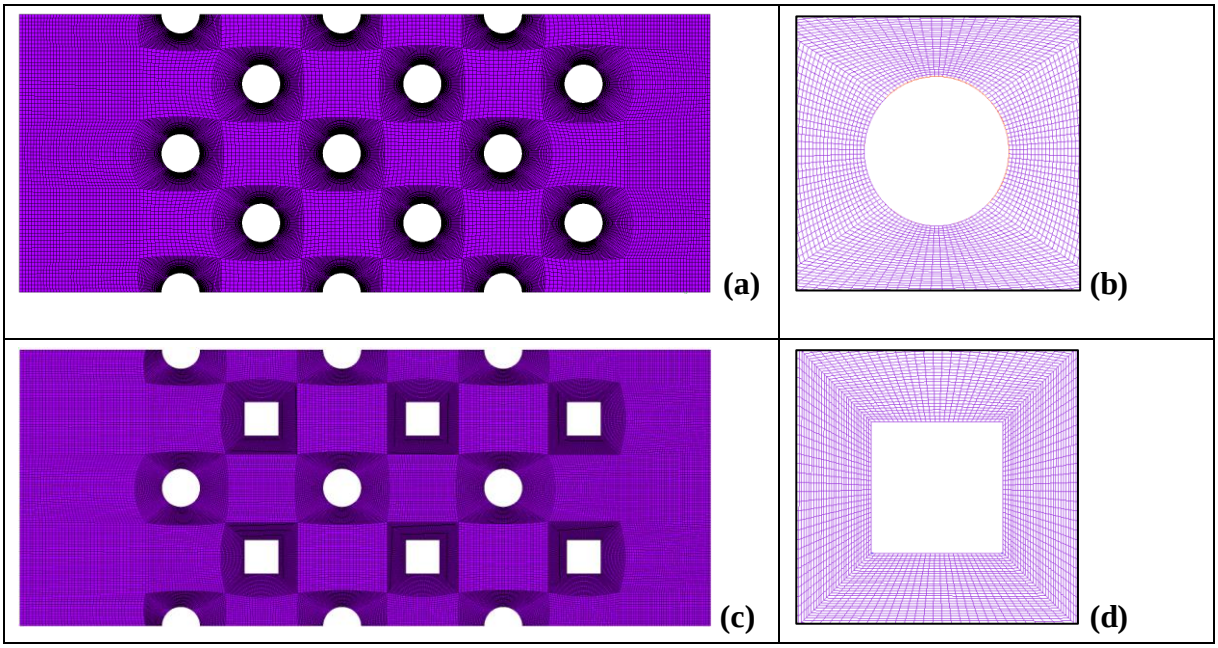

Figure IV-2: Mesh topology: (a) Computational grid of circular tube bundle, (b) Computational domain of mixed tube bundle, (c) grid close-up around the circular tube, (d) grid close-up around the square tube.

IV.5 Computational method and numerical set-up

In the present simulation, the finite volume method is implemented to compute Eqs. (IV.1) - (IV.2) with adequate boundary conditions using the ANSYS™ FLUENT CFD code 18.1 [88]. For momentum discretization, a bounded central differentiation scheme is applied, whereas to advance the equations in time, a second order implicit scheme is employed. To handle the pressure-velocity coupling between momentum and continuity equations, the well-known SIMPLEC algorithm is involved. A convergence criterion of 10^{-5} has been set for the continuity and momentum equations residuals with a time step of $10^{-3}\ s$. To sum up, Table IV.1 gathers further details.

Table IV-1: Simulation settings and boundary conditions (BCs).

Settings parameters	
Simulation type	3D Unsteady
SGS model	Wale model
Pressure-velocity coupling	SIMPLEC
Momentum discretization scheme	Bounded central differencing
Convergence criterion	10^{-5}
Fluid Properties	$\mu = 1.003\times10^{-3}\ Pa.s\ ;\ \rho = 998.2\ Kgm^{-3}$ at $T = 20\ °C$
Cylinder diameter	$D = 10^{-2}\ m$

Re	$Re = 12{,}858$
Time step	$10^{-3}\ s$
Grid used	4859,712 cells
CFD code	Ansys™ Fluent 18.1
BCs	
Inlet	Inlet velocity: $U_\infty = 0.93\ ms^{-1}$
Outlet	Relative pressure: $0\ Pa$
All walls	No-slip wall: $\overline{U} = 0$

The LES method is an expensive approach due to its demanding requests of computational time and accurate mesh generation. Four different sizes of grids are used to verify the independence of the solution from the consistency of the grid and cell size. The details of these grids, which all have a hexahedral structure, are given in Table IV.2. For traditional LES, some of these meshes can appear a bit coarse. It is worth noting, however, that the primary objective here is to evaluate the model capacity considered to manage such flows, even if the resolution is low.

Table IV-2: Grid sizes and properties.

Grid	Cell size	y^+ minimum	y^+ (average)	Max y^+ maximum
Grid A (coarse)	505,800	0.93	5.23	12.5
Grid B (medium)	1519,800	0.26	2.35	5
Grid C (fine)	3618,480	0.23	0.71	1.02
Grid D (very fine)	4859,712	0.14	0.42	0.87

Simulations have been performed for the first configuration where the tubes all have a circular shape and validated by comparison with the experimental results of Balabani and Yianneskis [45].

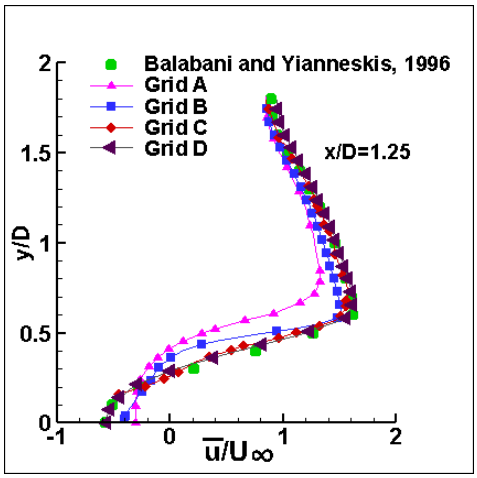

Figure IV-3: Spanwise profiles of the normalized average streamwise velocity; grid sensitivity.

The comparison between the computed normalized average streamwise velocity for the four grids and experimental data at x/D=1.25 are illustrated in Fig. IV-3. Computations on the first three grids demonstrate that data as the number of cells increases, the streamwise velocity is getting closer to experimental. However, with increasing grid size from grid C to grid D, the results remain almost constant and no significant change is observed.

The grid convergence index (GCI) method is handled in this study in order to estimate the uncertainty due to the mesh and to quantify the discretization error for the first three grids (B, C, D). This is a practical method of accounting the discretization error as a percentage based on the generalized Richardson extrapolation (GRE) [90-94].

Its principle takes the following steps:

• rate the grid refinement ratio r and the formal convergence order p using the following relationships:

$$r_{21} = b_2 / b_1 \text{ and } r_{32} = b_3 / b_2 \qquad \text{(IV-9)}$$

$$p = \frac{1}{\ln(r_{21})}\left|\ln\left|\frac{\varepsilon_{32}}{\varepsilon_{21}}\right| + \ln\left(\frac{r_{21}^{p} - s}{r_{32}^{p} - s}\right)\right| \qquad \text{(IV-10)}$$

with $s = sign(\varepsilon_{32} / \varepsilon_{21})$.

Equation (IV-10) is solved using a fixed-point iterative method where the formal order of accuracy can be used as an initial value. specify that ε_{21} and ε_{32} are the absolute error between two solutions viz f_1, f_2 and f_2, f_3, respectively, computed on two different grids with uniform discrete spacings, b_1 and b_2, corresponding to a fine and coarse grid spacing, while r is the grid refinement ratio, and p stands for the precision order of the discretization scheme. It is worth noting that f_1 being the fine grid solution, f_2 is the middle grid solution and f_3 is the coarse grid solution.

• Numerical uncertainty quantification

The numerical uncertainty quantification can be handled using the Roache's GCI method [90-94]. In this approach, the GCI index can be expressed as follow:

$$GCI^{21} = \frac{C_a}{r_{21}^{p} - 1} e_a^{21} \times 10^2 \qquad \text{(IV-11)}$$

where $r_{21}^{p} = (h_2 / h_1)^{1/d}$, d being the grid dimension, C_a is an adjustment factor that has been set at 1.25, and e_a^{21} is the approximate relative error ($= \varepsilon_{21} / f_1$). It should be reported that between grids 2 and 3,

the same relationships take place. In addition, according to Roache [90], at least three levels of grid refinement (coarse, medium, and fine) should be selected to determine the convergence appropriate order while ensuring that numerical predictions are within an asymptotic range.

Table 3 gathers the results for the drag coefficient on the last tubes used as a grid independence check variable for such an approach.

Table IV-3: GCI method results.

Grid	medium/fine (B/C)	fine/very fine (C/D)
Mesh refinement indices	$r_{21}^{p}=1.33$	$r_{32}^{p}=1.10$
Absolute errors	$\varepsilon_{21}=0.25$	$\varepsilon_{32}=0.021$
Convergence order	$p=3.52$	$p=3.52$
Extrapolated value	$f_{ext}^{21}=1.36$	$f_{ext}^{32}=1.70$
Relative errors	$e_{a}^{21}=16.66$	$e_{a}^{32}=1.21$
GCI %	$GCI^{21}=11.78$	$GCI^{32}=1.70$

From this Table 3, it can be seen that the error due to the refinement from the coarse to medium grid is of the order of 12%, whereas it is 1.7% (small value) for the refinement from medium to fine grid indicating that the error is insignificant to other possible sources of error, such as turbulence modelling, boundary conditions, etc. and the obtained solution is in a proper range. Thereby, the results presented in the remainder of this paper are achieved with the very finest grid, viz. the D grid.

IV.6 Computational results and discussion

Three-dimensional simulations have been performed for both configurations on the finest D-grid using the large eddy simulation method. The primary target of this study is to reproduce the mean flow from Balabani and Yianneskis [45] for the circular staggered tubes bundle in order to validate the methodology and subsequently the flow features. The results are also compared with those of Patel (2010), achieved via a numerical simulation with the SST model. After model validation, the two configurations are compared in terms of velocities, flow patterns and turbulences quantities.

IV.6.1 Velocity distributions and flow patterns

The time-averaged and dimensionless mean streamwise and spanwise velocities are compared to the measurements taken at eight locations highlighted in Figs. 1b and 1d, viz., x/D =0.85, 1.25, 2.95, 3.35, 5.05, 5.45, 7.15, and 7.5. Velocities are normalized with the inlet velocity and the spatial coordinates are normalized with the cylinder diameter D. Comparisons are made-up between our LES predictions, Patel SST results [95] and Balabani and Yianneskis [45] experimental data (see Figs. 4 and 5). As can be seen in Fig. IV-4, it is the WALE model which well predicts better the streamwise velocity ($\bar{u}/U_\infty$) whatever the location x/D. As can be observed at some stations, this velocity sometimes becomes negative, indicating the occurrence of a reverse flow. As for the transverse velocity ($\bar{v}/U_\infty$), it is globally better predicted by the LES model than the SST model (see Fig. IV-5). It can be seen that, from the third station, both models exhibit rather significant deviations. At the fifth and sixth rows (x/D = 5.05 and 5.45), the spanwise velocity is greatly overestimated by the SST model. However, at the last two stations (x/D = 7.15 and 7.55), the LES results agree better with Balabani and Yianneskis data compared to SST results which yet overestimate this velocity when y/D>1. In addition, since the average GCI is small (GCI <1.7%, see Table 3), one can state that the numerical uncertainty due to a discretization error does not contribute significantly to the disagreement between the predicted $\bar{u}$- and $\bar{v}$-velocities via the WALE model and the experimental data. Furthermore, it should be stressed that the wall-normal coordinate y^+ is such that $0.14 \le y^+ \le 0.87$ for the cylinders walls and $0.27 \le y^+ \le 1.08$ for the channel walls. Thereby, through these findings, it can be already stated such preliminary results support the WALE model.

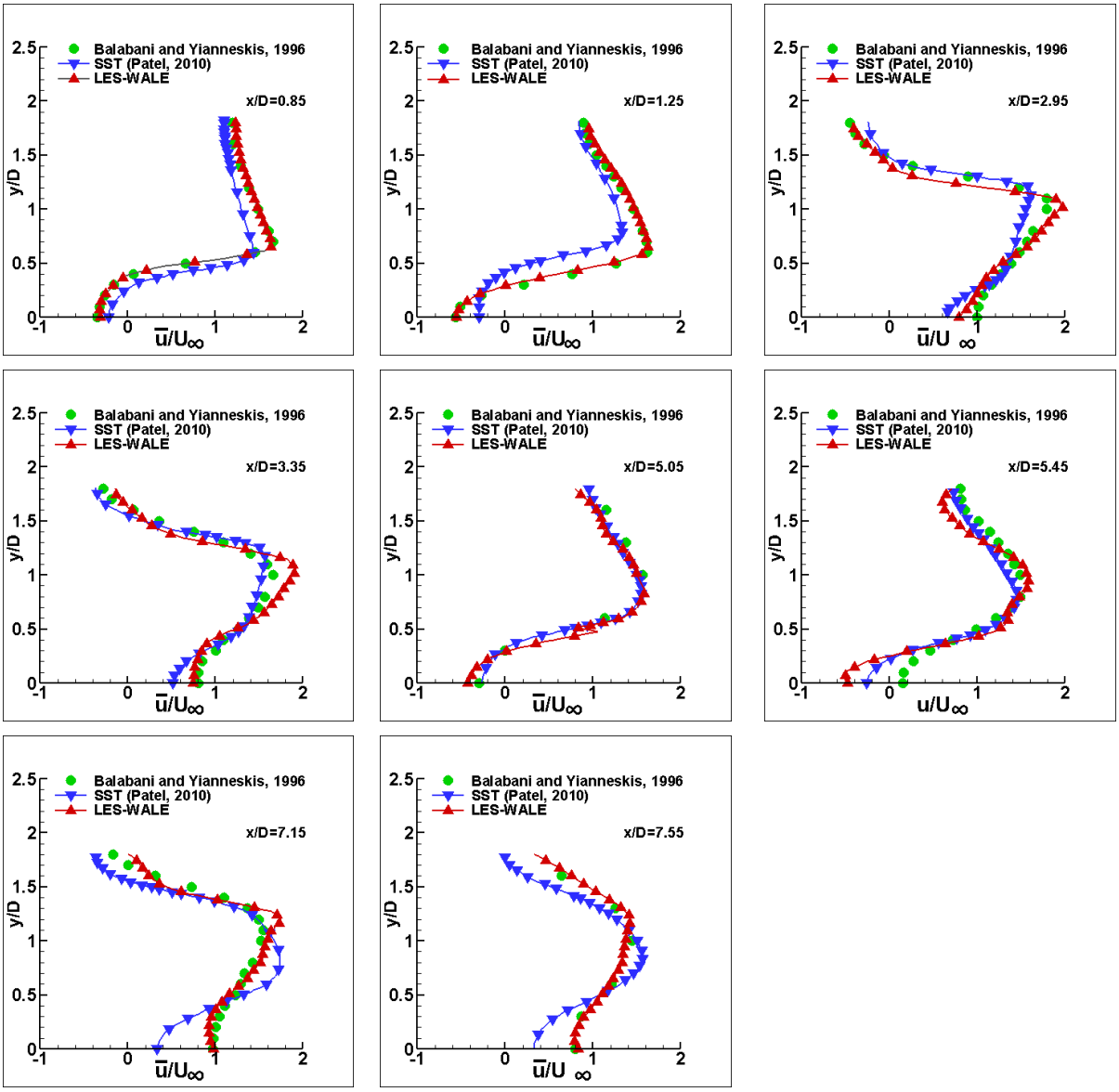

Figure IV-4: Streamwise dimensionless average velocity profiles $\overline{U}/U_\infty$ compared with experimental data and the SST model [95] at selected axial locations and z=0 .

The contours of normalized time averaged streamwise velocity for the two configurations are shown in Fig. IV-6. Results are presented for the mid-plane ($z=0$). It is found that the interference between tubes is more prominent in the mixed configuration compared to purely circular cylinders. In addition, the introduction of square rows tube makes the flow more accelerated, resulted in a larger recirculation's zone. Inverse velocities are higher in the mixed tube bundle and the shedding occurs in the tubes wake as expected. The highest velocities are between the tubes and the lowest are in the wake of tubes. At the exit, the flow rate is decelerated due to the absence of inhibiting flow in the next tubes row.

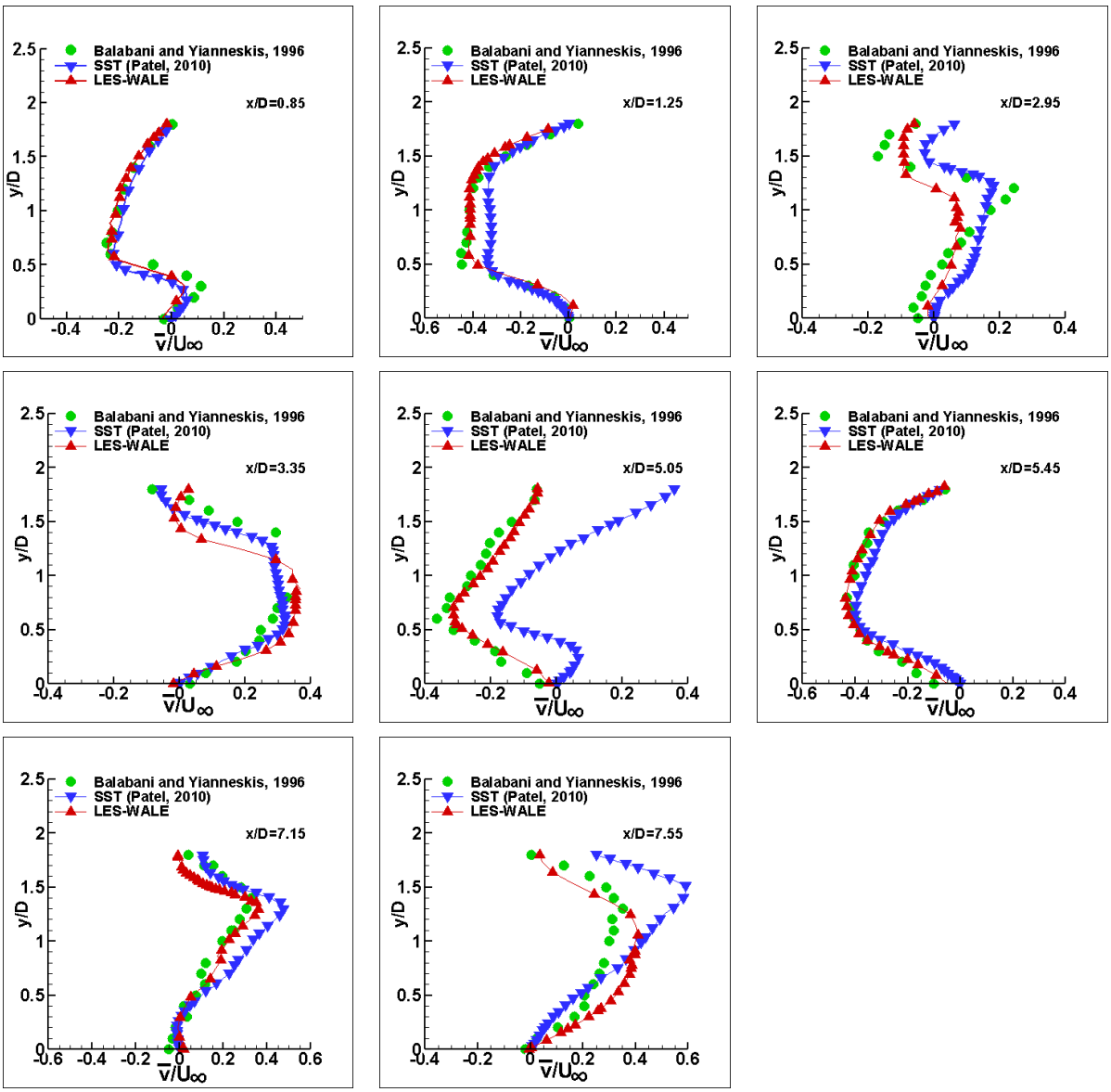

Figure IV-5: Transverse dimensionless average velocity profiles compared with experimental data and the SST model [95] at selected axial locations and z=0 .

In order to enhance the visualization of the shedding process the vorticity magnitude for the same instance is plotted as shown in Fig. IV-7. It's clear that the largest rotational structures in the flow occurs in the mixed configuration in which the flow swirl begins from the wake until the adjacent tube. Relatively high vorticity magnitude regions are observed behind the first and second rows in the downstream direction, however, its intensity reduces when reach the last row.

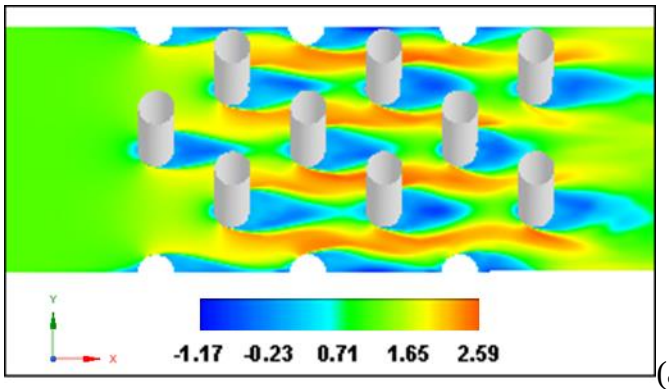

(a)

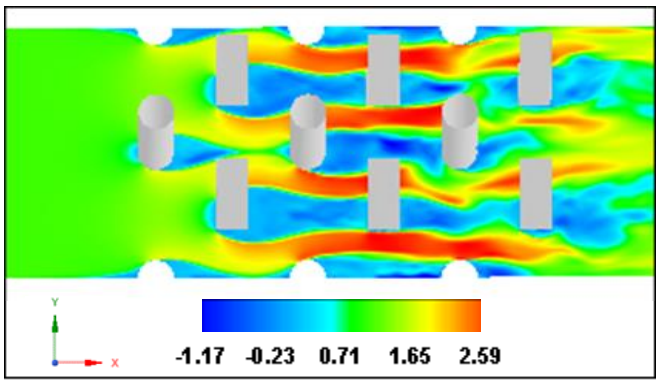

(b)

Figure IV-6: Dimensionless time-averaged streamwise velocity in x-y plane at z=0 (midplane) for circular (a) and mixed tubes bundles (b).

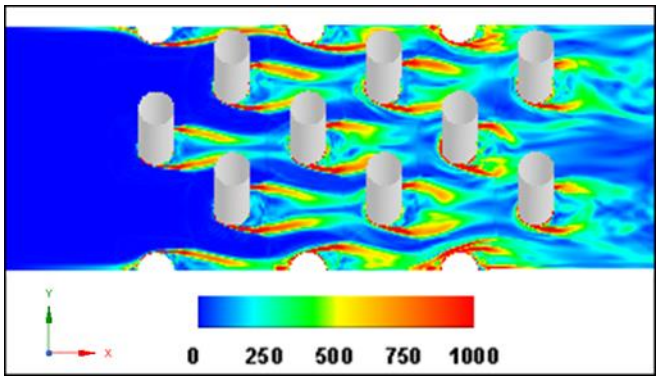

(a)

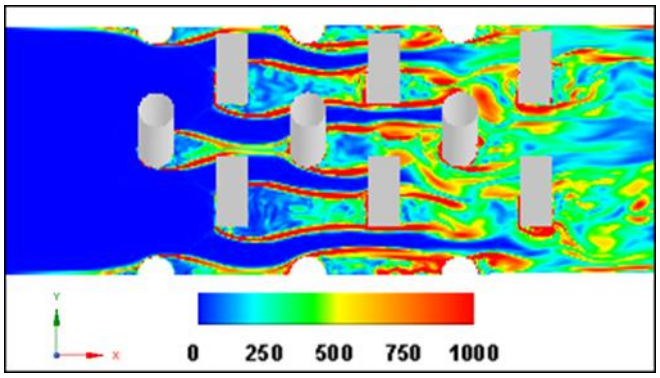

(b)

Figure IV-7: Instantaneous Vorticity magnitude contours in x-y plane at z=0 for around circular (a) and mixed tubes bundles (b).

From Fig. IV-8 that depicts the velocity vector, it can be observed the development of recirculation zones of different sizes in the wake region. Explicitly, recirculation zones appear at the top and bottom of the square cylinders of the second bundle. In total, six recirculation zones can be identified behind the first squares: one at the top, one at the bottom, two near the leeside of square and two others before the next square due to the interference between square tubes. Furthermore, the vortices behind the square cylinders are stronger and bigger than behind the circular cylinders in all rows. Once the flow passes the first square cylinders, the upper and lower vortices disappear from the next square cylinders. In the circular tube bundle, two main vortices develop in the wake region without interaction between the cylinders. For both configurations, it is set up that the flow reversal is more pronounced downstream of the first and second rows of cylinders.

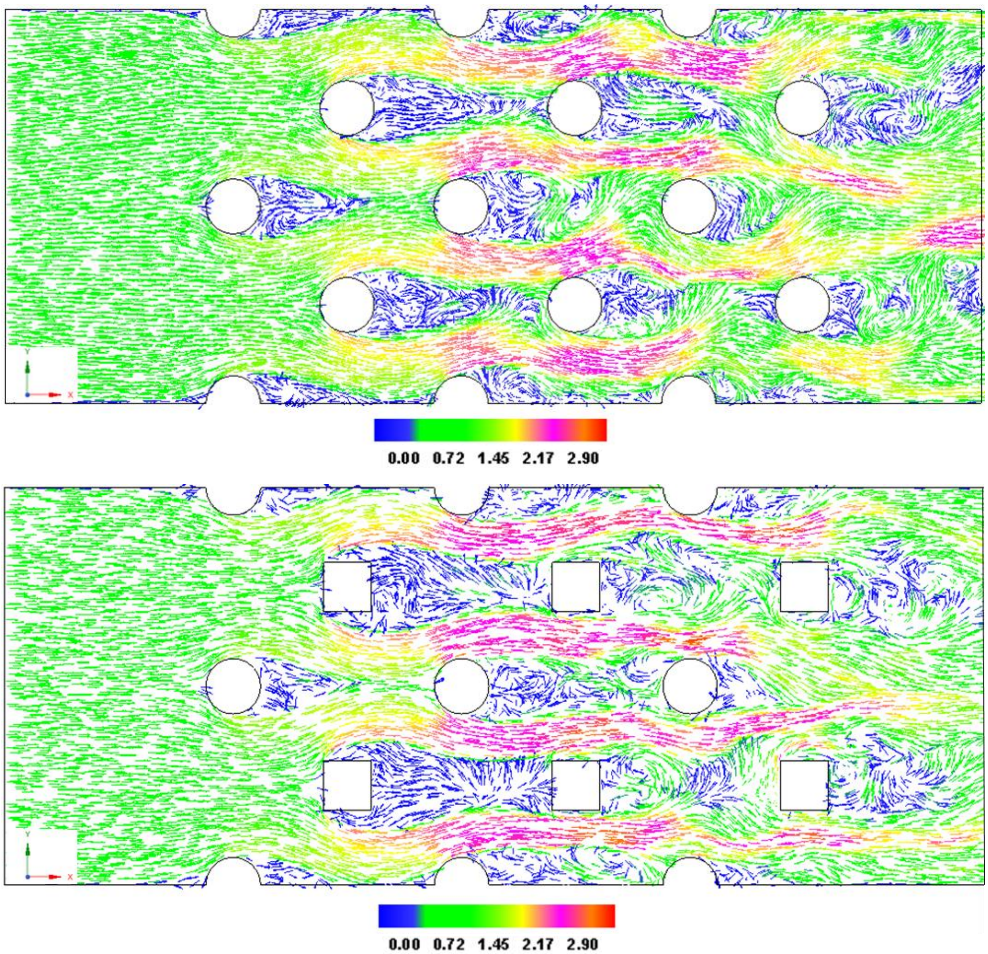

Figure IV-8: Averaged velocity vector contours around circular and mixed tube bundles in x-y plane at z=0.

Fig. IV-9 depicts the distribution of the normalized time-averaged velocity along the spanwise direction ($y-z$ plane) for both configurations at the position of $x/D=-1.2$ (before any obstacle) , $x/D=2.9$ (behind the first row tubes), $x/D=7.1$ (behind the second row tubes), $x/D=11.3$ (behind

the third row tubes) and the last stations at $x/D=13.8$. The first streamwise slices contours where no obstacle is confronted are similar, indicating that there is no tubes upstream effect on the flow. The streamwise velocity distribution at the second and third stations shows periodic repeats along the spanwise direction for the two configurations. At these stations, the streamwise velocity is assessed to be greater in the mixed model compared to the purely circular model, because of the different flow separation characteristics for the different square cylinders. Further downstream of $x/D=11.3$ and $x/D=13.8$, the parallel lines distributions of velocity disappeared along the spanwise direction and the flow is decelerated.

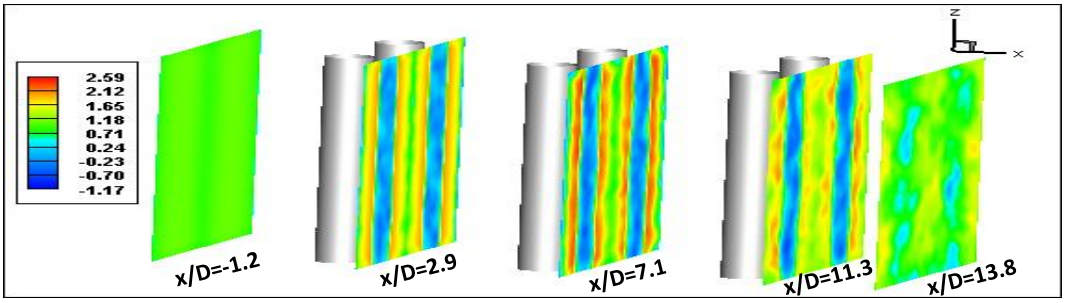

(a)

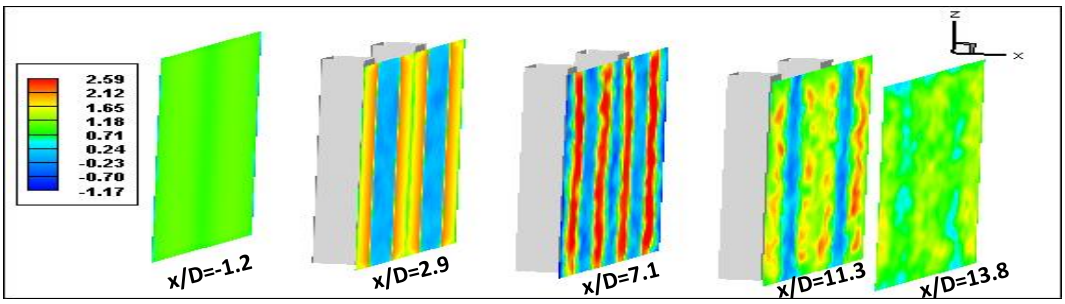

(b)

Figure IV-9: Dimensionless time-averaged streamwise velocity distributions in x-z plane at different locations x/D: (a) circular and (b) mixed tube bundles.

The streamlines plot of the full flow field shown in Fig. IV-10 demonstrate that purely circular cylinder arrays give rise to a more stable and organized flow pattern with less fluctuation. However, the introduction of square cylinders in the bundle results in a more chaotic flow. It is found that the recirculation regions become gradually small in the streamwise direction, and the recirculation length in the mixed model is bigger. In the wake region of the first tubes, it is observed that two main vortices are developed caused by the flow separation. When the flow reaches the second row of tubes, we notice the production of an upper and lower vortex for square cylinders. At this stage, the morphology of the flow becomes more complex. Furthermore, the length of the wake zone is increased to reach the next row.

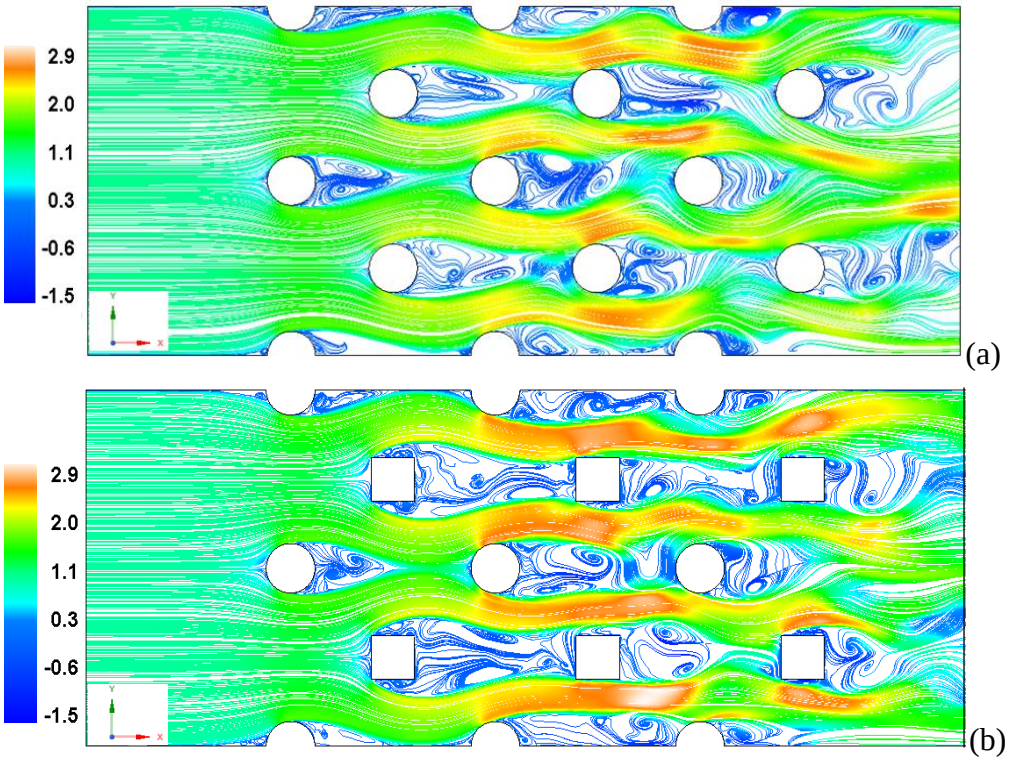

Figure IV-10: Streamlines colored by time averaged streamwise velocity in x-y plane at z=0 around (a) circular and (b) mixed tube bundles.

Fig. IV-11 depicts the iso-surfaces of the instantaneous vorticity magnitude in the flow for the two models. It can be seen an extremely complex flow distribution in the wake flow for the mixed configuration. In addition, the turbulent structures extent in the mixed model appears to be higher. Thereby, the iso-vorticity contours demonstrate the LES ability to capture full flow motion thus indicating that the adopted LES model is suited to handle complex turbulent flow through tubes bundles. The horseshoe vortex is developed for square and circular cylinders, caused by the interference between the cylinders and the channel flow. Downstream the fourth row, wake vortices are more prominent for the mixed configuration.

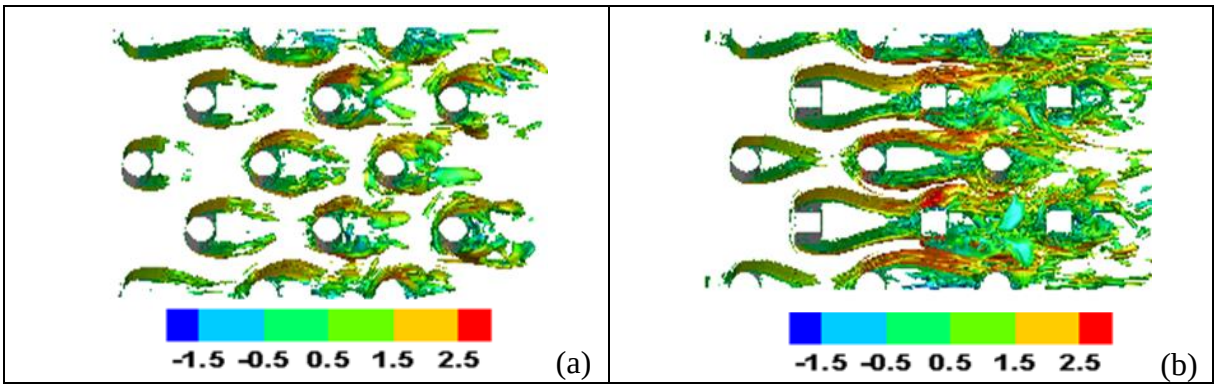

Figure IV-11: Instantaneous iso-surface vorticity colored with the streamwise velocity around (a) circular and (b) mixed tube bundles at z=0 and t=10 s.

Fig. IV-12 compares the dimensionless time-averaged streamwise velocity in the two bundles. It can be seen that, for the first two stations, the streamwise velocity are similar due to the fact that the two configurations at these stations have the same obstacles and the flow doesn't reach the square cylinders. There is no effect of the downstream on the upstream at these two locations. At the third and fourth stations, the flow is more accelerated between mixed tubes and decelerated near the square due to the reverse flow. The same phenomena are observed at stations x/D = 5.05 and 5.45. In addition, for distant stations (x/D > 5), the maximum velocity is higher (almost twice) in the mixed configuration compared to the circular tube bundle.

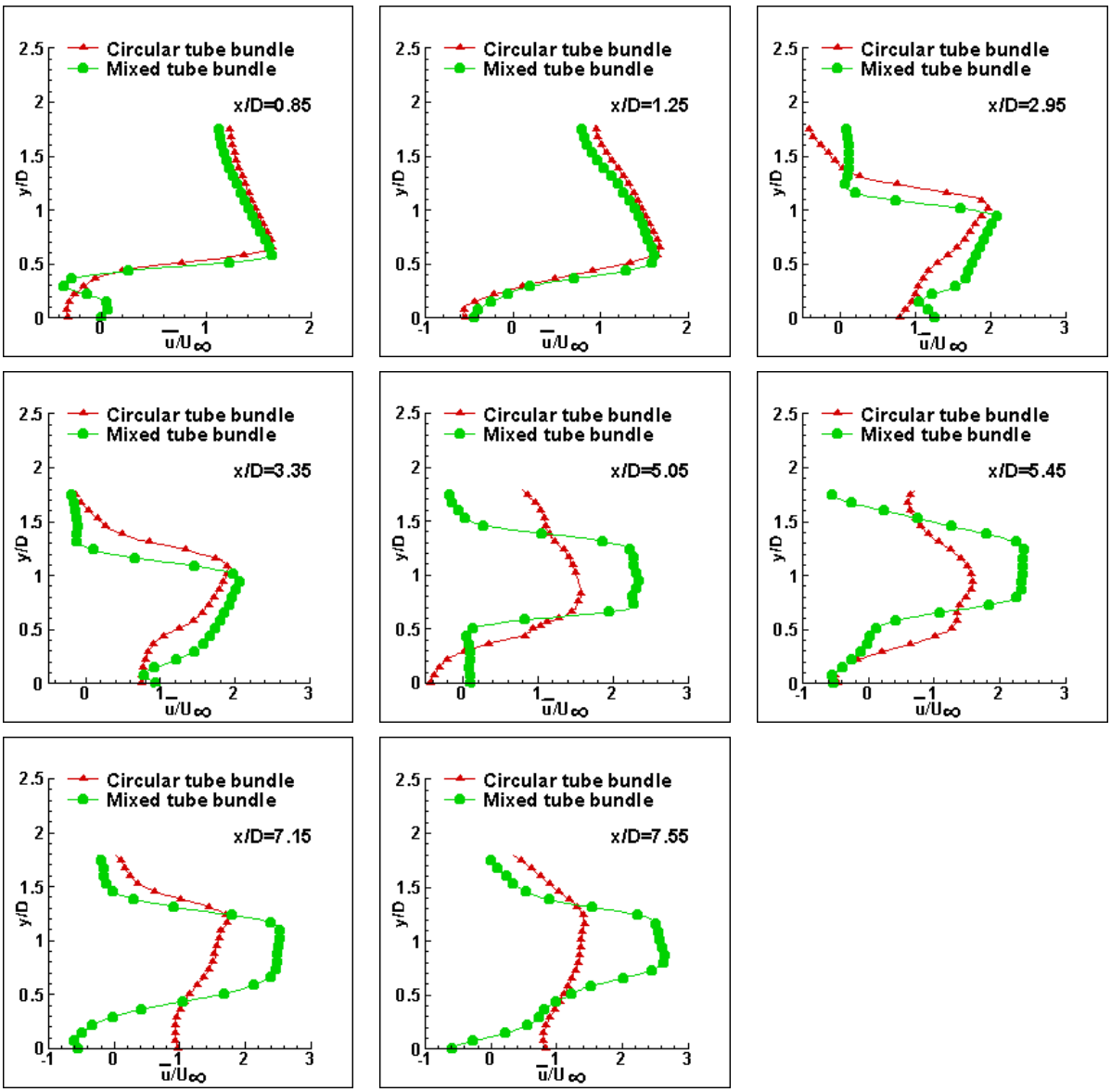

Figure IV-12: Dimensionless time averaged streamwise velocity comparison between the two bundles.

In Fig. IV-13, the normalized mean transverse velocity for the two tube bundles are compared at the same selected axial locations as the streamwise velocity. For the first three stations, this velocity exhibits almost similar profiles. Beyond, profiles differ. Explicitly, from x/D = 2.95 to 5.45, the transverse velocity for the mixed bundle is higher than circular tubes bundle for y/D <1. When the flow is closed to the next cylinder row (y/D >1), the transverse velocity is decreased with a higher gradient in mixed configuration. For last two stations, transverse velocity is higher in circular tubes bundle. Note that its maximum in the last station is ~ 0.15 for the mixed bundle and ~ 0.4 for the circular bundle.

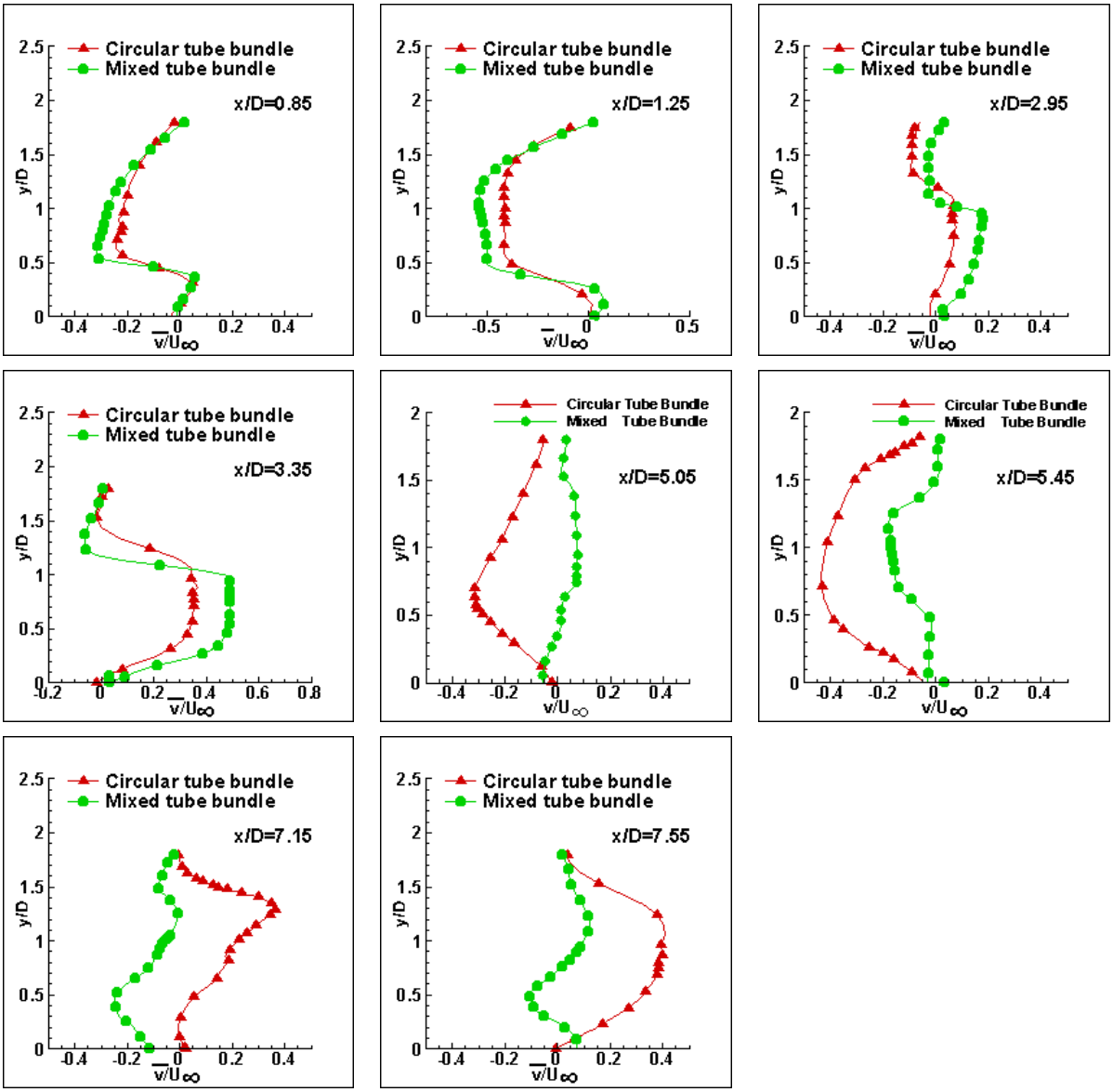

Figure IV-13: Dimensionless time averaged transverse velocity comparison between the two bundles.

IV.6.2 Turbulence kinetic energy, anisotropy degree and eddies identification

The normalized resolved turbulent kinetic energy (tke) is defined in terms of the SGS stress tensor trace as [96] to cite a few:

$$k_{sgs}^{+} = 0.5\overline{u_i' u_i'} / U_\infty{}^2 = 0.5\tau_{ii}^{sgs} / U_\infty{}^2 \qquad \text{(IV-12)}$$

Using summation notation, and u_i' is the SGS part of the non-filtered velocity u_i. Note that a transport equation for k can then be derived via the trace of the transport equation for the SGS stress tensor, while modeling the diffusion and dissipation terms.

Fig. IV-14 presents the normalized turbulence kinetic energy contours in mid-plane z. It is found to be associated with the flow structures and patterns of each arrangement showed in previous sections, as the regions with the highest k values are those with the greatest vorticity. It appears that in both configurations, the distribution of turbulent energy is very different in the last rows, involving more vortices in the mixed configuration. This energy is generated in the wake regions and then dissipated gradually in the mainstream flow. Downstream of the first two rows of cylinders, the tke is very low, then is increased downstream of the other rows due to the strongest eddies to reach its

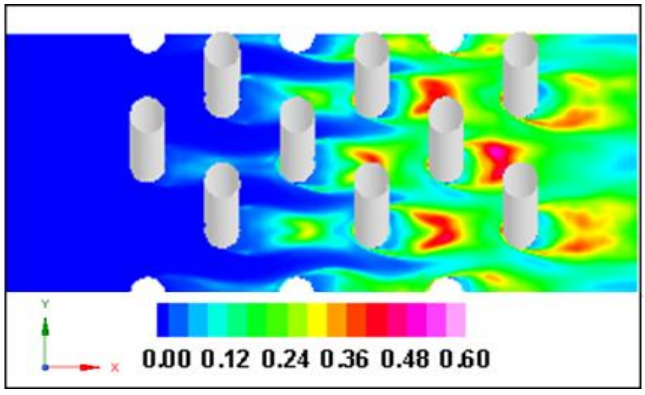

(a)

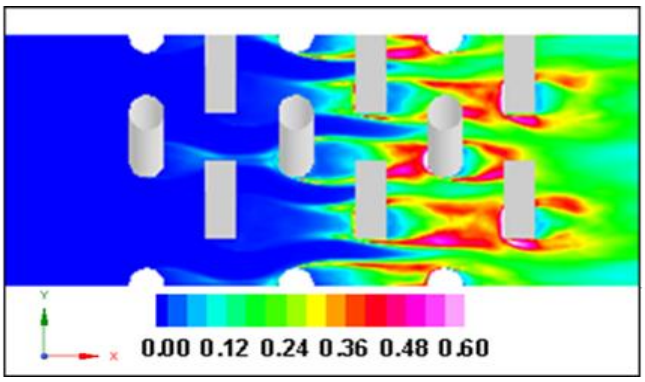

(b)

Figure IV-14: Dimensionless resolved tke contours around circular tube bundle (a) and mixed tube bundle (b) in x-y plane at z=0.

maximum value found downstream of fourth and fifth rows. The intensity of the turbulent flow structures being greater in the mixed model, a vibration could occur.

Fig. IV-15 depicts the dimensionless distribution of |v'-u'|. These contours provide an indication of the turbulence anisotropy degree. Downstream of the first two lines, the anisotropy is weak, whereas it increases downstream of the other rows, except for the last one. To sum up, the mixed arrangement exhibits a larger gap between the two velocities root mean square (rms) pointing out that the flow is more anisotropic than in the purely circular model.

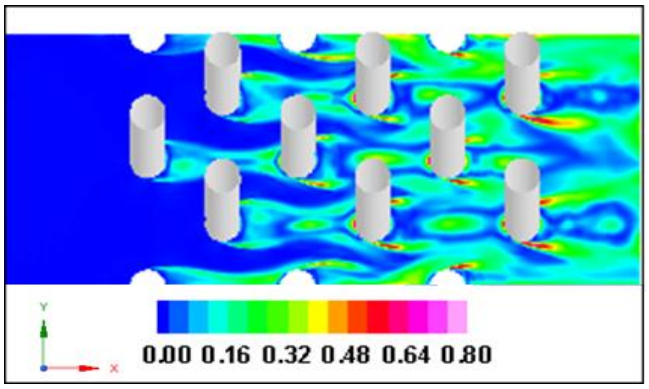

(a)

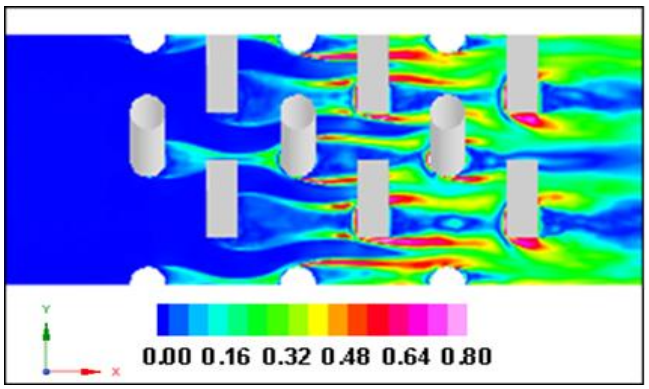

(b)

Figure IV-15: Turbulence anisotropy via |v'-u'|-dimensionless contours around circular tube bundle (a) and mixed tube bundle (b) in x-y plane at z=0 .

In what follows, the coherent three-dimensional structures can be identified via the criterion Q described in the previous chapter. Note that Dubief and Delcayre [97] pointed out its superiority on the low-pressure criterion in wall-bounded turbulent flows. The iso-surfaces plot of coherent eddies is depicted in Fig. IV-16 for both configurations at various instants. It shows different structures educed via the Q-criterion and colored by the velocity magnitude. It reveals a set of coherent eddies in the flow evolving irregularly throughout the tubes bundle, stretching due to high velocity gradients and distorting in hairpin and/or horseshoe shapes from the first and second rows. It appears that the mixed configuration involves many and strong eddies with higher density,

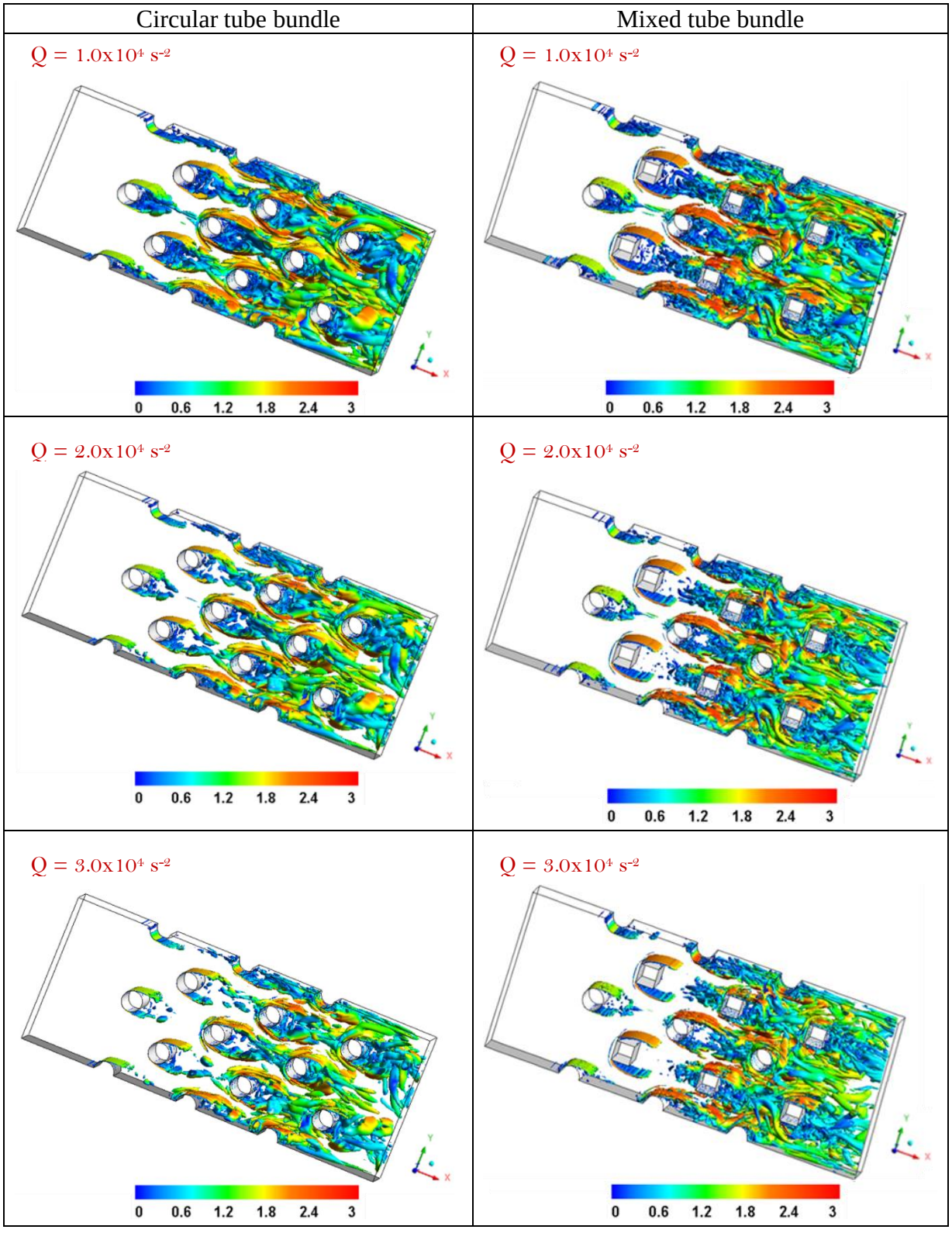

Figure IV-16: Coherent eddies via the Q criterion's iso-surface within both configurations at $t = 10s$ coloring by the velocity magnitude.

especially for the larger Q value ($3x10^4\ s^{-2}$). From the third row, the density and distortion degree of the iso-vortex surfaces increase in both configurations, highlighting the strongly turbulent character of these areas, and thereby, confirming the unveiling of Figs. 14 and 15.

IV.7 Conclusion

In this chapter, time dependent calculations of the subcritical cross flow through a staggered purely circular and mixed tube bundle have been performed with Large eddy simulation method. Time averaged streamwise velocity is used to choose the appropriate grid size in the simulation combined with the GCI method that is a good approach to test the solution dependency to the mesh. The LES method demonstrates that the mean streamwise and tranverse velocities profiles were reasonably well predicted compared to experimental data. For the two configurations, a reverse flow occurred in the wake region and the flow perturbations due to the unsteady nature of the vortex shedding are more prominent in square cylinders than circular. Furthermore, the analysis of the flow features demonstrates that the mixing between the circular and square tubes results in instable and disorganized flow pattern with interference between tubes and the flow becomes more chaotic. The velocity goes higher in the mixed model compared to circular tubes configuration. In the mixed arrangement, the turbulence is more anisotropic and the intensity of the turbulent structures of the flow is bigger, that could result in a strong vibration.

GENERAL CONCLUSION

General Conclusion

In this thesis, the flow past a single and array of obstacles is studied using numerical approaches. In the first part, a numerical study using the Shear Stress Transport K-ω model was carried out in order to investigate the impact of rounded edges on the cooling effectiveness of electronic components subjected to a cross flow and an impinging jet. It turned out that the adopted SST demonstrates that mean streamwise velocities were reasonably well predicted compared to the experimental data. We have shown that the heat flux is enhanced with the increase of the impinging to cross flow Reynolds number ratio for all cube geometries. Additionally, the flow features and coherent structures developed closer to components considerably influence the wall heat transfer. For the ratio value of 0.5, the impinging jet was dragged and did not impact the component, which results in almost similar flow patterns for all cube geometries. Because of this similarity in the vortical structures, no cooling enhancement is shown by rounding the top corners of the component. It is found that the use of rounded edges with a radius-to-height ratio of 2/15 can improve the heat effectiveness by more than 6% for $\mathrm{Re}_j / \mathrm{Re}_H = 1$. Furthermore, in the case of $\mathrm{Re}_j / \mathrm{Re}_H = 1.5$, the heat transfer on the global surface of the cube can be enhanced by more than 23% thanks to the use of curved edges with a radius-to-height ratio of 6/15 on the top of electronic component. For the ratio of 1.5, it is important to point out that an almost homogeneous cooling is achieved for the cube D (R=6mm).

In the second part of the thesis, the time-dependent computations of the flow through a staggered purely circular and mixed tubes bundle are performed using large eddy simulation. Moreover, the GCI method is used to assess the grid refinement influence on the solution. It turned out that the adopted LES demonstrates that mean streamwise and transverse velocities predicted reasonably corroborate the available experimental data. In addition, the quantities obtained with the LES-WALE model are in better agreement with the experimental data compared with those of the SST model. For the two configurations, a reverse flow occurs in the wake region and flow perturbations, due to the unsteady nature of the vortex shedding, are more prominent in the square than circular cylinders. Furthermore, the analysis of the flow features demonstrates that the mixing between the circular and square tubes results in instable and disorganized flow pattern with interference between tubes while exhibiting a more chaotic flow. In addition, the velocity increases in the mixed configuration compared to that with circular tubes. Finally, among the two arrangements, it is the mixed which exhibits a more anisotropic flow with many and more intense eddies. From the stability point of view, it is the circular tube bundle that is often advised. However,

to better generate coherent structures which are generally associated with heat transfer, the mixed bundle can be used to improve cooling efficiency. The latter deserves further study.

International Publications:

1- Numerical Study on the Performance of Rounded Corners on the Top of Electronic Components on Cooling Effectiveness, International Journal of Heat and Mass Transfer Volume 150, April 2020, 119391. https://doi.org/10.1016/j.ijheatmasstransfer.2020.119391

2- Large Eddy Simulation of a Turbulent Flow over Circular and Mixed Staggered Tubes' Cluster. Journal of Applied Fluid Mechanics, Vol. 13, No. 5, pp. 1471-1486, 2020. https://doi: 10.36884/jafm.13.05.31119

International Communications:

1- A numerical comparative study of fluid flow past cylindrical and mixed staggered tube bundle by LES Method. The Fourth International Conference on Fracture Mechanics, FRACT'4 November 26 - 29, 2018, Chlef, Algeria.

National Communications:

1- Numerical Simulation of Flow Past a Circular Cylinder, (The Second Students Symposium on Engineering Application of Mechanics (SSENAM'2), 13-14 December 2017. Chlef, Algeria.

2- Numerical Investigation of Flow Past In A Staggered Tube Bundle. (The Third Students Symposium on Engineering Application of Mechanics (SSENAM'3) 02-03 Mai 2018, Mascara, Algeria.

3- Numerical Comparative Study of the Flow Past Different Obstacles with the Large Eddy Simulation Method. (The Forth Students Symposium on Engineering Application of Mechanics (SSENAM'4) 18-19 December 2018, Bechar, Algeria.

References

[1] W. Gao, W. Wang, D. Dimitrov, Y. Wang, Nano properties analysis via fourth multiplicative ABC indicator calculating, j.arab.j.c. 11(2018) 793-801. https://doi.org/10.1016/j.arabjc.2017.12.024

[2] M. Bahiraei, S. Heshmatian, M. Keshavarzi, Multi-attribute optimization of a novel micro liquid block working with green graphene nanofluid regarding preferences of decision maker, j. appl. thermal eng. 143 (2018) 11-21. https://doi.org/10.1016/j.applthermaleng.2018.07.074

[3] M. Bahiraei, S. Heshmatian, Thermal performance and second law characteristics of two new microchannel heat sinks operated with hybrid nanofluid containing graphene–silver nanoparticles, j. en. con. man. 168 (2018) 357-370. https://doi.org/10.1016/j.enconman.2018.05.020

[4] M. Bahiraei, S. Heshmatian, M. Keshavarzi, A decision-making based method to optimize energy efficiency of ecofriendly nanofluid flow inside a new heat sink enhanced with flow distributor, j. pow. tec. 342 (2019) 85-98. https://doi.org/10.1016/j.powtec.2018.10.007

[5] M. Bahiraei, S. Heshmatian, Electronics cooling with nanofluids: A critical review, j.en. con. man. 172, 15 (2018) 438-456. https://doi.org/10.1016/j.enconman.2018.07.047

[6] M. Goodarzi, I. Tlili, Z. Tian, M. Safaei, Efficiency assessment of using graphene nanoplatelets-silver/water nanofluids in microchannel heat sinks with different cross-sections for electronics cooling, Int. J. Num. Meth. Heat Fluid Flow, Vol. ahead-of-print No. ahead-of-print. https://doi.org/10.1108/HFF-12-2018-0730

[7] M.R. Safaei, M. Gooarzi, O. A. Akbari, M. S. Shadloo, M. Dahari, Performance Evaluation of Nanofluids in an Inclined Ribbed Microchannel for Electronic Cooling Applications, Electronics Cooling, S M Sohel Murshed, IntechOpen, doi: 10.5772/62898

[8] R. Dadsetani, M. Salimpour, M. Tavakoli, M. Goodarzi, E. Pedone Bandarra Filho, Thermal and mechanical design of reverting microchannels for cooling disk-shaped electronic parts using constructal theory, Int. J. Num. Meth. Heat Fluid Flow, Vol. ahead-of-print No. ahead-of-print. https://doi.org/10.1108/HFF-06-2019-0453

[9] M. Bahiraei, S. Heshmatian, M. Goodarzi, H. Moayedi, CFD analysis of employing a novel ecofriendly nanofluid in a miniature pin fin heat sink for cooling of electronic components: Effect of different configurations, j. pow. tec. 30 (2019) 2503-2516. https://doi.org/10.1016/j.apt.2019.07.029

[10] B. Sahin, E. Manay, V. Ozceyhan, Overall Heat Transfer Enhancement Of Triangular Obstacles, Int. J. Aut. Mech. Eng. 8 (2013) 1278-1291. http://dx.doi.org/10.15282/ijame.8.2013.17.0105

[11] A. Leon Octavio, D.M. Gilbert, D. Erik, V. Jan, Staggered heat sinks with aerodynamic cooling fins, Microelectron. Reliab. 44 (2004) 1181–7. doi:10.1016/j.microrel.2004.03.003

[12] W. Qiao, Z. Yang, Solving Large-Scale Function Optimization Problem by Using a New Metaheuristic Algorithm Based on Quantum Dolphin Swarm Algorithm, Access IEEE, 7 (2019) 138972- 138988. DOI: 10.1109/ACCESS.2019.2942169

[13] W. Qiao, Z. Yang, Modified dolphin swarm algorithm based on chaotic maps for solving high-dimensional function optimization problems, Access IEEE, 7 (2019) 110472 – 110486. DOI: 10.1109/ACCESS.2019.2931910

[14] P. Martínez-Filgueira, E. Zulueta, A. Sánchez-Chica ,U. Fernández-Gámiz, J. Soriano, Multi-Objective Particle Swarm Based Optimization of an Air Jet Impingement System, Energies, 12 (2019) 1627. DOI: 10.3390/en12091627.

REFERENCES

[15] W. Qiao, Z. Yang , Modified Dolphin Swarm Algorithm Based on Chaotic Maps for Solving High-Dimensional Function Optimization Problems, IEEE Access, 7 (2019) 110472-110486. DOI: 10.1109/ACCESS.2019.2931910.

[16] W. Qiao, Z. Yang, An Improved Dolphin Swarm Algorithm Based on Kernel Fuzzy C-Means in the Application of Solving the Optimal Problems of Large-Scale Function, 8 (2019) 2073 – 2089. DOI: 10.1109/ACCESS.2019.2958456.

[17] W. Qiao, W. Tian, Y. Tian, Q. Yang, Y. Wang, J. Zhang, The Forecasting of PM2.5 Using a Hybrid Model Based on Wavelet Transform and an Improved Deep Learning Algorithm. 7 (2019) 142814 – 142825. DOI: 10.1109/ACCESS.2019.2944755.

[18] V.S. Bhandari, S. H.Kulkarni, Optimization of heat sink for thyristor using particle swarm optimization, Res. Eng. 4 (2019) 100034. https://doi.org/10.1016/j.rineng.2019.100034

[19] A. Yildizeli, S. Cadirci, Multi objective optimization of a micro-channel heat sink through genetic algorithm, Int. J. Heat Mass Transfer 146, (2020) 118847. https://doi.org/10.1016/j.ijheatmasstransfer.2019.118847.

[20] D. Rundström, B. Moshfegh, Investigation of flow and heat transfer of an impinging jet in a cross-flow for cooling of a heated cube, ASME J. Electronic Pack. 128 (2006a) 150–156. doi:10.1115/1.2188948

[21] D. Rundström, B. Moshfegh, RSM predictions of an impinging jet in a cross flow on a wall-mounted cube, In Proceedings of the 13th International Heat Transfer Conference, Sydney, Australia, (2006) 13–18.

[22] D. Rundström, B. Moshfegh, RSM and study on the flow behaviour of an impinging jet in a cross-flow on a wall-mounted cube, Prog. Comput. Fluid Dyn. 7 (2007) 311–322. doi:10.1504/PCFD.2007.014681

[23] D. Rundström, B. Moshfegh, Investigation of Heat Transfer and Pressure Drop of an Impinging Jet in a Cross flow for Cooling of a Heated Cube, J. Heat Transfer, 130 (2008) 121401-1. doi:10.1115/1.2969266

[24] D. Rundström, B. Moshfegh, Large-eddy simulation of an impinging jet in a cross-flow on a heated wall-mounted cube, Int. J. Heat Mass Transfer 52, (2009) 921–931. https://doi.org/10.1016/j.ijheatmasstransfer.2008.03.035

[25] H. N. Hajime, T. Igarashi, T.Tsutsui, Local heat transfer around a wall mounted cube in the turbulent boundary layer, int. j. heat mass transfer, 44 (2001) 3385-3395. doi: 10.1016/s0017-9310(01)00009-6

[26] M. Popovac, K. Hanjalic, Large-eddy simulations of flow over a jet-impinged wall-mounted cube in a cross stream, Int. J. Heat Fluid Flow, 28 (2007) 1360–1378. doi:10.1016/j.ijheatfluidflow.2007.05.009

[27] M. Popovac, K. Hanjalic, Vortices and heat flux around a wall-mounted cube cooled simultaneously by a jet and a crossflow, Int. J. Heat Mass Transfer 52 (2009) 4047–4062. doi:10.1016/j.ijheatmasstransfer.2009.03.042

[28] M.J. Tummers, M.A. Flikweert, K. Hanjali, R. Rodink, B. Moshfegh, Impinging jet cooling of wall mounted cubes, Eng. Turb. Mod. Exp. (2005) 773-782. https://doi.org/10.1016/B978-008044544-1/50074-1

[29] Y. Masip, A. Rivas, G. S. Larraona, A . Anton, J.C. Ramos, B. Moshfegh, Experimental study of the turbulent flow around a single wall-mounted cube exposed to a cross-flow and an impinging jet, Int. J. Heat Fluid Flow, 38 (2012) 50–71. http://dx.doi.org/10.1016/j.ijheatfluidflow.2012.07.004

[30] S. Nemdili, F. Nemdili, A. Azzi, Improving cooling effectiveness by use of chamfers on the top of electronic components, Microelectronics Reliability 55 (2015) 1067–1076. http://dx.doi.org/10.1016/j.microrel.2015.04.006

[31] R. Jason Hearst, G. Gomit, B. Ganapathisubramani, Effect of turbulence on the wake of a wall-mounted cube, J. Fluid Mech. 804 (2016) 513-530. doi:10.1017/jfm.2016.565

[32] A. Meghdir, T. Benabdallah, Z.E. Ahmed Dellil, Impact of Geometry of Electronic Components on Cooling Improvement, Int. J. Heat Tech. 37 (2019) 167-178. https://doi.org/10.18280/ijht.370121

[33] D. Bouris, G. Bergeles, Two-dimensional time dependent simulation of the subcritical flow in a staggered tube bundle using a subgrid scale model, Int. J. Heat Fluid Flow 20 (1999) 105-114. https://doi.org/10.1016/S0142-727X(98)10053-X.

[34] K. Lam, Y.F. Lin, L. Zou, Y. Liu, Experimental study and large eddy simulation of turbulent flow around tube bundles composed of wavy and circular cylinders, Int. J. Heat Fluid Flow 31 (2010) 32-44. https://doi.org/10.1016/j.ijheatfluidflow.2009.10.006.

[35] H.R. Barsamian, Y.A. Hassan, Large eddy simulation of turbulent crossflow in tube bundles, Nucl. Eng. Des. 172 (1997) 103-122. https://doi.org/10.1016/S0029-5493(97)00034-4.

[36] Y.A. Hassan, H.R. Barsamian, Tube bundle flows with the large Eddy simulation technique in curvilinear coordinates, Int. J. Heat Mass Transfer 47 (2004) 3057-3071. https://doi.org/10.1016/j.ijheatmasstransfer.2004.02.026.

[37] H. Wang, L. Daogang, Large eddy simulation on the turbulent flow and mixing in a 2x2 rod bundle, Ann. Nucl. Energy 133 (2019) 549-561. https://doi.org/10.1016/j.anucene.2019.07.005.

[38] M. Salinas-Vázquez, M.A. de la Lama, W. Vicente, E. Martínez, Large Eddy Simulation of a flow through circular tube bundle, Appl. Math. Model. 35 (2011) 4393-4406. https://doi.org/10.1016/j.apm.2011.03.003

[39] M. Tutar, A.E. Hold, Computational modelling of flow around a circular cylinder in subcritical flow regime with various turbulence models, Int. J. Numer. Meth. Fluids 35 (7) (2010)763-784. https://doi.org/10.1002/1097-0363(20010415)35:7<763::AID-FLD112>3.0.CO;2-S

[40] R. Perrin, M. Braza, E. Cid, S. Cazin, A. Barthet, A. Sevrain, Y. Hoarau, Near-wake turbulence properties in the high Reynolds number incompressible flow around a circular cylinder measured by two- and three-component PIV, Flow Turbul. Combust. 77 (2006) 185-204. https://doi.org/10.1007/s10494-006-9043-5.

[41] H. Xiao, Y. Zhang, W. Chen, L. Liming Zhang, The research on coherent structure in 7-rod bundle lattice, Ann. Nucl. Energy 124 (2019) 39-48. https://doi.org/10.1016/j.anucene.2018.09.027.

[42] B.H. Yan, H.Y. Gu, L. Yu, Unsteady Reynolds Averaged Navier–Stokes simulation of the turbulent flow pulsation and coherent structures in a tight lattice in rolling motion, Ann. Nucl. Energy 38 (2011) 1023-032. http://dx.doi.org/10.1016/j.anucene.2011.01.010.

[43] G. Duan, B. Chen, Large eddy simulation by particle method coupled with sub-particle-scale model and application to mixing layer flow, Appl. Math. Model. 39 (2015) 3135–3149. https://doi.org/10.1016/j.apm.2014.10.058.

[44] U. Piomelli, Large eddy simulations in 2030 and beyond, Phil. Trans. R. Soc. A 372 (2014) 20130320. https://doi.org/10.1098/rsta.2013.0320.

[45] S. Balabani, M. Yianneskis, An experimental study of the mean flow and turbulence structure of cross-flow over tube bundles, Proc. Instn. Mech. Engrs. 210 (1996) 317-331. https://doi.org/10.1243/PIME_PROC_1996_210_204_02.

[46] C. Liang, G. Papadakis, Large eddy simulation of cross-flow through a staggered tube bundle at subcritical Reynolds number, J. Fluid Struct. 23 (2007) 1215-1230. https://doi.org/10.1016/j.jfluidstructs.2007.05.004.

[47] B.L. da Silva, R.D. Luciano, J. Utzig, H.F. Meier, Flow patterns and turbulence effects in large cylinder arrays, Int. J. Heat Fluid Flow 69 (2018) 136-149. https://doi.org/10.1016/j.ijheatfluidflow.2017.12.013.

[48] B.L. da Silva, R.D. Luciano, J. Utzig, H.F. Meier, Analysis of flow behavior and fluid forces in large cylinder bundles by numerical simulations, Int. J. Heat Fluid Flow 75 (2019) 209-226. https://doi.org/10.1016/j.ijheatfluidflow.2019.01.006.

[49] S. Benhamadouche, D. Laurence, LES, coarse LES, and transient RANS comparisons on the flow across a tube bundle, Int. J. Heat Fluid Flow 24 (2003) 470-479. https://doi.org/10.1016/S0142-727X(03)00060-2.

[50] X. Zhengtong, I.P. Castro, LES and RANS for turbulent flow over arrays of wall-mounted obstacles, Flow Turbul. Combust. 76 (2006) 291-312. https://doi.org/10.1007/s10494-006-9018-6.

[51] A. Oengören, S. Ziada, An in-depth study of vortex shedding, acoustic resonance and turbulent forces in normal triangle tube arrays, J. Fluid Struct. 12 (1998) 717-758. https://doi.org/10.1006/jfls.1998.0162.

[52] Y. Kahil, S. Benhamadouche, A.S. Berrouk, I. Afgan, Simulation of subcritical-Reynolds-number flow around four cylinders in square arrangement configuration using LES, J. Europ. Mechanics/B Fluids 74 (2019) 111-122. https://doi.org/10.1016/j.euromechflu.2018.11.008.

[53] Chatterjee D, Biswas G. Dynamic behavior of flow around row of square cylinders kept in staggered arrangement, Journal of Computers & Fluids,2015.

[54] Chatterjee D, Biswas G, Amiroudine S. Numerical simulation of flow past row of square cylinders for various separation ratios. Journal of Computers & Fluids.

[55] D. Lakehal, Highly-resolved LES of turbulent convective flow along a PWR rod bundle, Int. J. Heat Mass Transfer 122 (2018) 785-794. https://doi.org/10.1016/j.ijheatmasstransfer.2018.01.099.

[56] M. Labois, D. Lakehal, Very-Large Eddy Simulation (V-LES) of the flow across a tube [7] K. bundle, Nucl. Eng. Des. 241 (2011) 2075-2085. https://doi.org/10.1016/j.nucengdes.2011.02.009.

[57] Lam, Y.F. Lin, L. Zou, Y. Liu, Experimental study and large eddy simulation of turbulent flow around tube bundles composed of wavy and circular cylinders, Int. J. Heat Fluid Flow 31 (2010) 32-44. https://doi.org/10.1016/j.ijheatfluidflow.2009.10.006.

[58] B. Mikuz, I. Tiselj, Wall-resolved Large Eddy Simulation in grid-free 5×5 rod bundle of MATiS-H experiment. Nucl. Eng. Des. 298 (2016) 64-77. https://doi.org/10.1016/j.nucengdes.2015.12.021.

[59] Lee, S.J, Lee S, Hassan Y.A, Numerical investigation of turbulent flow in an annular sector channel with staggered semi-circular ribs using large eddy simulation, International Journal of Heat and Mass Transfer 123 (2018) 705–717.

[60] Sal Rodriguez, Applied Computational Fluid Dynamics and Turbulence Modeling, Practical Tools, Tips and Techniques. Sandia National Laboratories Albuquerque, NM, USA. Springer Nature Switzerland AG 2019. https://doi.org/10.1007/978-3-030-28691-0

[61] Sreenivas Jayanti, Computational Fluid Dynamics for Engineers and Scientists. Department of Chemical Engineering Indian Institute of Technology Madras Chennai India. Springer Nature Switzerland AG 2019. https://doi.org/10.1007/978-94-024-1217-8.

[62] Imran Afgan, large eddy simulation of flow over cylindrical bodies using unstructured finite meshes School of Mechanical, Aerospace and Civil Engineering. Phd Thesis, July 2017.

[63] Ismail B. Celik, Introductory Turbulence Modeling, Lectures Notes. West Virginia University Mechanical & Aerospace Engineering Dept. P.O. Box 6106 Morgantown, WV 26506-6106, December 1999.

[64] FR. Menter, Two-equation eddy-viscosity turbulence models for engineering applications, AIAA Paper, 32 (1994) 1598-1605. https://doi.org/10.2514/3.12149

[65] H. Togun, M.R. Safaei, R. Sadri, S.N. Kazi, A. Badarudin, K. Hooman, E. Sadeghinezhad, Numerical simulation of laminar to turbulent nanofluid flow and heat transfer over a backward-facing step. App. Math. Comp. 239 (15) (2014) 153-170. https://doi.org/10.1016/j.amc.2014.04.051

[66] M. R. Safaei, H. Togun, K. Vafai, S. N. Kazi, A. Badarudin, Investigation of heat transfer enhancement in a forward-facing contracting channel using FMWCNT nanofluids, numerical heat transfer, Part A: Applications, 66:12, 1321-1340. DOI:10.1080/10407782.2014.916101

[67] H. Huang, T. TSun, G. Zhang, D. Li, H. Wei, Evaluation of a developed SST k-ω turbulence model for the prediction of turbulent slot jet impingement heat transfer, Int. J. Heat Mass Transfer, 139 (2019) 700-712. https://doi.org/10.1016/j.ijheatmasstransfer.2019.05.058

[68] H. Huang, T. TSun, G. Zhang, L. Sun, Z. Zong, Modeling and computation of turbulent slot jet impingement heat transfer using RANS method with special emphasis on the developed SST turbulence model, Int. J. Heat Mass Transfer, 126 (2018) 589-602. https://doi.org/10.1016/j.ijheatmasstransfer.2018.05.121

[69] Joel H. Ferziger, Milovan Perić, Robert L. Street. Computational Methods for Fluid Dynamics, Fourth Edition. Springer Nature Switzerland AG 2020. https://doi.org/10.1007/978-3-319-99693-6.

[70] A. Vassighi, M. Sachdev, Thermal and Power Management of Integrated Circuits, Springer, 2006. doi:10.1007/0-387-29749-9

[71] M. Goodarzia, M.R. Safaei, K. Vafai, G. Ahmadi, M. Dahari, S.N. Kazi, N. Jomharia, Investigation of nanofluid mixed convection in a shallow cavity using a two-phase mixture model, Int. J. Thermal Sciences, 75 (2014) 204-220. https://doi.org/10.1016/j.ijthermalsci.2013.08.003

[72] M.H. Bahmani, G. Sheikhzadeh, M. Zarringhalam, O.A. Akbari, A. Alrashed, G. Ahmadi Sheikh Shabani, M. Goodarzi, Investigation of turbulent heat transfer and nanofluid flow in a double 5 pipe heat exchanger, Advanced Pow. Tech. 29 (2018) 273-282. https://doi.org/10.1016/j.apt.2017.11.013

[73] A.Khelil, H.Naji, L. Loukarfi, M. Hadj Meliani, M. Braikia, Numerical simulation of the interactions among multiple turbulent swirling jets mounted in unbalanced positions, j. App. Math. Mod. 40 (2016) 3749-3763. https://doi.org/10.1016/j.apm.2015.10.047

[74] C. Seok-Ki, K. Seong-O, Turbulence modeling of natural convection in enclosures". A review J. Mech. Science Tech. 26 (1), (2012) 283-297. doi 10.1007/s12206-011-1037-0

[75] M.F. Koseoglu, S. Baskaya, The effect of flow field and turbulence on heat transfer characteristics of confined circular and elliptic impinging jets, Int. J. Thermal Sciences 47 (2008) 1332–1346. doi:10.1016/j.ijthermalsci.2007.10.015

[76] T. Kazuya, T. Miyako, L.W. Peter, N. Kazuyoshi, Swirl and buoyancy effects on mixing performance of baffle-plate-type miniature confined multijet, Int. J. Heat Fluid Flow 31, (2010): 45–56.

[77] D. C. Wilcox, Reassessment of the Scale Determining Equation for Advanced Turbulence Models, AIAA Journal, 26(11), (1988). https://doi.org/10.2514/3.10041

[78] k. Podila, Y. Rao, CFD modelling of supercritical water flow and heattransfer in a 2×2 fuel rod bundle, Nuc. Eng. Des. 301 (2016): 279–289. http://dx.doi.org/10.1016/j.nucengdes.2016.03.019

[79] H. Togun, M.R. Safaei, R. Sadri, S.N. Kazi, A. Badarudin, K. Hooman, E. Sadeghinezhad, Numerical simulation of laminar to turbulent nanofluid flow and heat transfer over a backward-facing step. App. Math. Comp. 239 (15) (2014) 153-170. https://doi.org/10.1016/j.amc.2014.04.051

[80] M. R. Safaei, H. Togun, K. Vafai, S. N. Kazi, A. Badarudin, Investigation of heat transfer enhancement in a forward-facing contracting channel using FMWCNT nanofluids, numerical heat transfer, Part A: Applications, 66:12, 1321-1340, DOI: 10.1080/10407782.2014.916101

[81] A. Khelil, H. Naji, M. Braikia, L. Loukarfi, Comparative investigation on heated swirling jets using experimental and numerical computations, J. Heat Transf. Eng. 36, (2014) 43-57. https://doi.org/10.1080/01457632.2014.906279

[82] Pope S.B, Turbulent Flows. Cambridge University Press, New York, (2000): pp.559–639.

[83] C. Nuntadusit, M. Wae-hayee, N. Kaewchoothong, Heat transfer enhancement on a surface of impinging jet by increasing entrainment using air-augmented duct, Int. J. Heat Mass Transfer, 127 (2018) 751-767. https://doi.org/10.1016/j.ijheatmasstransfer.2018.06.130

[84] Hunt JCR, Wray AA, Moin P. "Eddies, streams, and convergence zones in turbulent flows". In Center for turbulence research proceedings, CTR-S88, (1988): pp 193–208

[85] F. Nicoud, F. Ducros, Subgrid-scale stress modelling based on the square of the velocity gradient tensor, Flow Turbul. Combust. 62 (1999) 183-200. https://doi.org/10.1023/A:1009995426001.

[86] M. Germano, U. Piomelli, P. Moin, W.H. Cabot, A dynamic subgridscale eddy viscosity model. Phys. Fluids 3(7) (1991) 1760. https://doi.org/10.1063/1.857955.

[87] D. Lilly, A proposed modification of the Germano subgrid-scale closure method, Phys. Fluids 4 (1992) 633. https://doi.org/10.1063/1.858280.

[88] ANSYS Fluent Theory Guide - Fluent 18.1, 2017.

[89] G. Busco, Y.A. Hassan, Space and energy-based turbulent scale-resolving simulations of flow in a 5×5 nuclear reactor core fuel assembly with a spacer grid, Int. J. Heat Fluid Flow 71 (2018) 420-441. https://doi.org/10.1016/j.ijheatfluidflow.2018.04.003.

[90] P.J. Roache, Quantification of uncertainty in computational fluid dynamics, Annu. Rev. Fluid Mech. 29 (1997) 123-160. https://doi.org/10.1146/annurev.fluid.29.1.123.

[91] H.W. Coleman, F. Stern, Uncertainties and CFD validation, J. Fluids Eng. 119(4) (1997) 795-803. https://doi.org/10.1115/1.2819500.

[92] N. Salpeter, Y. Hassan, Large eddy simulations of jet flow interaction within staggered rod bundles, Nucl. Eng. Des. 251 (2012) 92-101. https://doi.org/10.1016/j.nucengdes.2011.10.066.

[93] M. Karimi, G. Akdogan, K.H. Dellimore, S.M. Bradshaw, Quantification of numerical uncertainty in computational fluid dynamics modelling of hydrocyclones, Comput. Chemical Eng. 43 (2012) 45-54. https://doi.org/10.1016/j.compchemeng.2012.04.009.

[94] A. Khelil, H. Naji, L. Loukarfi, M. Hadj Meliani, M. Braikia, Using numerical simulation to deepen understanding of the interaction of multiple turbulent swirling jets mounted with unbalanced positions, Appl. Math. Model. 40 (2016) 3749-763. http://dx.doi.org/10.1016/j.apm.2015.10.047.

[95] Y. Patel, Numerical Investigation of Flow Past a Circular Cylinder and in a Staggered Tube Bundle Using Various Turbulence Models, Master's thesis, (2010), Department of Mathematics and Physics, Lappeenranta University of Technology, 53850, Finland.

[96] M.A. Jahrul, L.P.J. Fitzpatrick, Large eddy simulation of flow through a periodic array of urban-like obstacles using a canopy stress method, Comput. Fluids 171 (2018) 65-78. https://doi.org/10.1016/j.compfluid.2018.05.027.

[97] Y. Dubief, F. Franck Delcayre, On coherent-vortex identification in turbulence, J. Turbul. 1(1) (2000) 1-22. https://doi.org/10.1088/1468-5248/1/1/011.